PASSIVE SENSING WITH SNAPPING SHRIMP NOISE

TOO YUEN MIN
(B.E.), Universiti Teknologi Malaysia (UTM), Malaysia

A THESIS SUBMITTED FOR THE DEGREE OF DOCTOR OF PHILOSOPHY

DEPARTMENT OF ELECTRICAL AND COMPUTER ENGINEERING

NATIONAL UNIVERSITY OF SINGAPORE

2016

DECLARATION

I hereby declare that this thesis is my original work and it has been written by me in its entirety. I have duly acknowledged all the sources of information which have been used in the thesis.

This thesis has also not been submitted for any degree in any university previously.

Too Yuen Min

30^{th} September 2016

ACKNOWLEDGEMENTS

The thesis would not be possible without the assistance of many great people. Upon accomplishing the study, I would like to take this opportunity to convey my appreciation to them in this acknowledgement.

Firstly, I would like to express my utmost gratitude to my supervisor, A/Prof. Mandar Chitre who introduced me to underwater acoustics. He not only provided technical guidance on my research but more importantly motivated me to face challenges. Thank you for believing in me, especially when I was overwhelmed with doubts throughout the study. I would not have been able to contribute in this field without your support.

I would also like to thank CENSAM[1] and ARL[2] for supporting the research work of my dissertation. I would like to acknowledge Dr. Venugopalan Pallayil and Mr. Anshu who are the key persons in conducting sea trials which lead to invaluable underwater acoustic datasets for the research. Discussions with Professor George Barbastathis, Dr. Hari Vishnu, Mr. Prasad Angangi, Dr. Matthew Legg, Dr. Hongqing Liu, Dr. Costas Pelekanakis facilitated in addressing limitations of the study. Thanks go to Ms. Ong Lee Lin for her help and guidance in my research writing.

I would like to thank A/Prof. Ong Sim Heng and A/Prof. Chen Xudong for providing comments on my research proposal during the PhD qualification defence. Their suggestions played an important role in shaping the research

[1] Center for Environmental Sensing and Modeling (CENSAM), Singapore-MIT Alliance for Research & Technology (SMART) - http://www.censam.mit.edu

[2] Acoustic Research Laboratory (ARL), Tropical Marine Science Institute (TMSI), National University of Singapore (NUS) - http://www.arl.nus.edu.sg/

directions of the study.

Finally, special thanks go to my parents for their love and support. They have instilled hard work and dedication in me such that I am able to procced with my academic goals.

Contents

Abstract

Snapping shrimp are found in abundance in shallow waters around the world. In such regions, they dominate the high frequency soundscape by producing transient impulsive signals known as “snaps”. Studies have shown that by estimating the spatial and temporal distribution of snaps we can obtain ecological information about the health of coral reefs. This provides an efficient alternative over conventional monitoring which deploys human divers to conduct inspection. Localizing snaps generated by the shrimp inhabiting underwater structures can reveal the physical forms of these submerged structures. All of these sensing applications rely on the ability to estimate the location of individual snaps accurately. Given the acoustic data from a hydrophone array, we can estimate the direction of arrival (DoA) of snaps if we measure the time difference of the arrival (TDoA) of the snap between sensors. This method estimates only the DoA but not the 3D location of most of the snaps because it assumes that the snaps originate at the near-field of the array. In a previous work, researchers have attempted to estimate the 3D location of the snaps and their occurrence times by using known bathymetric data. The work in this research does not assume a priori knowledge of the bathymetry.

The goal of this thesis is to explore the use of both direct and surface-reflected snaps in localizing far-field snapping shrimp noise for passive sensing. By measuring the TDoA of direct and surface-reflected snaps, we can estimate the

range of a snap source. However, considering that the receiver typically receives signals from multiple snap sources with similar acoustic signatures, it is not feasible to unambiguously distinguish the TDoA in the sensor array data for DoA and range estimation. The situation is further complicated by the fact that the signal propagating path consists of partially unknown parameters. We approach the problem of snap localization by detecting the direction of arrival and time of arrival (DoA-ToA) of an ensemble of impulsive transient signals, and then alternatingly associating the arrivals and refining the signal propagating path. In the investigation, we formulate a robust technique in detecting the DoA-ToA of impulsive signals through sparse recovery of an underdetermined linear system, and introduce an algorithm to approximately solve the arrival association and parameter estimation problem.

In this thesis, we developed method to estimate the location and time occurrence of snapping shrimp snaps located up to few hundred meters away from the receiver. This method was tested in Singapore waters using receiver measuring 1.3 m diameter. The estimated location of snapping shrimp allows us to passively image underwater man-made structures, and the estimated variations in receiver depth and orientation are shown to be consistent with tidal variation as reported in the Singapore tide-tables. This method paves the way for using portable sized receiver to conduct large-area passive sensing with snapping shrimp noise in coastal waters.

List of Tables

List of Figures

List of Acronyms

AUV	Autonomous Underwater Vehicle
BPDN	Basis Pursuit Denoising
BS	Block-Sparse
DAS	Delay And Sum
DFT	Discrete Fourier Transform
DoA	Direction of Arrival
DoA-ToA	Direction of Arrival and Time of Arrival
EM	Electromagnetic
FPC	False Positive Count
GPS	Global Positioning System
IID	Independent and Identically Distributed
NEPAN	Northeast Passive Acoustic Sensing Network
PSNR	Peak Signal to Noise Ratio
ROC	Receiver Operating Charateristic
ROMANIS	Remotely Operated Mobile Ambient Noise Imaging System
rS	reduced-Sparse
S	Sparse
SαS	Symmetric α-Stable
SOSUS	Sound Surveillance System
TDoA	Time Difference of Arrival
ToA	Time of Arrival
TP	True Positive
TPR	True Positive Rate
UCDWR	University of California Division of War Research
ULA	Uniform Linear Array

List of Notation

$\approx$	approximately equal to
$\sim$	distributed by
$\neq$	not equal to
x	scalar
$\mathbf{x}$	vector
$\hat{\mathbf{x}}$	unit vector
$\mathbf{X}$	matrix
$\mathbb{R}^N$	vector with N real value elements
$\{0,1\}^N$	vector with N binary value elements
$\mathbf{x}^\mathsf{T}$	transpose of $\mathbf{x}$
$\lvert x\rvert$	absolute value of x
$\lvert\mathbf{x}\rvert$	element-wise absolute value of $\mathbf{x}$
$\mathbb{H}(\mathbf{x})$	discrete Hilbert transform of $\mathbf{x}$
$\mathbb{U}(\mathbf{x})$	unit vector of $\mathbf{x}$
$\mathbb{P}_p(\mathbf{x})$	p^{th} percentile of the value in $\mathbf{x}$
$\lVert\mathbf{x}\rVert_p$	Lp-norm where $p \geq 1$
$\lVert\mathbf{x}\rVert_0$	total number of non-zero elements in $\mathbf{x}$
$\{\cdots\}$	element of a set
$\mathbb{Z}$	set of integer numbers
$\mathbb{Z}_{\geq 0}$	set of non-negative integer numbers
$\mathbb{R}$	set of real numbers
$\lvert\mathcal{X}\rvert$	cardinality of $\mathcal{X}$
$\mathcal{X} \cap \mathcal{Y}$	intersection between $\mathcal{X}$ and $\mathcal{Y}$
$\mathcal{X} \cup \mathcal{Y}$	Union between $\mathcal{X}$ and $\mathcal{Y}$
$x \in \mathcal{X}$	x is an element in $\mathcal{X}$
$\mathcal{Y} \subset \mathcal{X}$	$\mathcal{Y}$ is a subset of $\mathcal{X}$
$\exp(x)$	exponential of x
$\log(x)$	logarithm with base 10 of x
$\sin(x)$	sine of x
$\cos(x)$	cosine of x
$\tan(x)$	tangent of x
$\mathcal{N}(\mu, \sigma^2)$	univariate normal distribution with mean μ and variance σ^2

Chapter 1

Introduction

1.1 Sonar and passive sensing

Electromagnetic (EM) waves such as light and radio waves suffer from high attenuation in water, a significant factor which limits their use in underwater sensing. For example in coastal waters, optical visibility can fall below a few meters in range [1], [2]. On the other hand, sound travels longer distances underwater than EM waves, making it an efficient tool for probing the ocean. The use of sound for underwater navigation and ranging is traditionally known as sonar. There are two types of sonar — active and passive. Active sonar involves emitting sounds and listening for echoes, while passive sonar involves listening to the presence of underwater sounds. From the observed sounds and echoes, a sonar system can detect, locate and characterize both underwater sound sources and scatterers. Over the years, sonar has evolved into a mature technology. It has found use in diverse fields ranging from military applications such as submarine detection and navigation to commercial applications like fish finding, echo sounding, bathymetric mapping, ocean surveillance, etc.

Advances in the study of underwater ambient noise lead the way to the investigation of a technique called passive sensing. In contrast to sonar, passive sensing observes sounds generated by ambient sources such as human activities, marine life and natural physical processes, and extracts useful information surrounding these sources through the observation. Understanding the generation mechanism and biological properties of these ambient sources offers additional ability to extract useful information out of the ambient recording. For example, wind actions on the water surface [3]–[5] and ship noise [6] provide natural insonification for seabed layer imaging and characterization. The idea of utilizing ambient sources for various sensing applications has gained momentum in recent years.

In tropical and subtropical coastal waters, snapping shrimp has been regarded as one of the consistent and reliable ambient sources. Sounds emitted by snapping shrimp dominate the high frequency soundscape underwater [7]. The ensemble of snapping shrimp noise creates a background crackle which causes significant negative impact on sonar and underwater communication systems in conventional processing [8]–[10]. However recent field studies suggest that snapping shrimp noise are useful for passive sensing. Healthy coral reefs bustle with noise from the snapping shrimp. Conversely dead reefs are silent. For instance, estimated density of snapping shrimp is reported to be one to two orders magnitude greater within the healthy habitat than degraded ones [11]. Therefore detecting shrimp distribution on known coral reef locations help us to assess the health of the reef population. This method is more efficient compared to standard coral reef monitoring approaches which are time-consuming, prone to human bias, besides being manpower intensive. Location of shrimp reveals pictorial images of underwater submerged structures. Matching these images with the known local bathymetry allows underwater vehicle to perform passive positioning. This is similar to how some pelagic larval reef fishes make use of reef sounds dominated by snapping shrimp noise for navigational purposes [12], [13].

Passive sensing with snapping shrimp noise relies on the ability to estimate the location of shrimp accurately. This area of study remains a challenging problem. The primary difficulty arises from the fact that the aperture size of the receiver limits the detectable range of the snapping shrimp, especially when using conventional passive localization method. Larger aperture receiver is required to localize snapping shrimp farther away. However, deploying large aperture receiver is costly and may not be suitable for certain sensing applications. The secondary difficulty lies in localizing snapping shrimp sources, given that a few thousand acoustic signals comprising the direct arrivals and their multipath propagations can be observed within a short period of time. These signals are broadband, transient and impulsive, have similar acoustic signatures, and occur sporadically. Detecting and estimating the originating location of these signals is considerably harder than for conventional acoustic signals which are continuous and occur in small amounts.

1.2 Objectives

The ocean surface acts like an acoustic reflector to reflect snaps. The main aim of this thesis is to explore the use of direct and surface-reflected snaps in localizing far-field snapping shrimp noise for large-area passive sensing. Achieving this goal enables improvement in the portability and energy consumption of passive sensing applications with snapping shrimp noise without sacrificing the attainable range for sensing. By measuring the TDoA of direct snaps between sensors, we can estimate DoA of the snaps. By measuring the TDoA of direct and surface-reflected snaps, we can estimate the range of the snaps. The DoA and range of the snaps completely define the location of snaps. Estimating the DoA and range of snaps is non-trivial, because in practice, large numbers of direct and surface-reflected snaps are received in the observation period. These arrivals have very similar acoustic signatures and the arrival propagating path is only partially known. We investigate the snap localization problem by first detecting the direction of arrival and time of arrival (DoA-ToA) of impulsive transient signals which comprise direct and surface-reflected snaps. Subsequently, we alternatingly associate the ensemble of DoA-ToAs and refine the arrival propagating path to estimate the location of snaps. The specific objectives of this research are to:

- investigate the advantage of sparse assumption in detecting DoA-ToA of snapping shrimp noise;
- study the use of multipath ranging in estimating the originating locations of snaps with and without the associated direct and multipath arrivals of these snaps;
- demonstrate that the knowledge of location of the shrimp can be used for sensing.

1.3 Scope of the research

This study focuses on localizing snapping shrimp noise using small aperture receiver in shallow waters. Since the snapping shrimp noise dominates the high frequency soundscape of underwater ambient noise, we use ray tracing as the propagation model of snapping shrimp noise. We also assume an iso-velocity channel such that ray paths are straight lines. We do not consider deep water and cold water scenario as the propagation of acoustic wave is refracted such that the ray path is a curve. The small aperture receiver consists of numerous sensors and the positions of these sensors are assumed to be fixed with no uncertainties in array geometry. The locations of the receiver and snapping shrimp are static during the observation period. Other underwater ambient noises such as shipping noise and breaking waves are present in the acoustic recording of the receiver. Since our signal of interest is snapping shrimp noise, these ambient sources are filtered by bandpass filtering the frequency of the data. Impulsive signals, which correspond to direct and surface-reflected snaps, have distinct DoA-ToAs and are observed by the receiver at approximately the same time. The thesis focuses on detecting and localizing the originating locations of snaps. We are interested in the direct usage of detected and estimated locations of snaps for passive sensing such as forming pictorial images of submerged structures. The indirect usage such as illuminating underwater silent objects using snapping shrimp noise is not straightforward and hence it is not discussed in the thesis.

1.4 Contributions

The following are contributions made by this study.

- DoA-ToA detection of nearly identical, impulsive and transient signals is formulated as an inverse problem of an underdetermined linear system. The idea of choosing minimum number of DoA-ToAs given the array sensor data in solving this inverse problem, is proposed. We show that the proposed method possesses better detection performance than the existing methods through receiver operating characteristic (ROC). We also demonstrate that the proposed method is robust to the changes in aperture size and number of sensors in the receiver, a consideration which is crucial for practical implementation. Detection of impulsive signals is an active area of research to solve problems ranging from seismic imaging [14] to forensic science and audio surveillance systems [15]. The proposed method is well-suited to handle these types of applications.

- Given that perfect association of direct and surface-reflected snaps is known, a 3-dimensional geometric model describing the direct arrival and surface reflection of snaps is proposed. Uncertainties in water surface and receiver orientation are considered in this model. This leads to the construction of a range estimator of snap parameterized by nominal receiver depth and receiver orientation. Assumed parameters are normally perturbed from the true values and this may lead to large range estimation error for snap localization. A two-step minimization method is proposed to improve the assumed parameters so that the range of snaps can be accurately estimated using estimated parameters which are close to the true values. The range estimation error based on estimated parameters is much lower than the range estimation error based on assumed parameters in numerical simulations. We believe that this is the first time such kind of work has been used for snap localization. This work may provide a theoretical framework for underwater source localization by incorporating information of direct and surface-reflected signals with just the partial knowledge of the propagating path.

- In practice, the problem is further complicated by the fact that not only the propagating path of the arrivals is partially known, but the perfect association of direct and surface-reflected snaps is also generally not known. Estimating the location of snaps from the ensemble of DoA-ToA of impulsive signals relies on the ability to jointly associate the arrivals to form direct and surface-reflected pairs, while estimating the parameters to completely describe the arrival propagating path. This joint association and estimation problem is difficult to solve. We propose an algorithm which alternates the association of arrivals given the fixed parameters, with the estimation of the parameters based on the fixed set of associations. In numerical simulations, the alternating method is capable of estimating the location of snaps to reveal their spatial distribution without knowing the perfect association of direct and surface-reflected snaps. The investigation contributes to a better understanding of practical challenges in snap localization based on direct and surface-reflected snaps. The proposed method provides an alternative to solve this problem approximately.

- The proposed methods are tested in two experiments which were conducted in different bathymetric environments in Singapore waters. The estimated locations of snaps correlate with the position of underwater submerged structures such as long-term mooring buoys and jetty. The estimated nominal receiver depth matches the pattern of tidal changes in the

Singapore tide table. This empirically shows that passive sensing in the range of about two hundred meters using a small aperture receiver measuring in 1.3 m diameter is feasible by solely incorporating the direct and surface-reflected snaps. This suggests that a large-area passive sensing system with snapping shrimp noise using a portable receiver is a viable approach.

1.5 Thesis Organization

Chapter 2 gives a brief review on underwater passive sensing. The characteristics of snapping shrimp noise are presented followed by a discussion on existing sensing applications which rely solely on using ambient sources. Literature survey on passive snap localization schemes is included. A broadband snapping shrimp noise recording system is discussed to facilitate the understanding on experimental datasets.

Chapter 3 presents an underdetermined linear system to model the array sensor data largely dominated by snapping shrimp noise. Sparse approximation in detecting the DoA-ToA of the snaps is explored. The detection performance of the sparse approximation-based approach is compared with existing methods via numerical simulations.

Chapter 4 presents a 3-dimensional geometric model of the associated direct arrival and surface-reflected snaps. Range estimator of the snaps is constructed and the sensitivity of the approximated parameters with respect to the estimated range is discussed. Chapter 5 introduces a method to refine the approximated parameters based on an ensemble of associated arrivals. By relaxing the assumption of perfect association, a more practical snap localization problem is discussed and an algorithm is proposed to tackle the problem.

In chapter 6, snapping shrimp noise detection and localization methods are tested via two sets of experiments in Singapore waters. The effectiveness of the proposed methods is demonstrated by the match between the spatial distribution of estimated snaps and several known underwater man-made structures.

Chapter 7 summarizes the key findings of the study and provides further research directions to address the limitations of the study.

Chapter 2

Background

This thesis encompasses a broad number of topics ranging from passive sensing and characteristic of ambient noise generated by snapping shrimp, to techniques of underwater source localization. Throughout the years, these topics have been extensively explored. This chapter on the background of study is not meant to be exhaustive but to introduce concepts that facilitate readability of the following chapters.

2.1 Underwater passive sensing

The first practical use of underwater passive sensing can be dated back to early 1900s during World War I even though a similar idea has been conjectured by Leonardo da Vinci in much earlier times [16]. The invention was developed by the Allies to listen to the machinery noise of German submarines. Observing the noise allowed not only the detection and localization of submarines but also their identification through the individual acoustic signatures. However, passive sensing is sensitive to underwater ambient noise. For instance, the University of California Division of War Research (UCDWR) scientists identified snapping shrimp as the major coastal noise sources affecting sonar during World War II [17]. As technology advances, submarines become progressively quieter, such that conventional passive sensing is no longer effective. Instead of listening to the noise generated by submarines, Flatte and Munk explored the possibility of detecting submarines via scattered acoustic signals from underwater ambient noise [18].

Besides military applications, passive sensing is an important tool in marine biological research. The Sound Surveillance System (SOSUS), which is a network of hydrophones mounted on the seafloor, was used to passively detect and locate blue whale in the northeast Pacific Ocean [19]. This is useful in studying the migratory pattern and behaviour in the open ocean. Other passive sensory systems like Northeast Passive Acoustic Sensing Network (NEPAN) provide information on the presence and physical distribution of whales, dolphins, and certain species of fish [20]. In ocean monitoring, estimating water depth and seabed sub-bottom layering can be done using ambient noise correlations [3]. Similar correlation techniques can also be used to monitor deep ocean temperature, an important indicator and determining factor on the Earth's climate evolution [21]. Passive acoustic thermometry of the deep ocean, as implemented in Ascension and Wake islands, only requires two existing hydroacoustic stations for ambient noise recording.

Passive sensing is also an energy-efficient technique to identify potential underwater threats for long-term underwater security and surveillance due to its low power consumption. Passive tracking methods using an array of sensors have been developed to detect and track open-circuit divers or intruders in coastal waters by searching for their breathing waveforms [22], [23]. Detecting, localizing and tracking either noisy submerged objects or ambient sources play a very crucial part in underwater passive sensing. In general, passive sensing is a broad topic. We focus our study on passive sensing using snapping shrimp noise in shallow waters. This problem is interesting because snapping shrimp noise is one of the most pervasive sounds in tropical littoral waters. Several findings have demonstrated how snapping shrimp noise can be used as sources of opportunity in underwater passive sensing [7], [24], [25]. We discuss some of the passive sensing techniques in the following section.

2.2 Snapping shrimp noise

2.2.1 Individual snap

Snapping shrimp, also known as pistol shrimp, belong to the Alpheidae and Synalphedae family of crustaceans. These animals grow to only a few centimeters long with one normal claw and one distinctive enlarged claw which can measure up to half the length of its body. Figure 2.1 shows a photograph of a snapping shrimp. Johnson et al. discovered that all lower latitude regions are within the geographical zone of snapping shrimp [26]. Cato and Bell noted that shrimp are commonly found in tropical and subtropical shallow waters with temperature does not go below 11 degrees Celsius and at depths of less than 60 m [27]. They live in colonies, lodging on coral reefs, man-made structures, debris, etc. The rapid closure of the enlarged claw shoots out water and creates a low pressure cavitation bubble that collapses with an extremely loud sound [28]. This generates the acoustic signature of the snap, which starts with a full closure of the claw to produce a precursor pulse. The cavitation bubble grows until it collapses to create a main peak, followed by a reverberation time containing the oscillations of the main peak [29]. Immediately after the main peak due to collapse of the bubble, smaller bubbles are repeatedly created and then collapse until a complete dissolution of the bubble. This process is denoted as immediate reverberation. This is then followed by much later reverberation due to the multipath reflections. Figure 2.2 illustrates a time series acoustic pressure recording of a snap in Singapore waters. The "reverberation" in Figure 2.2 defines the immediate reverberation. The theoretical model in [28] predicts the width of the main spike of a shrimp snap to be in the order of 100 ps. However, in practice, the observed spike width is probably in the order of few μs because of the low pass filtering effect of the ocean as well as the limited sampling rate [24]. The acoustic pressure of shrimp snaps in Sydney Harbour at Pyrmont and Coral sea near Innisfail were measured using a system with 350 kHz bandwidth. The snap recording shows a peak width that varies from 3.5 to 8 μs and a bandwidth that extends beyond 200 kHz [27]. Au and Banks show that the reverberation time of a snap is within 100 μs while Legg et al. calculate it as 1.2 ms [30], [31]. The difference could be attributed to the impulse response of the environment and the recording system.

2.2.2 Ensemble of snaps

Persistent crackling sounds are often reported by scuba divers in shallow waters. This background crackle is the resultant of a large number of snaps in a short period of time. Figure 2.3 shows a 10-second clip of $25-75$ kHz bandpass filtered ambient noise recording in Singapore waters, which is dominated by snapping shrimp noise. As can be observed, the recorded signal comprises multiple impulsive transient signals. These signals are the direct arrival of the snaps and

Figure 2.1: Snapping shrimp. "Alpheus heterochaelis" by "Crabby Taxonomist" License under a Creative Common Attribution-NonCommercial-ShareAlike 2.0 Generic (CC BY-NC-SA 2.0). Accessed on 18 August 2016. `https://www.flickr.com/photos/crabby_taxonomist/7213807522/in/album-72157629764324092/`

the respective multipath propagations. The amplitude variation of the recording can be modeled using a symmetric α-stable (SαS) distribution [32] or more recently an α-sub-Gaussian noise model with memory [33]. The family of SαS distributions generalizes the central limit theorem to include the impulsiveness of pressure variation. Investigations show that snap occurrences are not completely random. Snaps tend to cluster within short (less than a second) and medium (1 s – 400 s) time scale. Short time scale clustering can be possibly attributed to surface reflections [8]. Ambient signal is not impulsive as compared to shrimp snap signal. Figure 2.4 shows the acoustic pressure recording of shrimp snap and ambient signal.

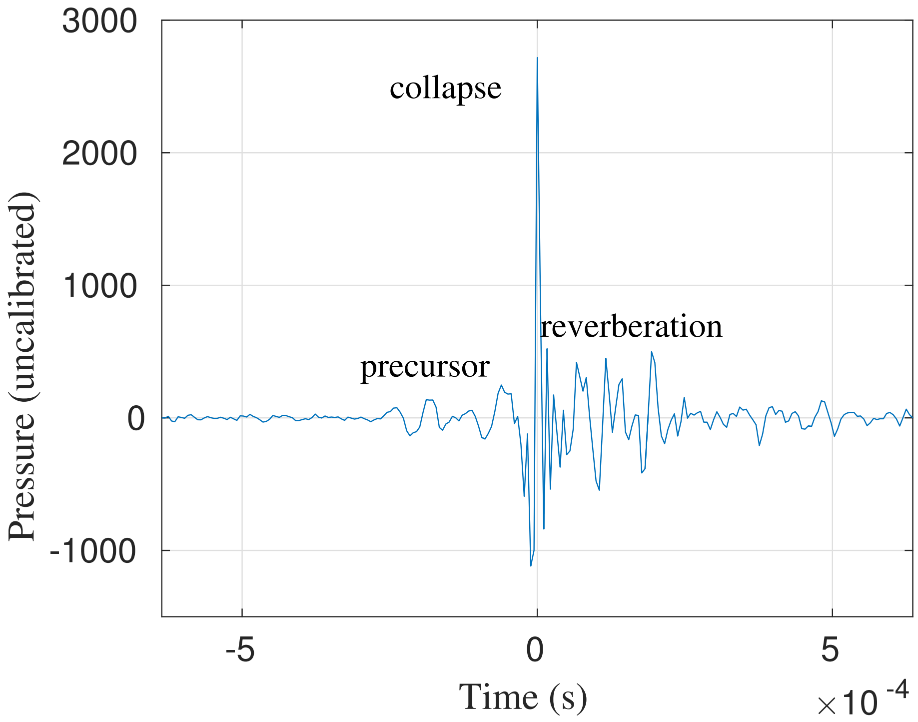

Figure 2.2: An acoustic pressure recording of a snap in Singapore waters.

2.2.3 Sources of opportunity

The idea of utilizing ambient sounds for acoustic sensing is not new. Listening to the sounds generated by wind actions on the water surface enables seabed layer imaging and charaterization [3]–[5]. Cross-correlating underwater diffuse noise measurements produces estimation for sound-speed profiles [34]. We are interested in snapping shrimp acting as sources of opportunity for passive sensing and thus several experimental findings are reviewed in the following paragraphs.

During the study of the use of ambient noise for underwater imaging, snapping shrimp noise has been used to illuminate silent submerged objects in the ocean. In one of the experiments, Epifanio et al. realized that a lot of impulsive transient signals reflected by a submerged object originated from

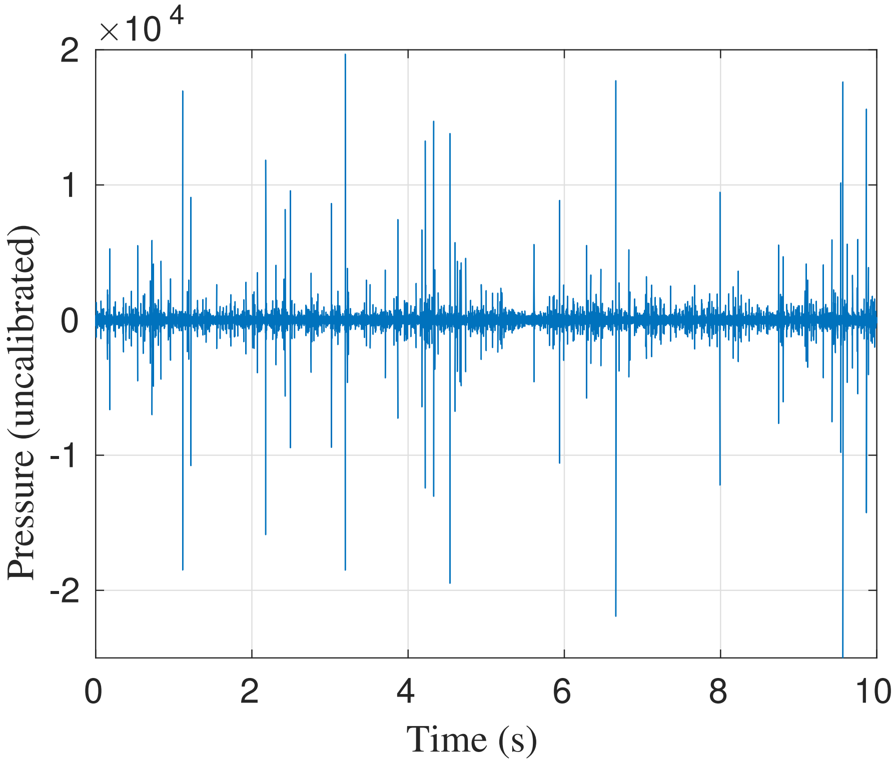

Figure 2.3: 10-second acoustic pressure recording of ambient noise in Singapore waters dominated by snapping shrimp noise.

snapping shrimp located at pier pilings behind the receiver, and they provide significant energy contrast to form a pictorial image of the object [35]. Potter et al. showed that temporal variation of directional acoustic pressure is a better quantity to use to differentiate between the reflected snapping shrimp noise and the underwater background noise [36]. Kuselan et al. noticed that not all of the ambient sources contribute to the object illumination and suggested that by judiciously selecting arrivals that provide illumination and rejecting others, the image quality can be improved [37]. Chitre et al. demonstrated that passive ranging of silent submerged objects is feasible given the rough locations of the shrimp [38]. This is analogous to range estimation using multistatic sonar.

Coral reefs are home to a multitude of living creatures some of which are

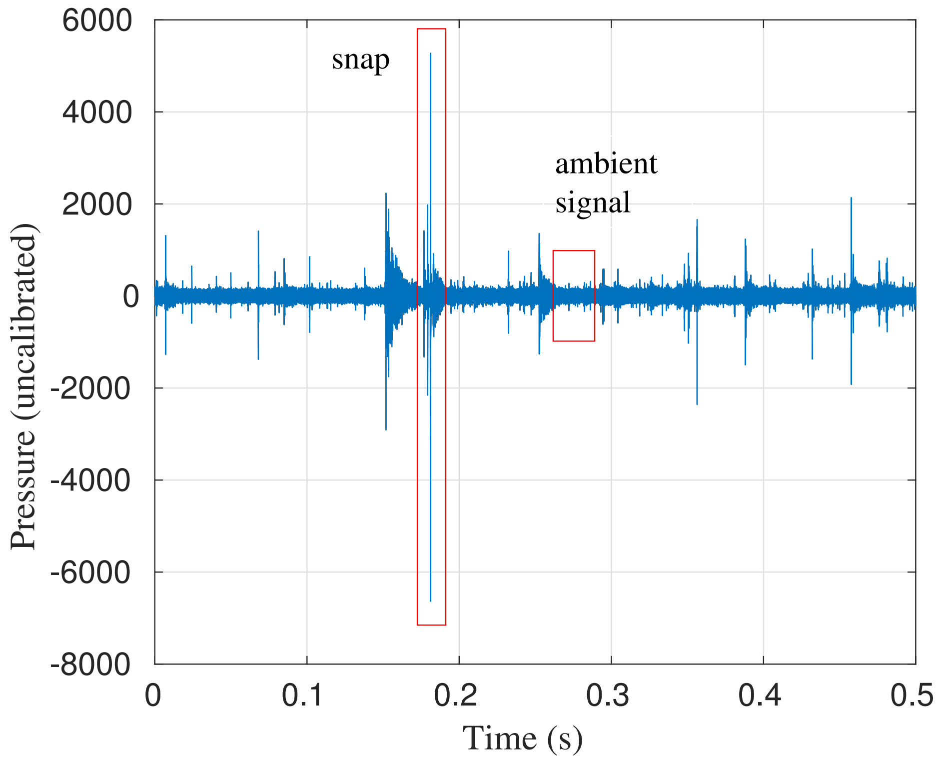

Figure 2.4: Acoustic pressure recording of underwater ambient noise containing shrimp snaps and ambient signals.

extremely noisy like the snapping shrimp. Field results indicate that reef fishes find their way back to the reefs where they originated from by listening to the sounds of snapping shrimp and fishes on the reefs [12]. Piercy et al. found that higher-quality reefs tend to be noisier than degraded reefs [39]. Sounds emitted by snapping shrimp give indication on the location and health of coral reefs [7]. The mapping of low density clusters on known coral reefs might suggest dead reefs. This approach is fairly efficient compared to the traditional practice of sending divers underwater for inspection. A snap reflected off the seabed contains information about the sediment. Multiple snaps enable the estimation of seabed sediment properties [24]. It is also possible to image submerged structures using noise generated by the shrimp inhabiting these structures [40]. The time difference between direct arrivals and surface reflections of snaps is useful in the passive estimation of the depth of autonomous underwater vehicles (AUVs) [41].

Most of the aforementioned applications of passive sensing with snapping shrimp noise rely on the ability to localize individual snaps. The common practice of using large aperture receiver for snap localization is not effective for large area coverage. Other localization methods rely on strict assumptions which are only appropriate for certain applications. We discuss some of these issues in the next section.

2.3 Passive snap localization

Consider a receiver in the form of an array of sensors, and assume that the sources of sounds are static over the observation period. Let the location of a source be defined by the DoA and range with respect to the origin of the receiver. Passive localization methods can be classified into two main categories [42]. The first is wavefront curvature method. The maximum range between the origin of the receiver and the source has to be at most a few multiples of the aperture size of the receiver. This enables the arrival waveform of the source to be spherical in shape. Figure 2.5 shows an arrival of a near-field source observed by a uniform linear array (ULA) receiver. The near-field TDoA between sensors can be written as

$$\Delta\tau_{\text{near}} = \frac{1}{c}\left(D - \sqrt{L^2 + D^2 - 2LD\cos(\gamma)}\right) \tag{2.1}$$

where L is the spacing between sensors of the receiver, D is the range of the source from the origin of the receiver, γ is the DoA of the source, and c is the speed of sound underwater. Given multiple measurements of $\Delta\tau_{\text{near}}$ for different sensors, Equation 2.1 can be extended to a nonlinear system and by solving the inverse problem of this system, we can estimate the DoA and range of the source. This method forms the basis of many modern ranging systems and has been applied to estimate the location of shrimp. A 3-sensor ULA with interelement spacing of 9.7 m was deployed in Sydney Harbour [40]. This experiment demonstrates the passive localization of snapping shrimp noise using wavefront curvature method. The spatial distribution of snapping shrimp agrees with the structure of the wharf. Freeman et al., by using a bilinear array of 6 m diameter, found that local biological sources, including snapping shrimp, were situated on or inside the reef structure rather than the adjacent sandy areas [43]. The disadvantage of wavefront curvature method is that the sources have to be in the near-field of the receiver, i.e., the range of the sources is limited by the size of the receiver's aperture. Deploying a large aperture receiver, especially the 2-dimensional array, is not practical in shallow waters. This limits the ability to locate shrimp in 3 dimensions. Furthermore, identifying the same snap in two different sensors well-apart is a challenging problem.

A small aperture ULA receiver observes an plane wave arrival of a far-field source as illustrated in Figure 2.6. Far-field TDoA between sensors is a function of DoA such that

$$\Delta\tau_{\text{far}} = \frac{L\cos(\gamma)}{c}. \tag{2.2}$$

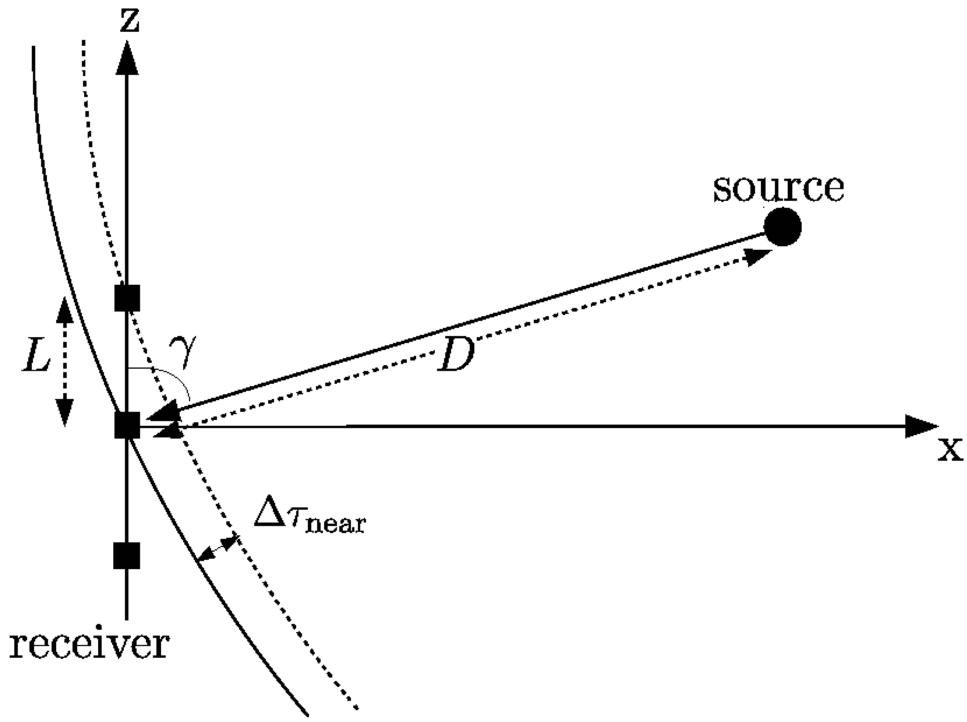

Figure 2.5: A 2-dimensional sketch illustrating the propagating spherical wave originating from a near-field source. The solid and dashed spherical waves represent the same waveform at different time instants.

We can only estimate the DoA but not the range of far-field sources given multiple measurements of $\Delta\tau_{\text{far}}$ for different sensors. The second approach of passive localization, namely multipath ranging, solves the far-field range estimation problem. It incorporates the direct arrival and multipaths of the source to form an effectively larger virtual receiver. This enables us to accurately estimate the range of sources in far-field without having to build a physically large aperture receiver. Figure 2.6 gives a brief idea of the geometry for multipath ranging of a source based on direct arrival and surface-reflected arrival. To the best of our knowledge, multipath ranging has not yet been utilized to estimate the location of snapping shrimp. Quite a number of encouraging results have been obtained from localizing cetaceans such as dolphin and whale [44], [45]. Only a small number of click sounds emitted by dolphins are observed during the observation period. Hence, associating the direct arrival and surface-reflected click sounds is considerably simple. In contrast, thousands of snaps can be observed even in a short period of time and the acoustic signatures of the snaps are almost identical. Identifying the correct surface reflection of a snap arrival is non-trivial. Other passive localization attempts have also been proposed. For instance, colonies of shrimp can be localized using triangulation by moving the small aperture receiver to different locations over a long period of time [46]. Continuous collection of ambient noise measurements over a long period is time consuming, and may not be suitable for certain applications. Chitre et al. estimated shrimp locations using small aperture receiver with the assumption that snapping shrimp live on a flat seabed [38] . This may not be valid and exact knowledge of the local bathymetry is not always available.

In short, the state-of-the-art for snapping shrimp passive localization can be categorized into near-field and far-field localization. Near-field localization is based on the concept of wavefront curvature method which limits the spatial coverage of the snaps. Far-field localization relies on certain assumptions which may not be true in practice. Both of these methods suffers from the respective limitations.

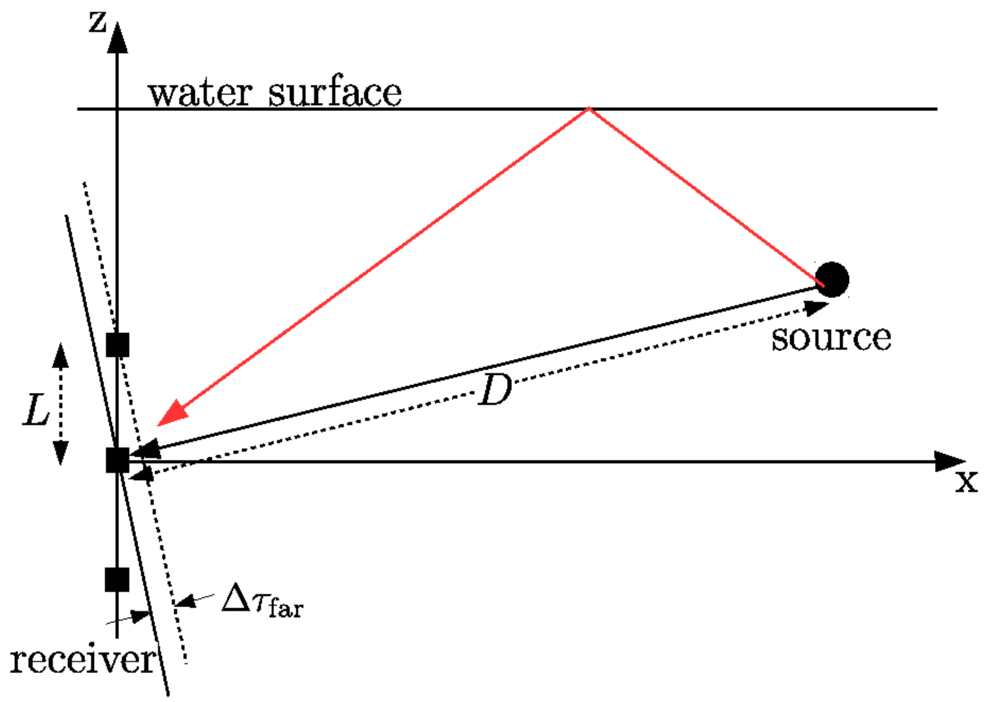

Figure 2.6: A 2-dimensional sketch illustrating a propagating plane wave originating from a far-field source. The solid and dashed plane waves represent the same waveform at different time instants. The red line indicates the propagating path of the surface-reflected arrival.

2.4 Remotely Operated Mobile Ambient Noise Imaging System (ROMANIS)

There are numerous data acquisition systems for snapping shrimp noise recording. Acoustic Daylight Ocean Noise Imaging System (ADONIS) is one of the systems which used to investigate the feasibility of forming pictorial images of a silent underwater objects solely by using ambient noise [35],[47]. A 4-sensors tetrahedral array namely, the High frequency ambient noise Data AcQuisition System (HiDAQ) was developed to study the high frequency ambient noise of Singapore waters, which consists predominantly of snapping shrimp noise [48].

Our study is based on the underwater acoustic pressure data collected by ROMANIS.

ROMANIS was primarily built to study the ambient noise soundscape as well as the feasibility of illuminating silent submerged objects using snapping shrimp as the main natural insonifiers. It is a broadband planar array comprising 508 sensors and measuring 1.3 m in diameter [49], [50]. Sensors are placed non-periodically. Each sensor of ROMANIS is able to sample at 196000 samples per second. The frequency band of ROMANIS is 25 kHz$-$75 kHz which is also the frequency band that contains significant amount of energy from snapping shrimp. 25 kHz and 75 kHz are selected to give the most effective imaging resolution and range. The angular resolution of this array is roughly 1° at the highest frequency of operation. A fully populated array requires more than ten thousand sensors, driving up the computational complexity beyond current practical limits. Without sacrificing the resolution, a sparse array was implemented in the design [51]. Figure 2.8 shows the aperiodic sensor placement of ROMANIS.

Throughout the study, ROMANIS was used to record snapping shrimp noise in Singapore waters. The large number of sensors improve the detection capability of snaps especially the multipath propagations which are generally weaker in strength.

2.5 Summary

In this chapter, we presented the topic of underwater passive sensing by introducing several applications. We proposed using snapping shrimp noise for

Figure 2.7: A photograph of ROMANIS.

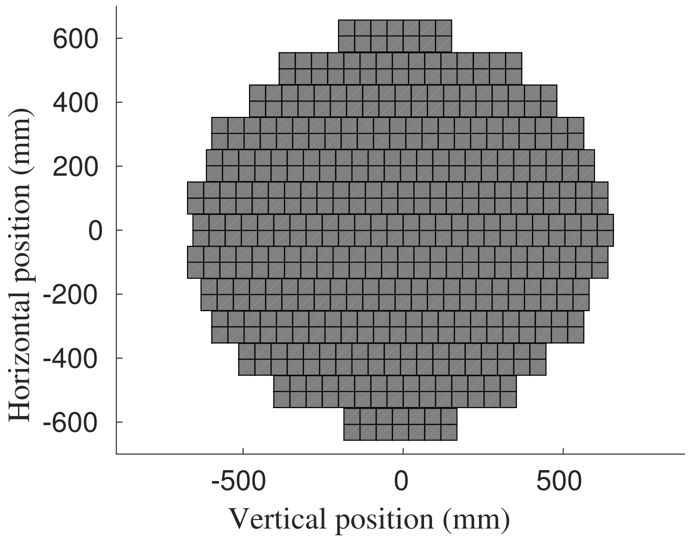

Figure 2.8: Sensor placement of ROMANIS. Each gray cell represents a sensor.

passive sensing, and provided a description on the snap mechanism, its signal statistics as well as the established results of some applications. As passive sensing is closely related to passive localization, the ideas of passive localization were briefly reviewed. Finally, we concluded the chapter by discussing the details of the receiver which is going to be used in the study.

Chapter 3

Detecting the DoA-ToA of transient impulsive signals

Cross-correlation-based TDoA is known to be effective in detecting the source of a continuous signal impinging on an array of sensors. However when multiple transient impulsive signals which have similar acoustic signatures are observed simultaneously, the performance of the TDoA method degrades drastically. Beamforming estimates the time domain propagating signals given the array sensor data through coherent and incoherent sum. Identifying high amplitude elements from the beamformed output yields DoA-ToAs of impulsive signals. This method may prone to false positive detection due to sidelobe of the beamformer. In this chapter, we propose robust methods, namely Sparse and reduced-Sparse, to detect DoA-ToA of impulsive transient signals such as those originating from multiple sources of snapping shrimp. The robustness is measured based on true positive and false positive detection rate of DoA-ToA of impulsive signals using receiver with different aperture sizes and number of sensors. A robust DoA-ToA method possesses high true positive and low false positive detection in all receiver configurations.

3.1 Signal model

To formally introduce the problem, we present a signal model to describe the acoustic pressure sensor array data of the impulsive transient signals. Let the acoustic center of an array be the origin of a Cartesian coordinate system. Let J be the number of transient impulsive signals arriving from the far-field, i.e., the signals are represented by $\{(\phi_j^*, \theta_j^*, \Gamma_j^*)\}_{j=1}^J$ where $*$ denotes the true value. Each signal is associated with a 3-tuple $(\phi_j^*, \theta_j^*, \Gamma_j^*)$, consisting of the azimuth angle, elevation angle, and the ToA. The acoustic pressure data of sensor m of the array at time $t_n = \frac{n}{F_s}$, $n \in \mathbb{Z}_{\geq 0}$, can be written as

$$x_m(t_n) = \sum_{j=1}^{J} s_j(t_n - (\Gamma_j^* + \tau_m(\phi_j^*, \theta_j^*))) \tag{3.1}$$

where F_s is the sampling rate. $s_j(t_n)$ is the acoustic pressure of signal j at time instance t_n. $\tau_m(\phi, \theta)$ is the time delay associated with the additional time needed for a source signal to reach the sensor m, and is given by $\tau_m(\phi, \theta) = \frac{\mathbf{p}_m^\mathsf{T} \mathbf{q}(\phi,\theta)}{c}$, where $\mathbf{q}(\phi, \theta) \in \mathbb{R}^3$ is the unit vector in the signal propagating direction, $\mathbf{p}_m \in \mathbb{R}^3$ is the sensor location, and c is the speed of sound in water. Figure 3.1 illustrates a simplified signal model by considering two impulsive transient signals.

The discrete Fourier transform (DFT) of the T collected snapshots of the sensor data can be written as

$$\mathrm{x}_m(f_k) = \sum_{j=1}^{J} \exp(-\mathrm{j}2\pi f_k \tau_m(\phi_j^*, \theta_j^*)) \exp(-\mathrm{j}2\pi f_k \Gamma_j^*) \mathrm{s}_j(f_k) \tag{3.2}$$

for $f_k = \frac{k}{T} F_s$, $k = \{0, 1, \cdots, T-1\}$ where $\mathrm{j} = \sqrt{-1}$. The DFT of M-sensor array data can be expressed as

$$\mathbf{x} = \mathbf{A}\mathbf{c} \tag{3.3}$$

where $\mathbf{A} = [\mathbf{A}_1, \cdots, \mathbf{A}_{|\mathcal{B}|}] \in \mathbb{C}^{MT \times T|\mathcal{B}|}$ is an overcomplete array response matrix

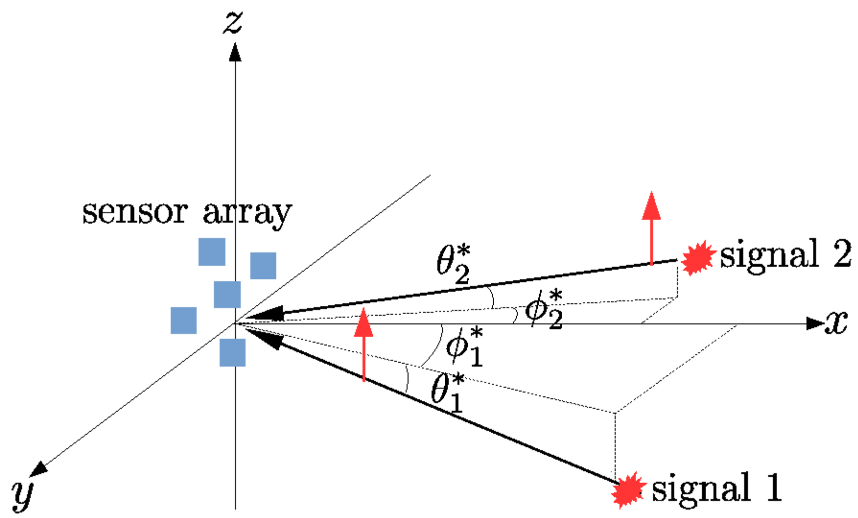

Figure 3.1: A sketch of sensor array observing the arrival of two impulsive transient signals. The vertical red arrows indicate the spatial displacement of the propagating signal at the particular snapshot.

represented as a partitioned matrix, with column sub-matrices of the form: [52]

$$\mathbf{A}_b = \begin{pmatrix} \mathbf{a}(f_0, \phi_b, \theta_b) & \mathbf{0} & \cdots & \mathbf{0} \\ \mathbf{0} & \mathbf{a}(f_1, \phi_b, \theta_b) & \cdots & \mathbf{0} \\ \vdots & \vdots & \ddots & \vdots \\ \mathbf{0} & \mathbf{0} & \cdots & \mathbf{a}(f_{T-1}, \phi_b, \theta_b) \end{pmatrix} \tag{3.4}$$

where $\mathbf{a}(f_k, \phi_b, \theta_b) = [\exp(-\mathrm{j}2\pi f_k \tau_1(\phi_b, \theta_b)), \cdots, \exp(-\mathrm{j}2\pi f_k \tau_M(\phi_b, \theta_b))]^\mathsf{T}$, and $b = 1, 2, \cdots, |\mathcal{B}|$ where $\mathcal{B}$ is the discrete space of all possible DoA. $\mathbf{x} = [x_1(f_1), x_2(f_1), \cdots, x_M(f_1), x_1(f_2), \ldots, x_M(f_{T-1})]^\mathsf{T} \in \mathbb{C}^{MT}$ is the column vector of the Fourier coefficients of the array sensor data. $\mathbf{c} = [\mathbf{c}_1, \cdots, \mathbf{c}_{|\mathcal{B}|}]^\mathsf{T} \in \mathbb{C}^{T|\mathcal{B}|}$ with $\mathbf{c}_j = [s_j(f_0), \cdots, s_j(f_{T-1})]^\mathsf{T}$ for $j = 1, 2, \cdots, |\mathcal{B}|$ is the column vector with J non-zero blocks denoting the phase shifted Fourier coefficients of the arrivals. Note that the ToA functions are non-linear. The next step is to extend the overcomplete sensing matrix to include the discrete space occupied by all possible ToAs. This extended formulation does not scale well as the size of the sensing matrix increases exponentially with the number of possible ToAs.

3.2 DoA-ToA power map

The discrete space of all possible DoA-ToA is denoted by $\mathcal{S}$. The DoA-ToA power map $\mathbf{z}$ is a vector indexed by $\mathcal{S}$ such that the amplitude of the element indicates absolute square of acoustic pressure of the signals in DoA-ToA space. Based on the aforementioned signal model, we outline the cross-correlation-based and beamforming-based method in generating DoA-ToA power map. Following that, we discuss the recent development of high resolution beamforming based on sparse DoA. We further extend this idea to propose sparse DoA-ToA method.

3.2.1 Cross-correlation-based TDoA (XCorr)

We can find the ToA of a snap at the sensor by cross-correlating the snap with the time-series sensor data. Since a snap is unknown a priori, we do not know exactly the acoustic signal structure of the snap. In existing literature, snaps are usually approximated by segments of the time-series sensor data, which consists of distinct peaks [29], [37]. Let sensor m' be the reference sensor. In order to find the main peaks of the snaps in data of sensor m', the data is preprocessed to form an enveloped sensor data such as

$$\tilde{x}_{m'}(t_n) = \sqrt{x^2_{m'(t_n)} + \mathbb{H}[x_{m'}(t_n)]^2} \tag{3.5}$$

where $\mathbb{H}$ is the discrete Hilbert transform operator. The enveloped sensor data is the magnitude of analytic sensor data based on Hilbert transform. Enveloping sensor data reveals the instantaneous amplitude of the sensor data which is essential to find main peaks of the snaps. N peaks exceeding a selected threshold, denoted by u, of the enveloped sensor output are identified as snaps with the ToA at sensor m' indicated by $\zeta_{m',i}$ for snap $i = 1, 2, \cdots, N$. Let snap i be

$$s_i^{\text{ref}}(t_n) = \begin{cases} x_{m'}(t_n) & \text{if } |t_n - \zeta_{m',i}| \leq \frac{l_s}{2} \\ 0 & \text{otherwise} \end{cases} \tag{3.6}$$

Equation 3.6 defines estimated snap i extracted from the acoustic recording of sensor m'. The subtraction in $|t_n - \xi_{m',i}| \leq \frac{l_s}{2}$ determines the non-zero values of $s_i^{\text{ref}}(t_n)$ according to the time stamp of the estimated peak of snap, denoted by $\xi_{m',i}$, and the time length of snaps, denoted by l_s. The process of identifying snaps from the sensor array data is named as snap detection. TDoA of snap i between sensor m' and $m \neq m'$ can be obtained by solving

$$\arg \max_{-l_\text{l} \leq t \leq l_\text{l}} \left| \sum_n x_m(t_n) s_i^{\text{ref}}(t_n - t) \right| \tag{3.7}$$

where the TDoA is bounded by the maximum time lag l_l which is dependent on the size of the array. The DoA-ToA detection i, denoted by $(\phi'_i, \theta'_i, \Gamma'_i)$, maximizes the number of consistent TDoAs of snap i. Hence, we have $\{(\phi'_i, \theta'_i, \Gamma'_i)\}_{i=1}^N$ and without loss of generality, we can construct the DoA-ToA power map of this method, denoted by $\mathbf{z}^{\text{XCorr}}$, such that the non-zero elements are indexed by

$\{(\phi'_i, \theta'_i, \Gamma'_i)\}_{i=1}^{N}$ with amplitude 1 and other elements are zeros. Snap detection is sensitive to the threshold value u. A large u would result in the detector failing to pick up weak signals, whereas a small u would result in detecting too much noise. Furthermore, the use of cross-correlation for TDoA estimation is susceptible to error. This is due to the fact that multiple transient impulsive signals, which include snaps and the corresponding multipath signals, can be found within the maximum time lag of a particular snap. The acoustic signature between different arrivals cannot be easily distinguished. Interested readers can refer to [25], [40], [43] for further details regarding a variety of XCorr implementations.

3.2.2 Beamforming

3.2.2.1 Delay and sum (DAS)

The time domain DAS beamformer estimates the time domain propagating signals through coherent and incoherent sum of the propagating signals given the array sensor data [53]. Identifying high amplitude elements from the beamformed output yields DoA-ToAs of impulsive signals. Formally, the time domain DAS beamformed output can be written as

$$\alpha^{\mathrm{DAS}}(\phi, \theta, \Gamma) = \frac{1}{M} \sum_{m=1}^{M} x_m(\Gamma - \tau_m(\phi, \theta)) \tag{3.8}$$

where $(\phi, \theta, \Gamma) \in \mathcal{S}$. The vectorization of $\alpha^{\mathrm{DAS}}(\phi, \theta, \Gamma)$ for all the elements in $\mathcal{S}$ is denoted by $\boldsymbol{\alpha}^{\mathrm{DAS}}$ and the DoA-ToA instantaneous power map of the DAS beamforming-based method is simply $\mathbf{z}^{\mathrm{DAS}} = |\boldsymbol{\alpha}^{\mathrm{DAS}}|^2$. In fact, $\mathbf{z}^{\mathrm{DAS}}$ is noisy due to the high sidelobe of the DAS beamformer.

3.2.2.2 Hough

To reduce the noise in the instantaneous power map, the sensor array data can be preprocessed such that peaks of enveloped sensor data, exceeding the threshold u, are set to ones while others are set to zeros across all the sensors. Subsequently, the time domain beamformed output of the preprocessed sensor array data yields the DoA-ToA power map denoted by $\mathbf{z}^{\text{Hough}}$. We use superscript Hough for the annotation because it is analogous to finding multiple planes in the preprocessed sensor array data [38]. Like the cross-correlation-based TDoA method, choosing threshold u is non-trivial. This method resembles the DAS-based method for small u, while at large u, it suppresses weaker snaps. The original idea of the Hough-based method is proposed in [37], [38].

3.2.3 Exploring sparsity

3.2.3.1 Block-Sparse (BS)

With the assumption that only a small number of wideband signals arrive at the array in the observation window, a DoA estimation technique based on the assumption of sparse DoA has been proposed [54] [52]

$$\hat{\mathbf{c}}^{\text{BS}} = \min_{\mathbf{c}} \frac{1}{2}\|\mathbf{A}\mathbf{c} - \mathbf{x}\|_2^2 + \lambda \sum_{b=1}^{|\mathcal{B}|} \|\mathbf{c}_b\|_2 \tag{3.9}$$

and a more intuitive form of this beamformer based on basis pursuit denoising (BPDN) is given by [55]

$$\hat{\mathbf{c}}^{\mathrm{BS}} = \min_{\mathbf{c}} \sum_{b=1}^{|\mathcal{B}|} \|\mathbf{c}_b\|_2$$
$$\text{s.t. } \|\mathbf{A}\mathbf{c} - \mathbf{x}\|_2 \leq \epsilon. \tag{3.10}$$

The solution of Equation 3.10 $\hat{\mathbf{c}}^{\mathrm{BS}}$ is an estimate of $\mathbf{c}$ in Equation 3.3 based on the objective function, L1/L2-norm. This mixed norm enforces block-sparsity on the solution which promotes spatially sparse wideband signal reconstruction [56]. ϵ^2 denotes the upper bound on the noise power of the signal model. λ controls the tradeoff between model misfit and block-sparsity of the solution. In order to have a stable recovery for block-sparse solution using Equation 4.15 and Equation 3.10, the coherence of $\mathbf{A}$, defined by the maximum off-diagonal element of absolute Gram matrix of $\mathbf{A}$, has to be low [55], [57]. A simple way to reduce the coherence of $\mathbf{A}$ is to use a non-periodic array [57]. Let

$$\mathbf{V} = \frac{1}{\sqrt{T}} \begin{pmatrix} \exp(-\mathrm{j}2\pi f_0 t_0) & \cdots & \exp(-\mathrm{j}2\pi f_0 t_{T-1}) \\ \vdots & \ddots & \vdots \\ \exp(-\mathrm{j}2\pi f_{T-1} t_0) & \cdots & \exp(-\mathrm{j}2\pi f_{T-1} t_{T-1}) \end{pmatrix} \tag{3.11}$$

be the discrete Fourier transform matrix and $\mathbf{W}$ be the block diagonal matrix of $\mathbf{V}$. The DoA-ToA power map of the BS method can be computed such as $\mathbf{z}^{\mathrm{BS}} = |\mathbf{W}^{\mathsf{H}}\hat{\mathbf{c}}^{\mathrm{BS}}|^2$. However, the wideband characteristic imposed by BS method is necessary but not sufficient to describe a impulsive transient signal since wideband signal can be non-impulsive and/or non-transient. For instance, Equation 3.10 can be rewritten as

$$\hat{\boldsymbol{\alpha}}^{\mathrm{BS}} = \min_{\boldsymbol{\alpha}} \sum_{b=1}^{|\mathcal{B}|} \|\mathbf{V}\boldsymbol{\alpha}_b\|_2$$
$$\text{s.t. } \|\mathbf{A}\mathbf{W}\boldsymbol{\alpha} - \mathbf{x}\|_2 \leq \epsilon \tag{3.12}$$

where $\mathbf{c}_b^{\mathrm{BS}} = \mathbf{V}\boldsymbol{\alpha}_b^{\mathrm{BS}}$ is the time domain beamformed output in direction b. Since $\mathbf{V}$ is a unitary matrix, minimizing $\|\mathbf{V}\boldsymbol{\alpha}_b^{\mathrm{BS}}\|_2 = \|\boldsymbol{\alpha}_b^{\mathrm{BS}}\|_2$ does not impose sparsity on the time domain beamformed output signal in direction b. This is in contrast with the prior knowledge of the transient impulsive signal which has sparse support in the time domain.

3.2.3.2 Sparse (S) – proposed method 1

The time domain beamformed output of the transient impulsive signal should be sparse in both DoA and ToA. We can reformulate Equation 3.3 as

$$\mathbf{x} = \mathbf{A}\mathbf{W}\boldsymbol{\alpha}. \tag{3.13}$$

and a sparse solution of $\boldsymbol{\alpha}$ can be recovered via

$$\hat{\boldsymbol{\alpha}}^{\mathrm{S}} = \min_{\boldsymbol{\alpha}} \|\boldsymbol{\alpha}\|_0$$
$$\text{s.t. } \|\mathbf{A}\mathbf{W}\boldsymbol{\alpha} - \mathbf{x}\|_2 \leq \epsilon. \tag{3.14}$$

The time domain beamformed output $\hat{\boldsymbol{\alpha}}^{\mathrm{S}}$ is an estimate of the inverse DFT of $\mathbf{c}$ in Equation 3.3 based on the objective function, L0-norm, which calculates the total number of non-zero elements of a vector. Minimizing L0-norm yields the sparsest solution of Equation 3.13 and also the sparsest DoA-ToA power map. However, there is no efficient algorithm to solve Equation 3.14 to obtain the optimal solution. The closest possible convex relaxation of the problem is

$$\begin{aligned}\hat{\boldsymbol{\alpha}}^{\mathrm{S}} = &\min_{\boldsymbol{\alpha}} \|\boldsymbol{\alpha}\|_1 \\ &\text{s.t. } \|\mathbf{A}\mathbf{W}\boldsymbol{\alpha} - \mathbf{x}\|_2 \leq \epsilon\end{aligned} \tag{3.15}$$

which can be solved efficiently using either second-order cone program or first order method. Let the coherence of $\mathbf{A}$ be κ. The coherence of $\mathbf{AW}$ can be written as

$$\begin{aligned}\mu(\mathbf{AW}) &= \max_{i,j,i\neq j}\{|\mathbf{W}^{\mathsf{H}}\mathbf{A}^{\mathsf{H}}\mathbf{A}\mathbf{W}|_{(i,j)}\} \\ &\leq \kappa\mathbf{V}^{\mathsf{H}}\mathbf{V} \\ &= \kappa.\end{aligned} \tag{3.16}$$

This shows that the coherence of $\mathbf{AW}$ is upper bounded by coherence of $\mathbf{A}$. The property for allowing stable recovery is preserved. As a result, stable recovery of sparse solution using Equation 3.15 is feasible if we have $\mathbf{A}$ with low coherence.

3.2.3.3 reduced-Sparse (rS) – proposed method 2

To minimize the effect of steering and model mismatch, a very large sensing matrix $\mathbf{A}$ has to be constructed so that all the array responses of the signals can be accurately represented by linear combination of the columns of $\mathbf{A}$. Considering a discrete space of field of view be $-50°$ to $50°$ azimuth angle and $-20°$ to $20°$ elevation angle with the spacing of $0.5°$, and the discrete space of time of arrival be 0 to 4999 samples with the spacing of 1 sample, the dimensions of $\mathbf{A}$ based on an array with 500 sensors is in the order of millions times ten of millions while the dimensions of $\mathbf{W}$ is in the order of ten of millions times ten of millions. This leads to a computationally expensive optimization problem in Equation 3.14. An intuitive way to improve the efficiency of this method is to reduce the size of $\mathbf{A}$ and $\mathbf{W}$. Energy of the DAS beamformed output defined by

$$\mathbf{y}_b = \sum_{\Gamma} |\alpha(\phi_b, \theta_b, \Gamma)|^2. \tag{3.17}$$

can serve as an indicator to eliminate the obvious redundant DoAs and hence only a subset of $\mathcal{B}$ is retained to generate a reduced-size $\mathbf{A}$ and $\mathbf{W}$. Formally, this subset can be written as $\tilde{\mathcal{B}} = \{(\phi_b, \theta_b) \in \mathcal{B} | \mathbf{y}_b > \mathbb{P}_p[\mathbf{y}]\}$ where $\mathbb{P}_p[\mathbf{y}]$ refers to p^{th} percentile of the value in vector $\mathbf{y}$. To avoid any confusion, the method of using the complete matrices and reduced-size matrices are coined as S and reduced rS respectively. The sparse DoA-ToA power maps can be denoted as $\mathbf{z}^{\text{S}} = |\hat{\boldsymbol{\alpha}}^{\text{S}}|^2$ and $\mathbf{z}^{\text{rS}} = |\hat{\boldsymbol{\alpha}}^{\text{rS}}|^2$.

3.3 Discussion

3.3.1 DoA-ToA detection

In this section, we discuss a process to extract the DoA-ToA detection $\{(\phi_i, \theta_i, \Gamma_i)\}_{i=1}^{N}$ from the DoA-ToA power map $\mathbf{z}$. This is obvious for $\mathbf{z}^{\text{XCorr}}$ as the non-zero element of $\mathbf{z}^{\text{XCorr}}$ is exactly the DoA-ToA of the snaps. Other methods tend to recover the DoA-ToA power map of snaps based on different criteria. Since the acoustic signal of a snap spans more than one sample and the array responses of the adjacent DoAs are highly correlated, $\mathbf{z}^{\text{Hough}}$, $\mathbf{z}^{\text{DAS}}$, $\mathbf{z}^{\text{BS}}$, $\mathbf{z}^{\text{S}}$, and $\mathbf{z}^{\text{rS}}$, to some extent, comprise multiple high amplitude elements (main peak of the snaps) surrounded by low amplitude elements (acoustic signal of a snap besides the main peak, spatial leakage of the snaps, sensor noise and etc.). Locating these high amplitude elements gives the DoA-ToA detection.

Let $\triangle_\phi$, $\triangle_\theta$, and $\triangle_\Gamma$ be the threshold distances of the DoA-ToA detection. Let $\triangle_{\mathbf{z}}$ be the threshold amplitude of the DoA-ToA detection. The DoA-ToA detection $\mathcal{D}$ can be obtained using peak finding algorithm in a 3-dimensional space. This can be done firstly by setting the small value elements in $\mathbf{z}$ to zeros based on the threshold amplitude and then selecting local maximums among the adjacent non-zero elements. Closely located peaks are eliminated based on the threshold distance because these peaks are probably due to the acoustic variability of snap or spatial leakage through highly correlated array response in DoA. We summarize the peak finding algorithm in Algorithm 3.1. We present a simple example in Figure 3.2 to further illustrate the algorithm. For convenient visualization, the figure contains a rough sketch of $\mathbf{z}$.

Algorithm 3.1 Peak finding

Require: $\mathbf{z}$, $\mathcal{S}$, $\mathcal{D} = \emptyset$, $\triangle_{\mathbf{z}}$, $\triangle_\phi$, $\triangle_\theta$, $\triangle_\Gamma$

1: $\tilde{\mathcal{S}}$ contains the indexes of local minimum of the thresholded $\mathbf{z}$ using $\triangle_{\mathbf{z}}$

2:
$$(\phi', \theta', \Gamma') = \arg \max_{(\phi,\theta,\Gamma)} \mathbf{z}_{(\phi,\theta,\Gamma)} \quad \text{s.t. } (\phi, \theta, \Gamma) \in \tilde{\mathcal{S}}$$

3: $\mathcal{Q} = \{(\phi, \theta, \Gamma) || \phi' - \phi| > \triangle_\phi, |\theta' - \theta| > \triangle_\theta, |\Gamma' - \Gamma| > \triangle_\Gamma, (\phi, \theta, \Gamma) \in \tilde{\mathcal{S}}\}$

4: $\tilde{\mathcal{S}} = \tilde{\mathcal{S}} \cap \mathcal{Q}$, $\mathcal{D} = \mathcal{D} \cup (\phi', \theta', \Gamma')$

5: repeat 2, 3, 4 until $\tilde{\mathcal{S}} = \emptyset$

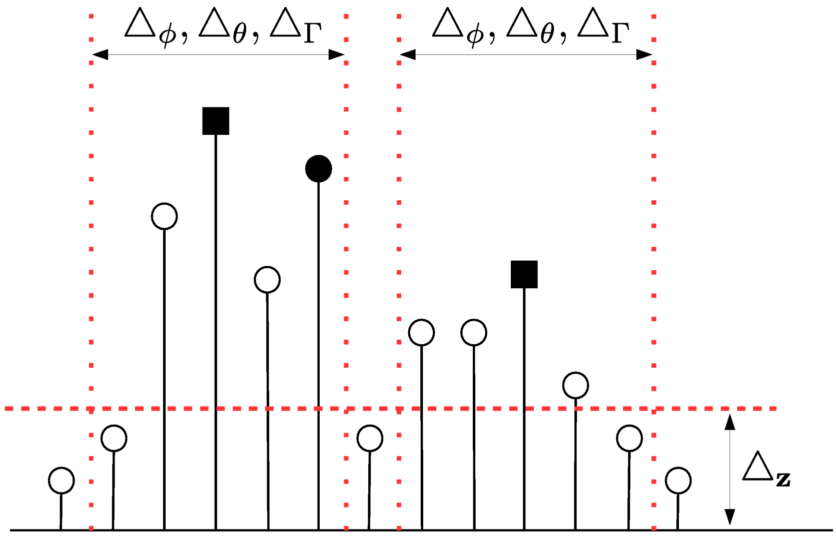

Figure 3.2: The two filled squares are the DoA-ToA detections. Both filled squares and filled circle are the selected peaks. The horizontal dashed line illustrates the threshold amplitude and the vertical lines show the threshold distances.

3.3.2 Practical considerations

The transient signal is sparse in time since it has very few non-zero samples within T. Reconstruction of a sparse time domain signal is feasible by randomly choosing a partial knowledge of its Fourier coefficients (Compressed Sensing) [58]. Random selection produces partial DFT matrix which satisfies the restricted isometry property (RIP) to ensure high probability of stable recovery using L1-minimization [59]. By randomly choosing a set of frequencies such that index of frequency $k \in \Omega \subset \{0, 1, \cdots, T-1\}$ we can reduce the memory requirement for storing huge $\mathbf{A}$. Within the observation period, the DoA of the signals is sparse in $\mathcal{B}$ which corresponds to a widely spread wavenumber (spatial frequency). High-resolution DoA estimation can be achieved by having a random sample of the spatial information using a sparse array.

Assuming a known noise power is impractical since the arrival of a snap is random. We can identify the main peaks of the snaps using simple thresholding and peak finding as described in the previous section. Then, we define the trimmed data of sensor m as

$$x^t_m(t_n) = \begin{cases} 0 & \text{if } t_n \in \{\zeta_{m,i}\}_{i=1}^{N_m} \\ x_m(t_n) & \text{if otherwise} \end{cases} \quad (3.18)$$

where $\zeta_{m,i}$ is a ToA of detected snap i at sensor m and N_m is the number of detected snaps at sensor m. We can estimate $\epsilon = \|\mathbf{x}^t\|_2$ where $\mathbf{x}^t$ is the Fourier coefficient vector of the trimmed sensor array data. By identifying and then eliminating the peaks of snaps observed in each sensor, we wish to obtain the sensor data without snaps so that they can be used to compute an upper bound of noise power for the optimization problem.

3.4 Numerical simulations

In this section, we study the detection performance of the aforementioned methods based on the simulated sensor array data of the impulsive transient signals in 3 different cases as shown in Table 3.1. The impulsive transient signal j was generated according to an exponentially damped sinusoid represented as

$$s_j(t) = \begin{cases} \beta_j \exp(-bt_n)\cos(2\pi f^{\mathrm{s}} t_n), & \text{if } t_n \geq 0 \\ 0, & \text{otherwise} \end{cases} \quad (3.19)$$

where β_j is the amplitude of the main peak of signal j, b is the decay constant, and f^{s} is the frequency of the sinusoid. $b = 10000$ and $f^{\mathrm{s}} = 30000$ Hz were chosen to imitate the transient and wideband behaviour of the snaps. Figure 3.3 shows the unit amplitude time domain simulated signal. Two signals were generated in case 1 and case 2. The signals were purposely simulated with DoA-ToAs close to each other in case 2. Case 3 is similar to case 2 with the additional three weak signals. ROMANIS was used to record all of these signals which were contaminated by independent and identically distributed (IID) Gaussian noise of zero mean and variance σ^2, with the peak signal to noise ratio (PSNR) defined by

$$\mathrm{PSNR} = 10 \log \left(\frac{\frac{1}{J} \sum_j \beta_j^2}{\sigma^2} \right). \tag{3.20}$$

Two plots of simulated observed signals of a sensor are shown in Figure 3.4, one without noise and the other with noise. Let $\mathcal{S} = \mathcal{S}_\phi \cup \mathcal{S}_\theta \cup \mathcal{S}_\Gamma$ where the set of azimuth angles $\mathcal{S}_\phi = \{-20°, -19.5°, \cdots, 20°\}$, the set of elevation angles $\mathcal{S}_\theta = \{-20°, -19.5°, \cdots, 20°\}$ and the set of time of arrivals $\mathcal{S}_\Gamma = \{0, 1, \cdots, 499\}$. We set the threshold u to 99.0^{th} percentile of the sensor data for snap detection. u is a small positve real value smaller and close to 99.9^{th} in order to avoid false positive snap detection from the sensor data. The typical maximum time lag of XCorr is the diameter of the receiver divided by speed of sound which gives 0.844 ms. Array response $\mathbf{A}$ was generated by randomly selecting 64 frequency points while the reduced-size $\mathbf{A}$ was based on 90^{th} percentile of the energy of the DAS beamformed output. We computed $\mathbf{z}^{\mathrm{XCorr}}$, $\mathbf{z}^{\mathrm{Hough}}$, $\mathbf{z}^{\mathrm{DAS}}$, $\mathbf{z}^{\mathrm{BS}}$, $\mathbf{z}^{\mathrm{S}}$, and $\mathbf{z}^{\mathrm{rS}}$ accordingly. Optimization toolbox, SPGL1, was used to solve for $\mathbf{z}^{\mathrm{BS}}$, $\mathbf{z}^{\mathrm{S}}$, and

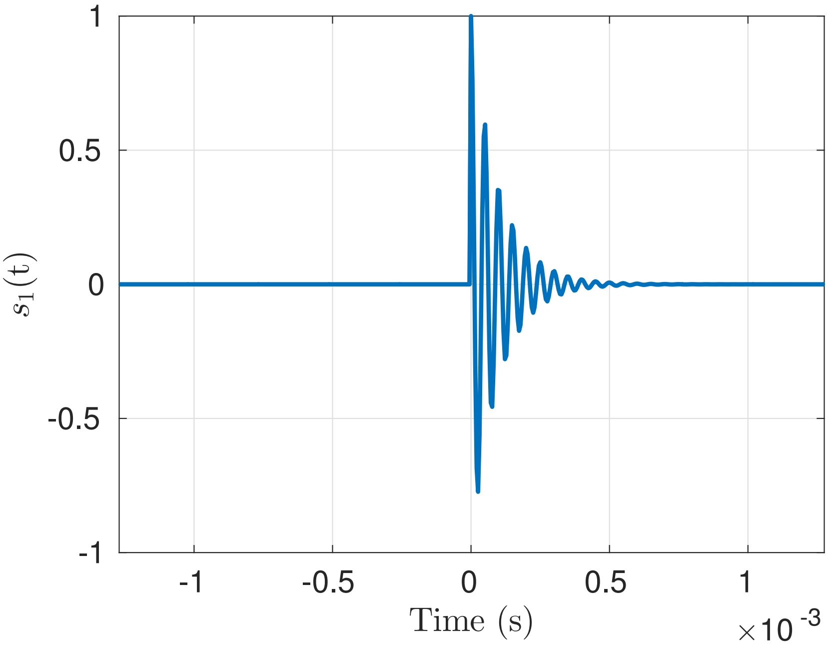

Figure 3.3: Time domain simulated s_1.

$\mathbf{z}^{\mathrm{rS}}$ [60], [61].

TABLE 3.1: Simulation setup.

Case	Signal	β	ϕ	θ	ΓF_{s} (sample)
1	s_1	1.0	$-6.3°$	$-8.1°$	49.2
	s_2	1.0	$-6.1°$	$5.2°$	249.3
2	s_1	1.0	$-6.3°$	$3.4°$	49.2
	s_2	1.0	$-6.1°$	$5.1°$	72.3
3	s_1	1.0	$-6.3°$	$3.4°$	49.2
	s_2	1.0	$-6.1°$	$5.2°$	72.3
	s_3	0.8	$5.8°$	$4.2°$	125.7
	s_4	0.8	$11.1°$	$-3.8°$	230.3
	s_5	0.8	$2.4°$	$9.6°$	400.8

Given the DoA-ToA power maps, DoA-ToA detections were obtained based on $\triangle_\phi = 1°$, $\triangle_\theta = 1°$ while $\triangle_\Gamma = 0.510$ ms is the time length of a snap. The detected DoA-ToA is true positive (TP) if it is within the threshold distance of the actual DoA-ToA. The true positive rate (TPR) is the number of TP divided

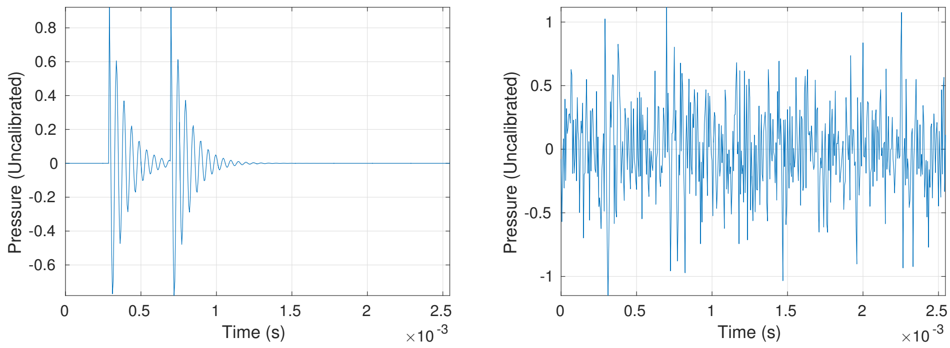

(a) Without noise. (b) With noise at 10 dB PSNR

Figure 3.4: Acoustic pressure recording of a sensor for two simulated signals.

by the number of actual DoA-ToA. False positive count (FPC) is defined by the number of detections which is beyond the threshold distance of the actual DoA-ToA. By varying the threshold amplitude, the TPR vs FPC curves were plotted based on the average of 50 noise realizations. We defined low PSNR as 10 dB and high PSNR as 20 dB in all cases.

The discussion on the detection performance using varies methods is shown in Figure 3.5. As the amplitude of the non-zero elements of $\mathbf{z}^{\mathrm{XCorr}}$ are the same, there is only one point in all of the TPR vs FPC plots for XCorr regardless of the threshold amplitude. In case 1, DAS, S, and rS methods achieve ideal detection performance, i.e., TPR=1, FPC=0, by choosing the right threshold amplitude. Others approach close to the ideal detection performance with a small number of FPC. Similar observations can be obtained in the result of case 2 except that the detection performance of XCorr and Hough degrade extensively in case 2. When the TDoA of two signals is less than the maximum time lag of XCorr, the method fails to identify the snap across sensors using cross-correlation. When two signals are close in DoA and ToA, Hough suffers from a large number of false positive detections. In case 3, XCorr, Hough, and BS have poor detection performance compared to the other methods.

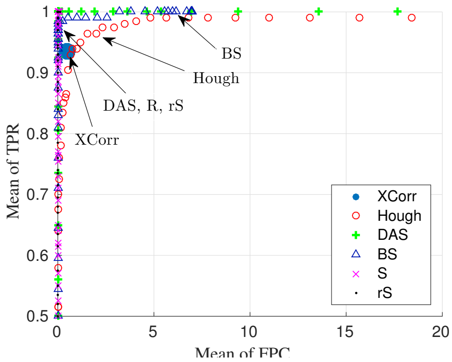

(a) Case 1.

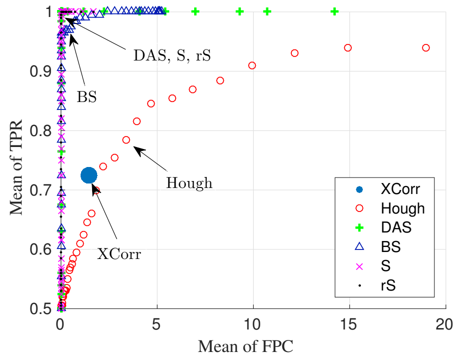

(b) Case 2.

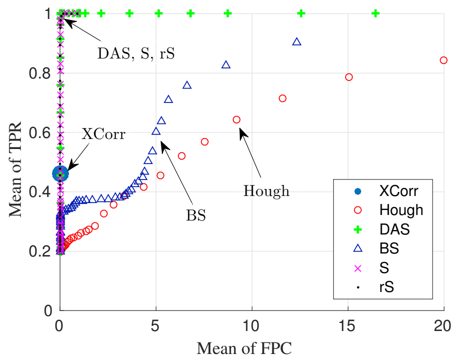

(c) Case 3.

Figure 3.5: Simulations at 10 dB PSNR.

Using the complete set of 508 sensors of ROMANIS, we noticed that DAS, S and rS are able to achieve ideal detection performance in all the simulated cases. To differentiate the performance among these methods, we reduced the effective diameter of ROMANIS by considering sensors within the radius of 0.3 m as shown in Figure 3.6 and recomputed case 3. A small aperture receiver is always preferable provided the detection performance can be maintained. However, this effectively decreases the resolution and PSNR of the receiver. In Figure 3.7, the detection performance of S and rS surpass that of DAS when using the scaled-down array in case 3. One of the reasons is that DAS seems to be easily susceptible to false positive detection at 10 dB and 20 dB PSNR. In general, the detection performances of S and rS are fairly consistent and are robust in a variety of circumstances such as the simulated cases. Even though rS uses the reduced-size **A**, it does not suffer performance degradation in detecting the DoA-ToA of snaps.

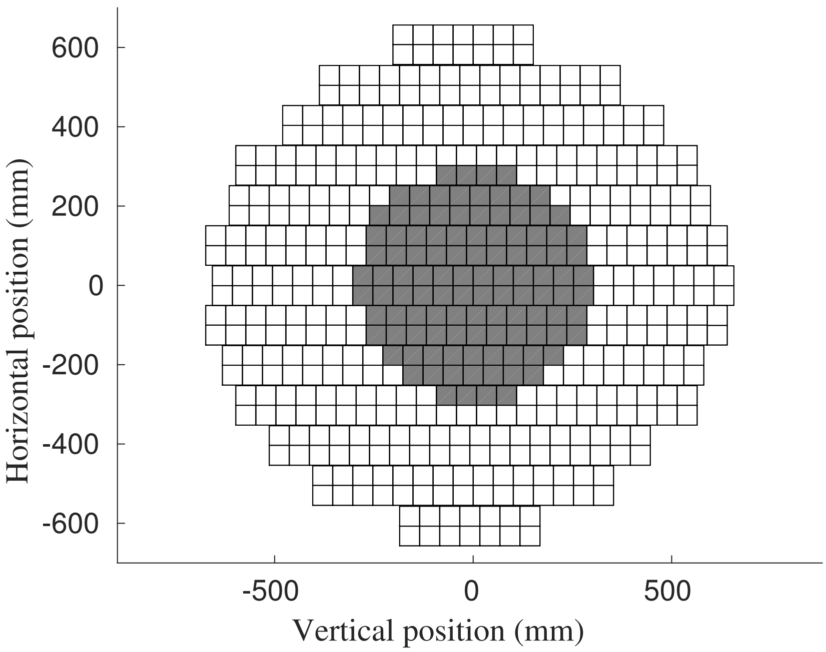

Figure 3.6: Sensor placement of scaled-down ROMANIS. The gray color sensors are those used in the simulation.

3.5 Summary

In this chapter, we discussed the transient impulsive signal model based on an array of sensors. We outlined the existing methods in detecting DoA-ToA of the impulsive transient signals such as those originating from snapping shrimp. We

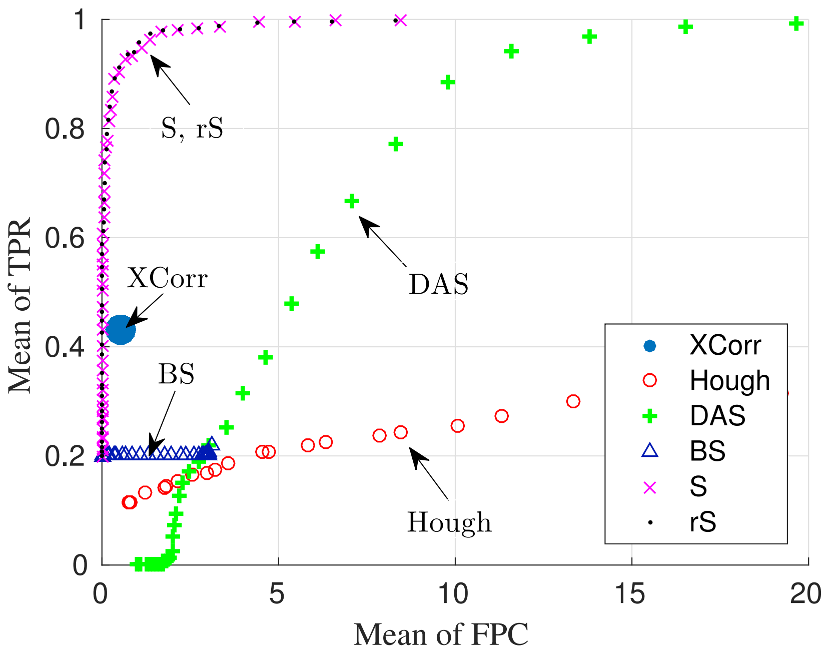

(a) Case 3 at 10 dB

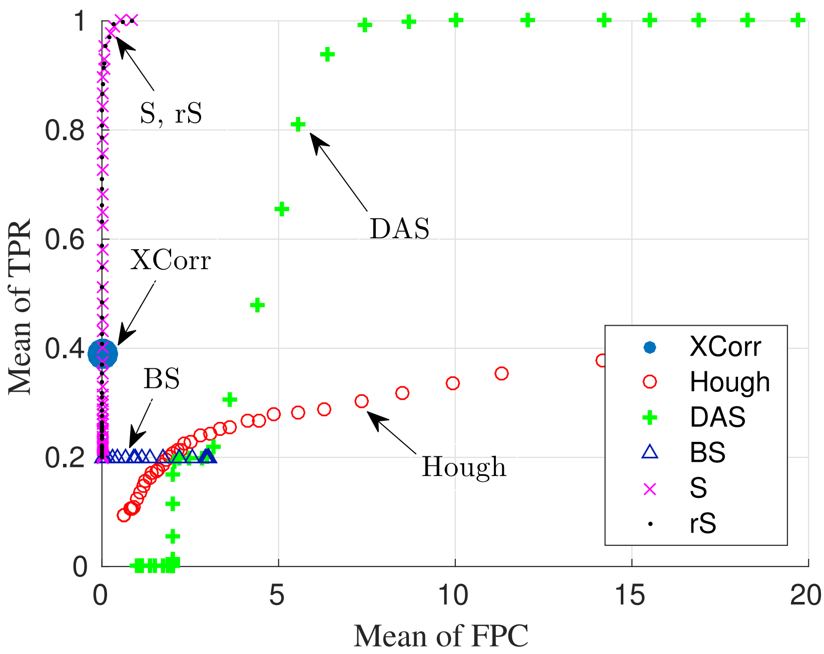

(b) Case 3 at 20 dB

Figure 3.7: TPR vs FPC plot of case 3 using the scaled-down ROMANIS.

explored the option of using sparse DoA-ToA as the prior knowledge of the signal support in detecting the DoA-ToA of these impulsive signals. We demonstrated that the proposed method has several advantages over the existing methods via numerical simulations. We will revisit the performance of these methods based on experimental results in Chapter 6.

Chapter 4

Geometric models of the direct arrival and surface-reflected snaps

In the previous chapter, we studied the DoA-ToA detection problem of impulsive transient signals such as those produced by the snapping shrimp, and proposed a sparse estimation method which overcomes the limitations of existing methods by its ability to distinguish similar arrivals which are adjacent in DoA or ToA. However, DoA-ToAs do not convey range information of far-field arrivals and hence, we cannot estimate the location of snaps. Given that water surface is like an acoustic reflector, we are able to associate the direct and surface-reflected snaps. In this chapter, we formulate geometric models by considering an effectively larger virtual array consisting of the actual array and its image above the water surface. This enables us to construct a range estimator for the snap by measuring the TDoA between the direct and surface-reflected arrival.

4.1 2-dimensional geometric model

A snap generates multipath propagations in warm shallow waters. The primary propagating path is the direct arrival. The first order propagating paths are the reflections at air-water interface and water-seabed interface, namely the surface and bottom reflections. The reflection coefficient is approximately -1 for a snap reflected at the water-air interface so the surface reflection is the same as the direct arrival with 180° phase inversion [62]. Due to the high absorption loss, especially in areas with sandy seabed, the bottom reflection and higher order propagations are ignored. For simplicity, we assume that water surface is calm and flat, and that both direct and surface-reflected arrival propagate in the same azimuth angle. The reason for both arrivals propagating at the same azimuth angle is the fact that the orientation of the receiver is unperturbed such that the broadside of the receiver is parallel to the water surface and the z-axis of the receiver is perpendicular to the water surface. This yields a 2-dimensional geometric model as shown in Figure 4.1.

In Figure 4.1(a), azimuth angles of the direct and surface reflection of snap i are the same, and are denoted by ϕ_i. In Figure 4.1(b), elevation angles of the direct and surface reflection of snap i are denoted by θ_i^d and θ_i^r respectively. Elevation angle ϕ_i carries a positive sign if it is above the OA line parallel to water surface. R_i and D_i are the distances traveled from the origin of snap i to the receiver. The ToA of the direct and surface reflection of snap i are τ_i^d and τ_i^r. During the observation period, we assume that the nominal depth of the receiver h is constant.

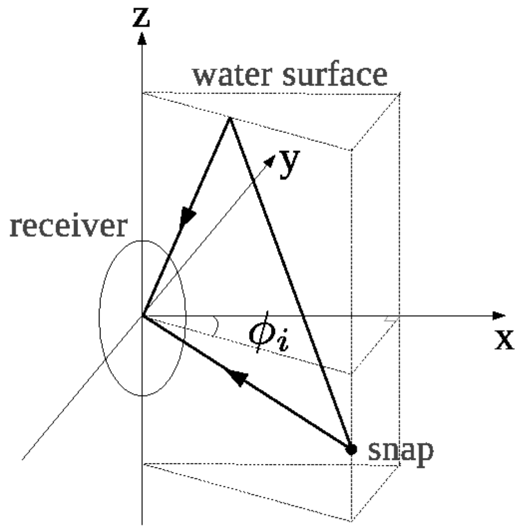

(a) 3-dimensional view

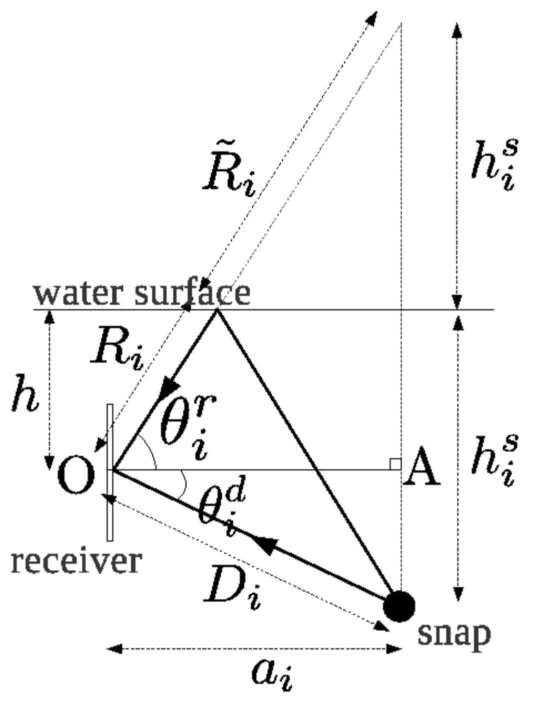

(b) Cross-sectional view

Figure 4.1: 2-dimensional geometric model with two arrows indicating direct arrival and surface reflection of a snap. (a) shows a 3-dimensional view of the direct and surface reflection of snap i. (b) shows the cross-sectional view of the snap propagating at azimuth angle ϕ_i.

We have

$$\cos(\theta_i^d) = \frac{a_i}{D_i}, \tag{4.1}$$

$$\cos(\theta_i^r) = \frac{a_i}{R_i + \tilde{R}_i}, \tag{4.2}$$

and

$$\delta_i = R_i + \tilde{R}_i - D_i \tag{4.3}$$

where $\delta_i = c(\tau_i^r - \tau_i^d)$ and c is the underwater speed of sound. Equation 4.1-4.3 can be written compactly as

$$\delta_i = a_i \left(\frac{1}{\cos(\theta_i^r)} - \frac{1}{\cos(\theta_i^d)} \right). \tag{4.4}$$

Equating the two vertical distances h_i^s, we derive

$$|d - a\tan(\theta_i^d)| = a\tan(\theta_i^r) - d. \tag{4.5}$$

By squaring both sides of Equation 4.5 and selecting the non-trivial solution, we obtain

$$a_i = \frac{2h}{\tan(\theta_i^d) + \tan(\theta_i^r)}. \tag{4.6}$$

The range of snap i can be written as

$$D_i = \frac{2h\cos(\theta_i^r)}{\sin(\theta_i^d + \theta_i^r)} \tag{4.7}$$

based on Equation 4.1 and 4.5. Finally, the location of snap i is

$$\mathbf{\Lambda}_i = D_i \begin{pmatrix} \cos(\phi_i)\cos(\theta_i^d) \\ \sin(\phi_i)\cos(\theta_i^d) \\ \sin(\theta_i^d) \end{pmatrix} \tag{4.8}$$

according to the Cartesian coordinate system in Figure 4.1. Note that D_i' is parameterized by h which is only known approximately and requires an ensemble of arrivals to improve the a priori knowledge.

Using ROMANIS, we collected ambient noise acoustic pressure data at Selat Pauh anchorage in Singapore waters which has an average depth of 15 m. The data is dominated by impulsive transient signals generated by snapping shrimp. DoA-ToA of the impulsive signals were identified and then associated into coarse direct and surface-reflected snaps. The computation method regarding the coarse pairing is discussed in the subsequent chapter. In concise description, this is a method which utilizes a few general physical properties of surface reflection to eliminate nuisance arrivals from the detected DoA-ToAs. At the moment, you may assume that the coarse direct and surface-reflected snap is a noisy association which we can easily derive from the DoA-ToA of impulsive transient signals. The coarse direct and surface reflection of snap i is represented by 3-tuple $((\phi_i, \theta_i^d), (\phi_i, \theta_i^r), \delta_i)$ where (ϕ_i, θ_i^d) is the azimuth and elevation angle of the direct arrival, and (ϕ_i, θ_i^r) is the azimuth and elevation angle of the surface reflection. Combining Equation 4.4 and Equation 4.6, we can relate the 3-tuple of coarse pair i by

$$\delta_i = 2h \left[\frac{\cos(\theta_i^d) - \cos(\theta_i^r)}{\sin(\theta_i^d + \theta_i^r)} \right]. \tag{4.9}$$

This relation is depicted in Figure 4.2 which displays the scatter points according to 3-tuple of the coarse pairs collected from the data. The gray curve represents Equation 4.9 and the majority of scatter points form a plane-like cluster on this curve, these being attributed to the correctly associated direct and surface-reflected snaps. The correct association is denoted by blue color. Points outside the cluster, denoted by red color, are likely to be the wrong associations. This shows that the experimental data in Singapore waters, to some extent, agrees with the geometric model of the direct arrival and surface-reflected snaps.

However, this model assumes that both direct and surface reflection have the same azimuth angle, that the water surface is completely flat, and that the orientation of the receiver is aligned with the water surface. The real sensor array data may not completely fit into this simple geometric model.

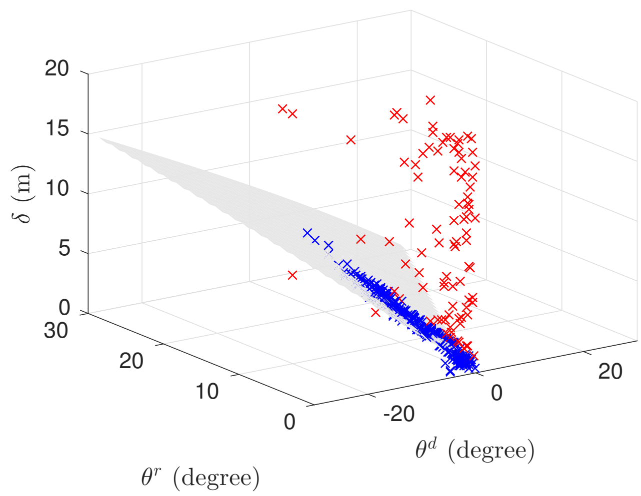

Figure 4.2: Scatter plot of the δ_i, θ_i^d, and θ_i^r based on the coarse direct and reflection arrivals generated by acoustic recording in Singapore waters. Points, which fit well on the the curve, are labeled in blue color while others are in red color.

4.2 3-dimensional geometric model

By relaxing the aforementioned assumptions, we present a more general form of geometric model in this section. We set up a right-handed coordinate system with its origin at the acoustic center of the receiver, x-axis pointing along the broadside direction, and y-axis pointing along the row of sensors. Let $\mathbf{d}_i$ and $\mathbf{r}_i$ be the direction unit vectors of the direct and reflected arrival pair i respectively. These unit vectors are the generalization of θ_i^d and θ_i^r with different azimuth angles. We consider $\hat{\mathbf{d}}_i$, $\hat{\mathbf{r}}_i$, and δ_i to be the measured quantities for each snap i.

Let $D_i\hat{\mathbf{d}}_i$ be the position vector of the snap i. Let $R_i\hat{\mathbf{r}}_i$ be the position vector of the point of reflection in the ocean surface, and $\hat{\mathbf{n}}_i$ be the unit vector normal to the surface (pointing downwards) at that point. We assume the undisturbed ocean surface to be a plane given by the equation $\mathbf{x}^\mathsf{T}\hat{\mathbf{s}} = h + \eta_i$ where $\mathbf{x}$ is any point on the surface, $\hat{\mathbf{s}}$ is normal to the surface (pointing upwards), and η_i is the depth deviation from the nominal water depth, h, due to wave motion. $\hat{\mathbf{s}}$ effectively captures the exact orientation of the receiver on the sea floor. We assume that h and $\hat{\mathbf{s}}$ do not change over the observation period, but are unknown. In practice, we may know them approximately. Figure 4.3 displays the geometry of a direct and surface-reflected arrival pair.

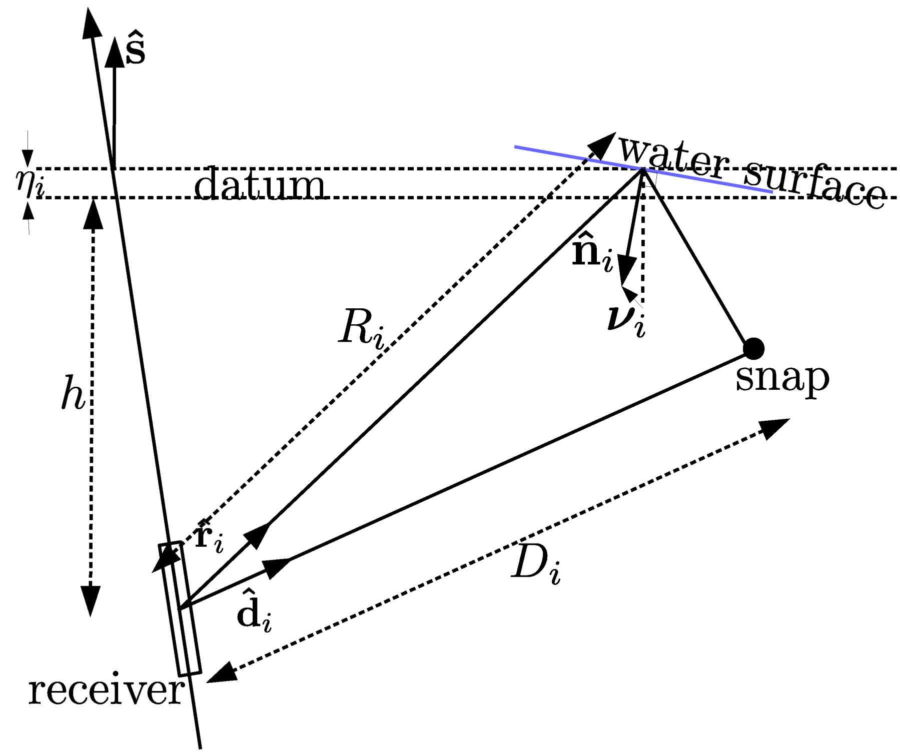

Figure 4.3: 3-dimensional geometric illustration of a direct and surface-reflected arrival pair.

The path length difference δ_i is given by

$$\delta_i = R_i + |D_i\hat{\mathbf{d}}_i - R_i\hat{\mathbf{r}}_i| - D_i. \tag{4.10}$$

Rearranging and squaring both sides, we get

$$R_i = \frac{\delta_i^2/2 + D_i\delta_i}{D_i + \delta_i - D_i\hat{\mathbf{d}}_i^\mathsf{T}\hat{\mathbf{r}}_i}. \tag{4.11}$$

Since the point of reflection must lie on the ocean surface, the perturbed nominal water depth can be written as

$$R_i\hat{\mathbf{r}}_i^\mathsf{T}\hat{\mathbf{s}} = h + \eta_i \tag{4.12}$$

which is the projection of $R_i\hat{\mathbf{r}}$ onto $\hat{\mathbf{s}}$. The normal vector $\mathbf{n}_i$ is given by

$$\hat{\mathbf{n}}_i = \mathbb{U}(\mathbb{U}(D_i\hat{\mathbf{d}}_i - R_i\hat{\mathbf{r}}_i) - \hat{\mathbf{r}}_i) \tag{4.13}$$

where $\mathbb{U}(\mathbf{x})$ is an operator generating a unit vector from vector $\mathbf{x}$. Since $\hat{\mathbf{r}}_i$, $\hat{\mathbf{n}}_i$ and $\hat{\mathbf{v}}_i = \mathbb{U}(D_i\hat{\mathbf{d}}_i - R_i\hat{\mathbf{r}}_i)$ are coplanar, there exists β_1 and β_2 such that $\hat{\mathbf{n}}_i = \beta_1\hat{\mathbf{v}}_i - \beta_2\hat{\mathbf{r}}_i$. Law of reflection ensures $-\hat{\mathbf{r}}_i^\mathsf{T}\hat{\mathbf{n}}_i = \hat{\mathbf{v}}_i^\mathsf{T}\hat{\mathbf{n}}_i$ so that $-\beta_1\mathbf{r}_i^\mathsf{T}\hat{\mathbf{v}}_i + \beta_2 = \beta_1 - \beta_2\hat{\mathbf{r}}_i^\mathsf{T}\hat{\mathbf{v}}_i$ which leads to $\beta_1 = \beta_2$. Since $\hat{\mathbf{n}}_i = \beta_1(\hat{\mathbf{v}}_i - \hat{\mathbf{r}}_i)$ and $\hat{\mathbf{n}}_i$ is a unit vector, $\beta_1 = \frac{1}{|\hat{\mathbf{v}}_i - \hat{\mathbf{r}}_i|}$ and thus $\hat{\mathbf{n}}_i = \mathbb{U}(\hat{\mathbf{v}}_i - \hat{\mathbf{r}}_i)$. This confirms the correctness of Equation 4.13.

In the case of a calm unperturbed water surface, $\hat{\mathbf{n}}_i = -\hat{\mathbf{s}}$ and $\eta_i = 0$. In the presence of waves, $\hat{\mathbf{n}}_i = -\hat{\mathbf{s}} + \boldsymbol{\nu}_i$ where $\boldsymbol{\nu}_i$ indicates the local roughness of the sea surface. Substituting Equation 4.13, we get

$$\mathbb{U}(\mathbb{U}(D_i\hat{\mathbf{d}}_i - R_i\hat{\mathbf{r}}_i) - \hat{\mathbf{r}}_i) = -\hat{\mathbf{s}} + \boldsymbol{\nu}_i. \tag{4.14}$$

The left hand side of Equation 4.12 and Equation 4.14 depict the indirect noisy measurements of h and $\hat{\mathbf{s}}$ respectively. If h and $\hat{\mathbf{s}}$ are known and η_i is ignored, the range of snap i can be estimated based on

$$D_i' = \frac{\delta_i^2/2 - \frac{h}{\hat{\mathbf{r}}^\mathsf{T}\hat{\mathbf{s}}}\delta_i}{\frac{h}{\hat{\mathbf{r}}^\mathsf{T}\hat{\mathbf{s}}} - \frac{h}{\hat{\mathbf{r}}^\mathsf{T}\hat{\mathbf{s}}}\hat{\mathbf{d}}_i^\mathsf{T}\hat{\mathbf{r}}_i - \delta_i}. \tag{4.15}$$

Subsequently, the location of snap i is defined as

$$\mathbf{\Lambda}_i' = D_i'\left(\mathbf{T}\hat{\mathbf{d}}_i\right). \tag{4.16}$$

where $\mathbf{T}$ is the transformation of the receiver axes to the datum axes. Since $\hat{\mathbf{s}} = [\sin(\alpha^o), \sin(\rho^o)\cos(\alpha^o), \cos(\rho^o)\cos(\alpha^o)]^\mathsf{T}$ where α^o and ρ^o are the pitch and roll of the normal vector of datum, we can write the transformation matrix as

$$\mathbf{T} = \begin{bmatrix} \cos(-\alpha^o) & 0 & \sin(-\alpha^o) \\ 0 & 1 & 0 \\ -\sin(-\alpha^o) & 0 & \cos(-\alpha^o) \end{bmatrix} \begin{bmatrix} 1 & 0 & 0 \\ 0 & \cos(\rho^o) & -\sin(\rho^o) \\ 0 & \sin(\rho^o) & \cos(\rho^o) \end{bmatrix} \tag{4.17}$$

where the first matrix describes the pitch rotation at y-axis and second matrix is the roll rotation at x-axis according to the right-handed rule. Combining Equation 4.15 and 4.16, we notice that the estimated location of snap i is a function of h and $\hat{\mathbf{s}}$ if DoA-ToA of the direct and surface-reflected snap i is known.

Given the direct and surface-reflected snaps, and parameters h and $\mathbf{s}$, we compute the δ_i for snap i by solving the nonlinear Equations 4.10, 4.12 and 4.14

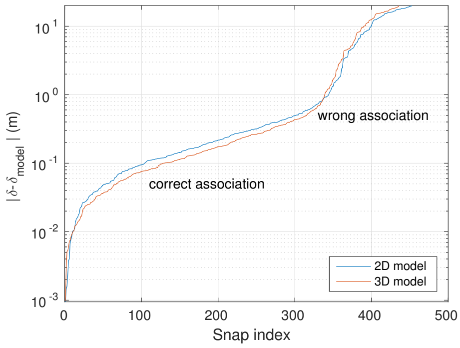

(a) Error plot with correct and wrong association.

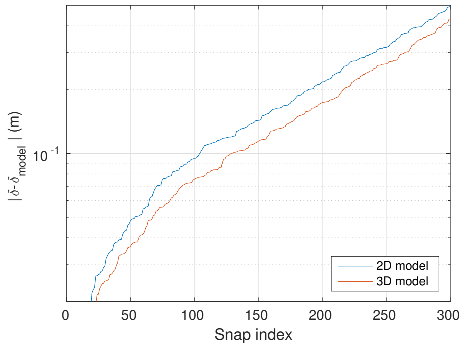

(b) Zoom-in view containing solely the correct association.

Figure 4.4: Absolute error of δ between measurement and geometric model with respect to snap index.

with $\eta_i = 0$ and $\boldsymbol{\nu}_i = \mathbf{0}$. We compare the measured path length difference using TDoA of direct and surface reflection, denoted by δ, with the geometric model-based path length difference, denoted by δ_{model} in Figure 4.4. The 2D geometric model is also included as a benchmark. The correct and wrong association of the direct and surface-reflected snaps can be easily shown since wrong association suffers from larger error compared to correct association. By considering receiver orientation, the 3D geometric model can better approximate the multipath propagation of the snap than the 2D geometric model and subsequently improves the agreement between δ and δ_{model} as shown in Figure 4.4(b).

4.3 Sensitivity analysis

The 3-dimensional geometric model is equivalent to the 2-dimensional geometric model if the ocean surface is unperturbed ($\eta_i = 0, \boldsymbol{\nu}_i = \mathbf{0}$) and the orientation of the receiver is aligned to the water surface, i.e., $\hat{\mathbf{s}} = [0, 0, 1]^{\mathsf{T}}$. As a result, the sensitivity analysis on the 3-dimensional geometric model is applicable to the 2-dimensional geometric model. For ease of notation, index i is omitted in this section. Let $\hat{\mathbf{d}}$, $\hat{\mathbf{r}}$, and δ be known exactly but not h and $\hat{\mathbf{s}}$. The range estimator in Equation 4.7 is a function of the prior knowledge of the parameters such that

$$D'(h+\epsilon_h, \hat{\mathbf{s}}+\boldsymbol{\epsilon}_{\hat{\mathbf{s}}}) = \frac{\delta^2/2 - \frac{h+\epsilon_h}{\hat{\mathbf{r}}^\mathsf{T}(\hat{\mathbf{s}}+\boldsymbol{\epsilon}_{\hat{\mathbf{s}}})}\delta}{\frac{h+\epsilon_h}{\hat{\mathbf{r}}^\mathsf{T}(\hat{\mathbf{s}}+\boldsymbol{\epsilon}_{\hat{\mathbf{s}}})} - \frac{h+\epsilon_h}{\hat{\mathbf{r}}^\mathsf{T}(\hat{\mathbf{s}}+\boldsymbol{\epsilon}_{\hat{\mathbf{s}}})}\hat{\mathbf{d}}^\mathsf{T}\hat{\mathbf{r}} - \delta}. \tag{4.18}$$

where the a priori parameters ($h+\epsilon_h$, $\hat{\mathbf{s}}+\boldsymbol{\epsilon}_{\hat{\mathbf{s}}}$) are defined by the summation of the actual value of the parameters (h, $\hat{\mathbf{s}}$) and the errors (ϵ_h, $\boldsymbol{\epsilon}_{\hat{\mathbf{s}}}$).

To simplify the notation, we define $R' = \frac{h}{\hat{\mathbf{r}}^\mathsf{T}\hat{\mathbf{s}}}$ which linearises the parameter errors such that $R' + \epsilon_{R'} = \frac{h+\epsilon_h}{\hat{\mathbf{r}}^\mathsf{T}(\hat{\mathbf{s}}+\boldsymbol{\epsilon}_{\hat{\mathbf{s}}})}$. Hence, we can write

$$D'(R'+\epsilon_{R'}) = \frac{\frac{\delta^2}{2} - (R'+\epsilon_{R'})\delta}{(R'+\epsilon_{R'}) - (R'+\epsilon_{R'})\hat{\mathbf{d}}^\mathsf{T}\hat{\mathbf{r}} - \delta} \tag{4.19}$$

where $\epsilon_{R'}$ is related to ϵ_h and $\boldsymbol{\epsilon}_{\hat{\mathbf{s}}}$. The range estimation error due to the a priori parameters can be written as

$$D'(R'+\epsilon_{R'}) - D'(R') = D'(R')\epsilon_{R'}\left[-\frac{1}{R'+\epsilon_{R'}+\frac{\delta}{-1+\hat{\mathbf{d}}^\mathsf{T}\hat{\mathbf{r}}}}\right] \tag{4.20}$$

The magnitude of the estimation error turns out to be

$$|D'(R'+\epsilon_{R'}) - D'(R')| \propto D'(R')|\epsilon_{R'}|. \tag{4.21}$$

We notice that the error is linearly proportional to the range of the snap.

We are also interested in identifying which parameter is more significant in generating larger range estimation error. The previous paragraph has shown the direct relation between $|\epsilon_{R'}|$ and the range estimation error. Thus, it is sufficient to just present the relation between $|\epsilon_{R'}|$ and the parameters. Let $\epsilon_{\hat{\mathbf{s}}} = 0$. We have

$$|\epsilon_{R'_1}| = \frac{1}{\hat{\mathbf{r}}^{\mathsf{T}}\hat{\mathbf{s}}}|\epsilon_h|. \tag{4.22}$$

Let $h = 0$. We have

$$\begin{aligned}|\epsilon_{R'_2}| &= \frac{1}{\hat{\mathbf{r}}^{\mathsf{T}}\hat{\mathbf{s}}}\left(\frac{h}{\hat{\mathbf{r}}^{\mathsf{T}}(\hat{\mathbf{s}}+\boldsymbol{\epsilon}_{\hat{\mathbf{s}}})}\right)|\hat{\mathbf{r}}^{\mathsf{T}}\boldsymbol{\epsilon}_{\hat{\mathbf{s}}}| \\ &\leq \frac{1}{\hat{\mathbf{r}}^{\mathsf{T}}\hat{\mathbf{s}}}\left(\frac{h}{\hat{\mathbf{r}}^{\mathsf{T}}(\hat{\mathbf{s}}+\boldsymbol{\epsilon}_{\hat{\mathbf{s}}})}\right)|\boldsymbol{\epsilon}_{\hat{\mathbf{s}}}| \end{aligned} \tag{4.23}$$

The upper bound is due to Cauchy-Schwarz inequality and $|\hat{\mathbf{r}}| = 1$ [63]. For comparison, we replace the magnitude of the errors by the same fractional perturbation, denoted by $0 \leq e \leq 1$, with respect to the magnitude of the parameters. This can be written as $|\epsilon_h| = eh$ and $|\boldsymbol{\epsilon}_{\hat{\mathbf{s}}}| = e|\hat{\mathbf{s}}| = e$. Equations (4.22) and (4.23) become

$$|\epsilon_{R'_1}| = \frac{h}{\hat{\mathbf{r}}^{\mathsf{T}}\hat{\mathbf{s}}}e, \tag{4.24}$$

$$|\epsilon_{R'_2}| \leq \frac{h}{\hat{\mathbf{r}}^{\mathsf{T}}\hat{\mathbf{s}}}\left(\frac{1}{\hat{\mathbf{r}}^{\mathsf{T}}(\hat{\mathbf{s}}+\boldsymbol{\epsilon}_{\hat{\mathbf{s}}})}\right)e. \tag{4.25}$$

Snaps are located in far-field and the receiver orientation is close to $[0,0,1]^{\mathsf{T}}$, and hence $0 < \hat{\mathbf{r}}^{\mathsf{T}}(\hat{\mathbf{s}}+\boldsymbol{\epsilon}_{\hat{\mathbf{s}}}) < 1$. When snaps are farther away, the value approaches 0, and when snaps are nearer, the value approaches 1. In general, the error of the receiver orientation is more significant than the error of the nominal receiver depth for range estimation error in the worst case scenario. For distant snaps, range estimation error due to inaccurate knowledge of receiver orientation is larger as compared to the error due to inaccurate knowledge of receiver depth.

4.4 Summary

In this chapter, we studied the far-field range estimation problem by firstly looking at the 2-dimensional geometric model of the direct arrival and surface-reflected snap. We recognized the limitations of this simple model and hence developed the more general 3-dimensional geometric model, which is based on less restrictive assumptions. Based on this model, we constructed the range estimator for the snap which is parametrized by the nominal water depth and the receiver orientation. We discussed the sensitivity of these parameters to the estimated range. We also showed that the error of receiver orientation has greater impact on the estimated range than the nominal water depth. We observed that the accuracy of the parameters is crucial for snapping shrimp range estimation. However at this juncture it is still unclear as to how better parameters can be obtained other than by using the prior knowledge. We will address this problem in the next chapter.

Chapter 5

Association and estimation problem in snap localization

In the previous chapter, we showed that estimated location of snap is a function of parameters h and $\hat{\mathbf{s}}$. However, by assuming prior knowledge of the parameters we may not be able to obtain accurate range estimation. In this chapter we propose a method to improve the knowledge of the parameters, with the assumption that these parameters remain constant over the observation period. In the first part, we assume that we know the associated direct and surface-reflected snaps so that we can obtain an estimator for the parameters. This assumption is not true in practice. However, it is important for the development of the method to improve the a priori knowledge of h and $\hat{\mathbf{s}}$ given a perfect association. Through numerical simulations, we will show that the derived method is capable of estimating the locations of snaps even if a small number of wrong associations of direct and surface-reflected snaps exist. Then, in the second part of the chapter, we relax the assumption of perfect association and establish a relatively comprehensive problem for snapping shrimp localization. An algorithm, which simultaneously associates the arrivals and estimates the parameters, is discussed.

5.1 Estimating the nominal water depth and receiver orientation

5.1.1 Formulation

Estimating h and $\hat{\mathbf{s}}$ from one associated direct and surface reflection arrival of snap is non-trivial since there are more unknowns than number of nonlinear equations. Let P be the number of associated direct and surface-reflected snaps collected during the observation period. The small variation over the nominal water depth h is represented by a set of IID random variables $\{\eta_i\}_{i=1}^P$, while the small variation in the water surface normal vector is represented by a set of IID random vectors $\{\nu_i\}_{i=1}^P$. Figure 5.1 depicts the 3-dimensional geometric model, showing multiple snaps reflected from different water surface conditions. Let h' and $\hat{\mathbf{s}}'$ be the estimates of h and $\hat{\mathbf{s}}$. Let $\{D_i\}_{i=1}^P$ be bounded by $\{[l_{D_i}, u_{D_i}]\}_{i=1}^P$ respectively, and considering R_i as a function of D_i, then the equations $\mathbb{U}(\mathbb{U}(D_i\hat{\mathbf{d}}_i - R_i\hat{\mathbf{r}}_i) - \hat{\mathbf{r}}_i) = -\hat{\mathbf{s}} + \boldsymbol{\nu}_i$ for $i = 1, 2, \cdots, P$ can be illustrated as a set of curves on an unit ball by varying $\{D_i\}_{i=1}^P$. All the curves should pass close to $\hat{\mathbf{s}}$ since they are shifted by $\{\boldsymbol{\nu}_i\}_{i=1}^P$ from $\hat{\mathbf{s}}$. According to $R_i\hat{\mathbf{r}}^\mathsf{T}\hat{\mathbf{s}} = h + \eta_i$, varying $\{D_i\}_{i=1}^P$ creates lines on h shifted by $\{\eta_i\}_{i=1}^P$. All the lines should lie in the vicinity of h. Estimating h and $\hat{\mathbf{s}}$ reduces to finding h' and $\hat{\mathbf{s}}'$ that is closest to all the curves and the lines. The closeness can be measured by the distance between the estimates and the points on the curves and the lines.

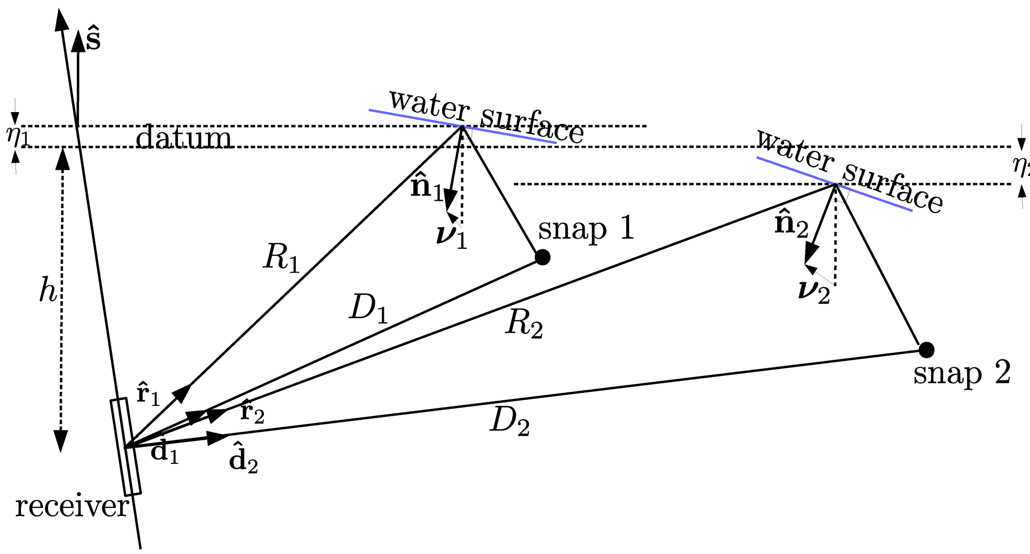

Figure 5.1: Geometric illustration of two direct and surface-reflected snaps.

We can write this as an optimization problem:

$$h', \hat{\mathbf{s}}' = \arg \min_{\tilde{h}, \tilde{\hat{\mathbf{s}}}: \|\tilde{\hat{\mathbf{s}}}\|_2 = 1} \sum_{i=1}^{P} \min_{l_{D_i} \leq \tilde{D}_i \leq u_{D_i}} \Big(\|\tilde{R}_i \hat{\mathbf{r}}_i^{\mathsf{T}} \tilde{\hat{\mathbf{s}}} - \tilde{h}\|_2^2$$

$$+ \lambda \|\tilde{\hat{\mathbf{s}}} + \mathbb{U}(\mathbb{U}(\tilde{D}_i \hat{\mathbf{d}}_i - \tilde{R}_i \hat{\mathbf{r}}_i) - \hat{\mathbf{r}}_i)\|_2^2 \Big) \tag{5.1}$$

where $\tilde{D}_i$ defines a point on the respective curve and line which has the shortest Euclidean distance from h' and $\hat{\mathbf{s}}'$, and $\tilde{R}_i$ is a function of $\tilde{D}_i$. $\lambda > 0$ is a tuning parameter controlling the relative importance of the closeness in the curves and closeness in the lines. Note that $\{\tilde{D}_i\}_{i=1}^{P}$ is not the estimate of $\{D_i\}_{i=1}^{P}$. It is used solely to describe the distribution of the curves and the lines.

Estimating h and $\hat{\mathbf{s}}$ involves solving nonconvex optimization problem in Equation 5.1. Considering a smooth bathymetry and calm sea state, we can initialize $\tilde{h}^{(0)}$ to the average nominal water depth at the receiver deployment location and $\tilde{\hat{\mathbf{s}}}^{(0)} = [0, 0, 1]^{\mathsf{T}}$ both values of which should be close to the actual h

and $\hat{\mathbf{s}}$. For $k = 1$ iteration, the single-variable inner minimization of Equation 5.1 can be efficiently solved for $\{\tilde{D}_i^{(k)}\}_{i=1}^P$ given $\tilde{h}^{(k-1)}$ and $\tilde{\hat{\mathbf{s}}}^{(k-1)}$. Subsequently, we solve the outer minimization of Equation 5.1 for $\tilde{h}^{(k)}$ and $\tilde{\hat{\mathbf{s}}}^{(k)}$ given $\{\tilde{D}_i^{(k)}\}_{i=1}^P$. The two-step minimization is repeated for the next iteration until the objective function value is lesser than a predefined positive small number. Let f be the objective function of Equation 5.1. The decrease of the objective function value over iterations can be shown as follows:

$$\begin{aligned} f(\tilde{D}_i^{(k)}, \tilde{h}^{(k)}, \tilde{\hat{\mathbf{s}}}^{(k)}) &\leq f(\tilde{D}_i^{(k)}, \tilde{h}^{(k-1)}, \tilde{\hat{\mathbf{s}}}^{(k-1)}) \\ &\leq f(\tilde{D}_i^{(k-1)}, \tilde{h}^{(k-1)}, \tilde{\hat{\mathbf{s}}}^{(k-1)}) \end{aligned} \tag{5.2}$$

for $k = 1, 2 \cdots$. This shows that local optimal estimates can be achieved.

The objective function in Equation 5.1 can be divided into two cost functions. The first cost is the distance between the estimate and the points on the lines while the second cost is the distance between the estimate and the points on the curves. For $\lambda \to 0$, the first cost dominates and $D_i^{(1)}$ can always be found such that the objective function value is close to zero regardless of $\tilde{h}^{(0)}$ and $\tilde{\hat{\mathbf{s}}}^{(0)}$ if the l_{D_i} and u_{D_i} are not tied. The local optimal estimates are simply the prior knowledge of the parameters. For $\lambda \to \infty$, the second cost dominates but it is less likely that we can find $\tilde{D}_i$ such that the objective function value is zero over the iterations. However, this might lead to over-fitting in $\hat{\mathbf{s}}$ and consequently yields large error in the estimate of h.

5.1.2 Numerical simulations

In this section, we verify the parameter estimation performance of the proposed method by adopting 2 different simulations. The first simulation features longer range and randomly distributed snaps, while the second simulation has shorter range and structurally distributed snaps. 2000 associated direct and surface-reflected snaps were generated based on $\eta_i \sim \mathcal{N}(0, (0.2\text{ m})^2)$ and

$$\begin{aligned}\boldsymbol{\nu}_i &= \hat{\mathbf{n}}_i + \hat{\mathbf{s}} \\ &= -\begin{bmatrix} \sin(\alpha_i + \alpha^o) \\ \sin(\rho_i + \rho^o)\cos(\alpha_i + \alpha^o) \\ \cos(\rho_i + \rho^o)\cos(\alpha_i + \alpha^o) \end{bmatrix} + \begin{bmatrix} \sin(\alpha^o) \\ \sin(\rho^o)\cos(\alpha^o) \\ \cos(\rho^o)\cos(\alpha^o) \end{bmatrix}\end{aligned} \tag{5.3}$$

for $i = 1, 2, \cdots, 1000$ where $\alpha_i \sim \mathcal{N}(0, 5^{\circ 2})$ and $\rho_i \sim \mathcal{N}(0, 5^{\circ 2})$ are the pitch and roll of the local water surface whereas α^o and ρ^o describe the orientation of the receiver. We fixed $l_{D_i} = 0$ m and $u_{D_i} = 300$ m for all i. The parameters were estimated using Equation 5.1. We displayed the estimated locations of snaps based on the actual and estimated parameters for comparison. The locations are modified such that the origin of z-axis is set on the water surface for convenient illustration.

In simulation 1, we set $h = 15$ m, $\alpha^o = -7^\circ$ and $\rho^o = -5$. The sources were uniformly distributed across $[-60^\circ, +60^\circ]$ in azimuth angle, $[-5^\circ, +10^\circ]$ in elevation angle and $[100\text{ m}, 200\text{ m}]$ in range. Let the average nominal water depth be $\tilde{h}^{(0)} = 14$ m. When $\lambda = 0$, we obtain $h' = \tilde{h}^{(0)}$ and $\hat{\mathbf{s}}' = \tilde{\hat{\mathbf{s}}}^{(0)}$ which yield estimated range error of approximately 100 m. This shows that using the prior knowledge parameters is not a reliable method for range estimation. The lowest estimation error of h' and $\hat{\mathbf{s}}'$ are attained at $\lambda = 5000$ and $\lambda = 7000$ respectively. This finding is reasonable as the estimator with larger λ tends to over-fit the curves which determine $\hat{\mathbf{s}}$. When λ is gradually reduced, more effort is given to minimizing the error in h. The calculated range of the snaps based on the estimated parameters is more accurate for large λ and better $\hat{\mathbf{s}}'$ estimate as shown in Figure 5.2(c) and Figure 5.2(d). This agrees with the previous result stating that the error in $\hat{\mathbf{s}}'$ is more significant than the error in h' for snaps that are farther apart from the receiver.

In simulation 2, we examine the capability of the method to estimate the parameters given that snaps are structurally distributed in space. We set $h = 5$ m, $\alpha^o = 7^\circ$ and $\rho^o = -5^\circ$. The snaps were uniformly generated within a rectangular space defined by $[10\text{ m}, 20\text{ m}]$ in x-axis, $[-20\text{ m}, 20\text{ m}]$ in y-axis, $[-1\text{ m}, 0\text{ m}]$ in z-axis, and two vertical spaces, both sharing the same interval $[-1\text{ m}, 2\text{ m}]$ in z-axis but with one at 10 m x-axis, $[9\text{ m}, 10\text{ m}]$ y-axis while the other at $[15\text{ m}]$ x-axis, $[-20\text{ m}, -19\text{ m}]$. Let the average nominal water depth be $h^{(0)} = 3$ m. According to Figure 5.3, the accuracy of D' is less dependent on $\hat{\mathbf{s}}'$ because this parameter becomes less significant when the range of the snap decreases. Similarly, there is a large estimation error for the range of the snaps parameterized by the prior knowledge of the parameters.

In short, a large λ, i.e., numbering a few thousands seems to be a reasonable amount for the two-step minimization. This is because the increment in the parameter estimation error is small for large λ. Even though a large λ does not produce optimal estimation for shorter range snaps such as those in simulation

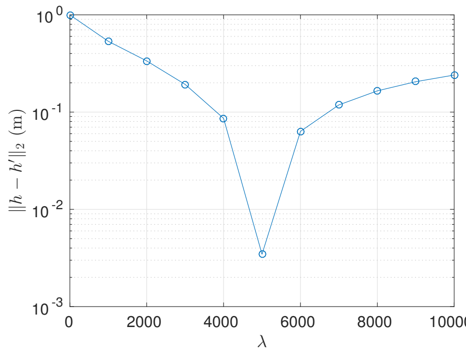

(a) Error of h'.

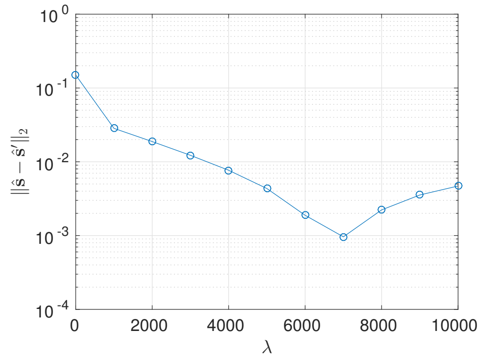

(b) Error of $\hat{\mathbf{s}}'$

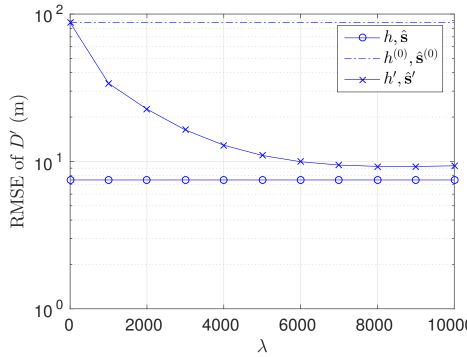

(c) Root-mean-square error (RMSE) of D' based on the actual, the prior knowledge and estimated parameters.

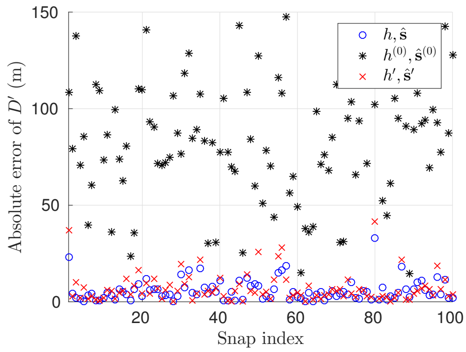

(d) Absolute error of the range based on the prior knowledge and the estimated parameters which were calculated using $\lambda = 8000$ as minimum RMSE of D' is achieved. Only estimated range of 100 snaps are plotted for the ease of visualization.

Figure 5.2: The accuracy of h' and $\hat{\mathbf{s}}'$ and the performance of the range estimator of snap using the parameters in simulation 1.

2, the parameter error is considerably small compared to the underestimated λ.

5.2 Association and estimation

To determine the snapping shrimp locations from DoA-ToA recording, there are two crucial pieces of information that need to be known in practice. One is the parameters of the range estimator like nominal water depth and receiver orientation. The other is the association of direct and surface-reflected snaps from multiple arrivals. If many snaps arrive at the origin of the receiver

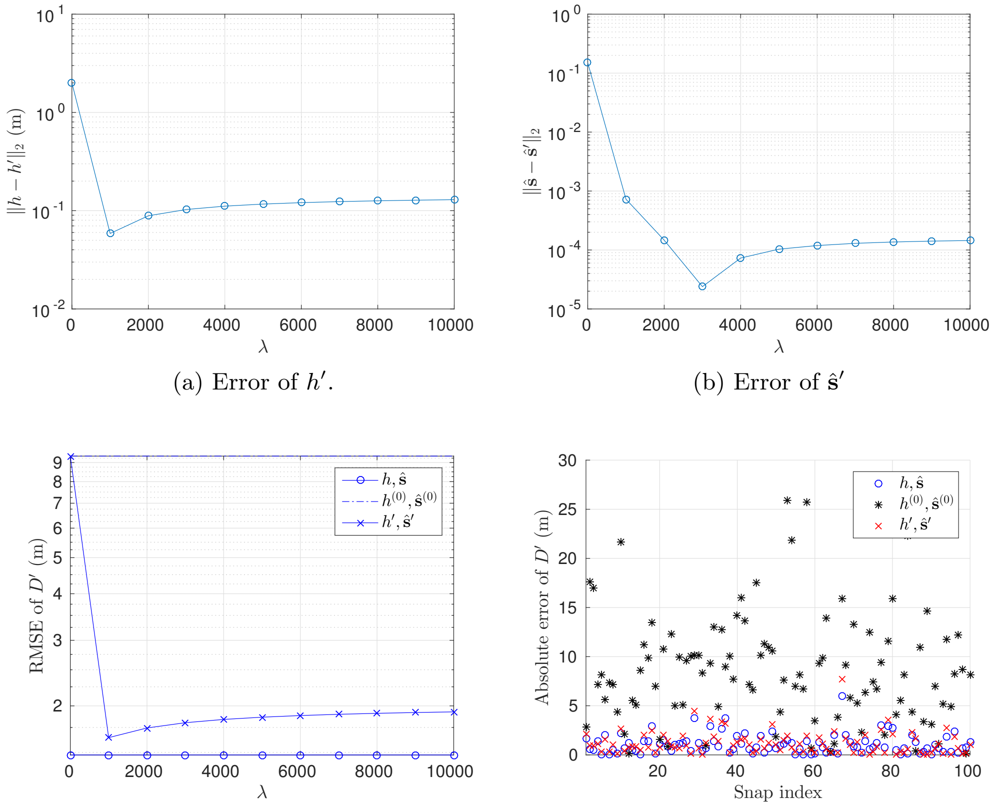

(a) Error of h'.

(b) Error of $\hat{\mathbf{s}}'$

(c) RMSE of D' based on the actual, the prior knowledge and the estimated parameters.

(d) Absolute error of the range based on the prior knowledge and the estimated parameters which were calculated using $\lambda = 1000$ as minimum RMSE of D' is achieved. Only estimated range of 100 snaps are plotted for the ease of visualization.

Figure 5.3: The accuracy of h' and $\hat{\mathbf{s}}'$ and the performance of the range estimator of snap using the parameters in simulation 2.

approximately at the same time, associating a snap with its reflection is a hard problem without the exact knowledge of the parameters describing the geometric model. Observing large number of arrivals potentially increases the number of wrong pairings if the geometric model is partially known. Given the DoA-ToA arrivals, we discuss a complete algorithm to solve the problem of snapping shrimp noise localization. We present the idea starting with the coarse pairing procedure which eliminates obvious wrong association among all the arrivals, followed by an algorithm to associate the arrivals and at the same time estimate the parameters.

5.2.1 Coarse pairing

If N arrivals are observed, we can form, at most, N^2 associated direct and surface-reflected snaps. For brevity we shall refer to the associated direct and surface-reflected snaps simply as pairs. These pairs include a large portion of wrong association. In fact, by removing the number of obviously wrong pairs, we can reduce the number of pairings from N^2 to P'. The P' pairs denoted by $\{\hat{\mathbf{d}}_i, \hat{\mathbf{r}}_i, \delta_i\}_i^{P'}$, where $\hat{\mathbf{d}}_i = [\cos(\phi_i^{\mathrm{d}})\cos(\theta_i^{\mathrm{d}}), \sin(\phi_i^{\mathrm{d}})\cos(\theta_i^{\mathrm{d}}), \sin(\theta_i^{\mathrm{d}})]^\mathsf{T}$ and $\hat{\mathbf{r}}_i = [\cos(\phi_i^{r})\cos(\theta_i^{\mathrm{r}}), \sin(\phi_i^{\mathrm{r}})\cos(\theta_i^{\mathrm{r}}), \sin(\theta_i^{\mathrm{r}})]^\mathsf{T}$, and where superscript d and r represent direct arrival and surface reflection, can be judiciously formed based on the physical properties of surface reflection of a calm water surface. The pairs must satisfy

1. $|\phi_i^{\mathrm{d}} - \phi_i^{\mathrm{r}}| \leq \varepsilon$
2. $\theta_i^{\mathrm{r}} > |\theta_i^{\mathrm{d}}|$
3. $0 \leq \delta_i \leq 2h_{\mathrm{u}}$

for $i = 1, 2, \cdots, P'$ where h_{u} is the maximum water depth. The first property indicates that the azimuth angle of the reflection has to be within a small deviation from the direct arrival of the snap. The second property requires the unit vector of the reflection to be above the direct arrival. Lastly, the difference in path length is a positive real value, bounded by property 3. The problem size has been extensively reduced to N arrivals and P' pairs where $P' \ll N^2$.

5.2.2 Joint association and estimation

Let the N arrivals be the vertices, and the P' pairs of the arrivals be edges of a Graph. We define a weighted Graph with incidence matrix $\mathbf{G}$. The weight of the edge i, denoted by w_i, indicates the likeliness of the associated direct and surface-reflected pair i. Unlike the standard approach, the acoustic signature of the arrival of the snaps is not very useful in identifying the pairs. We suggest that the weights be defined by the fitness of the pairs with respect to the geometric model. Any pair which conforms to the geometrical constraints will have a large weight and vice versa. However, the geometric model contains unknown parameters and we can only define the weight as a function of the parameters such as the nominal water depth and receiver orientation. $\mathbf{G}$ is a N by P binary matrix with the "1" elements representing pairing on the vertices which means each column of $\mathbf{G}$ contains two "1" elements.

The challenge of this problem is that the pairing depends on the unknown parameters but the parameter estimation requires a good set of pairs. To localize the snaps, we have to jointly associate the pairs and estimate the unknown parameter in order to find the set of pairs that maximizes the sum of the weights of edges of the Graph. Formally, this can be written as

$$
\begin{aligned}
&\arg \max_{\substack{\mathbf{x}\in\{0,1\}^{P'},\\ h',\hat{\mathbf{s}}':\|\hat{\mathbf{s}}'\|_2=1}} \mathbf{w}^{\mathsf{T}}\mathbf{x} - \mu f(\mathbf{x}, h', \hat{\mathbf{s}}') \\
&\text{s.t. } \mathbf{G}\mathbf{x} \leq \mathbf{1}, \\
&\qquad w_i = \begin{cases} \frac{1}{\|\hat{\mathbf{s}}'+\hat{\mathbf{n}}_i(h',\hat{\mathbf{s}}')\|_2^2} & (\hat{\mathbf{n}}_i(h',\hat{\mathbf{s}}'))_z \leq \kappa, \\ 0, & \text{otherwise} \end{cases} \\
&\qquad \text{for } i = 1, 2, \cdots, P'
\end{aligned} \tag{5.4}
$$

where $\mathbf{x}$ is a P'-dimensional binary column vector with "1" elements indicating the existence of the pairs, $\hat{\mathbf{n}}_i(h', \hat{\mathbf{s}}') = \mathbb{U}(\mathbb{U}(D_i'(h', \hat{\mathbf{s}}')\hat{\mathbf{d}}_i - \frac{h'}{\hat{\mathbf{r}}_i^{\mathsf{T}}\hat{\mathbf{s}}'}\hat{\mathbf{r}}) - \hat{\mathbf{r}}_i)$ for $D_i'(h', \hat{\mathbf{s}}')$ as given in (4.7) parameterized by h' and $\hat{\mathbf{s}}'$. $f(\mathbf{x}, h', \hat{\mathbf{s}}')$ is the objective function of (5.1) with respect to variables $\mathbf{x}$, h' and $\hat{\mathbf{s}}'$. $\mu > 0$ indicates the importance between arrival association and parameter estimation. The first constraint (inequality) of the optimization problem is that every arrival can only be associated once. The second constraint defines the weight as a function of the parameters. Let $(\hat{\mathbf{n}}_i(h', \hat{\mathbf{s}}'))_z$ be the z-axis element of the normal vector $\hat{\mathbf{n}}_i(h', \hat{\mathbf{s}}')$. κ is a real value greater and close to -1. The hard threshold $(\hat{\mathbf{n}}_i(h', \hat{\mathbf{s}}'))_z \leq \kappa$ constrains the normal vector of the local water surface to point approximately downwards, representing a calm sea state. The optimization problem is complicated and there is no obvious algorithm to solve it optimally. We next propose an algorithm to solve this problem approximately.

5.2.3 Alternating association and estimation

Instead of solving the joint association and estimation problem, the location of the snaps can be estimated by alternatingly associating the pairs with fixed parameters and then estimating the parameters with fixed selected pairs. Given the prior knowledge of the parameters, we can compute the weights of the edges and select a set of pairs that maximizes the sum of the weights (**Association**). Next, based on the pairing, we can improve the prior knowledge of the parameters for the range estimator (**Estimation**). The **Association** and **Estimation** are repeated in an alternating manner until some criteria are fulfilled. We summarize the method in algorithm 5.1. A major limitation of the proposed algorithm is lack of convergence proof as the **Association** does not guarantee the reduction of the objective function in **Estimation** compared to the previous iteration's. In fact, we will show that given a good initialization of h and $\hat{\mathbf{s}}$, the algorithm stops at a few iterations in the numerical simulations as well as the experimental results.

After the computation of the algorithm, we can further refine the remaining pairs by deciding on a threshold with respect to the amplitudes of $\mathbf{w}$ to separate the pairs into two clusters. Correct pairings fall into the high amplitude cluster, while nuisance pairings fall into the low amplitude cluster. Since the association and estimation algorithm selects the distinct set of pairs that maximize the weights of the edges of the pairs, this algorithm is not able to deal with those pairs having very small weights which are probably nuisance pairs as long as they are not overlapping with other arrivals. The existence of the small number of

Algorithm 5.1 Alternating association and estimation for snap localization

Require: $\{(\hat{\mathbf{d}}_i, \hat{\mathbf{r}}_i, \delta_i)\}_{i=1}^{P'}$, $\mathbf{G}$,
$\mathbf{x}^{(0)} \leftarrow \mathbf{0}$,
$h'^{(0)} \leftarrow$ average water depth,
$\hat{\mathbf{s}}'^{(0)} \leftarrow [0,0,1]^{\mathsf{T}}$,
$k \leftarrow 0$,
maxIter $\leftarrow$ maximum number of iterations,
$\epsilon_h \leftarrow$ positive small value,
$\epsilon_{\hat{\mathbf{s}}} \leftarrow$ positive small value

1: Given $w_i = \begin{cases} \frac{1}{\|\hat{\mathbf{s}}'^{(k)} + \hat{\mathbf{n}}_i(h'^{(k)}, \hat{\mathbf{s}}'^{(k)})\|_2^2} & (\hat{\mathbf{n}}_i(h'^{(k)}, \hat{\mathbf{s}}'^{(k)}))_z \leq \kappa, \\ 0, & \text{otherwise} \end{cases}$ for $i = 1, 2, \cdots, P'$, solve

$$\arg \max_{\mathbf{x} \in \{0,1\}^{P'}} \mathbf{w}^{\mathsf{T}} \mathbf{x} \quad \text{s.t. } \mathbf{G}\mathbf{x} \leq \mathbf{1}$$

for $\mathbf{x}^{(k+1)}$.
2: Given $\mathbf{x}$, we solve (5.1) for $\tilde{h}^{(k+1)}$ and $\tilde{\hat{\mathbf{s}}}^{(k+1)}$.
3: **if** $k \leq$ maxIter OR $(\|h'^{(k)} - h'^{(k+1)}\|_2 > \epsilon_h$ AND $\|\hat{\mathbf{s}}'^{(k)} - \hat{\mathbf{s}}'^{(k+1)}\|_2 > \epsilon_{\hat{\mathbf{s}}}$ AND $\|\mathbf{x}^{(k)} - \mathbf{x}^{(k+1)}\|_2 > 0)$ **then**
4: $k \leftarrow k+1$
5: Go to 2
6: **end if**
7: **return** $\mathbf{x}$, $\tilde{h} \leftarrow h'^{(k)}$, $\tilde{\hat{\mathbf{s}}} \leftarrow \hat{\mathbf{s}}'^{(k)}$

nuisance pairs does not effect the performance of parameter estimation. Hence, the refinement process is crucial to remove the nuisance pairs at this final stage.

5.2.4 Numerical simulations

Referring to the same data generated in simulation 1 and 2 in the previous section, we do not assume perfect association of the direct and surface-reflected snap. In fact, 100 direct arrivals and 100 reflections were independently discarded to create a 10 percent nuisance arrival noise and hence the maximum number of correct pairs is 1800. We used $\lambda = 8000$ to compute the parameter estimation for simulation 1 and simulation 2. The estimated location of the snaps λ' based on these parameters are shown in Figure 5.4. We only depict the location of snaps at x- and y-axes in simulation 1 for the ease of visualization. We present the estimated receiver orientation $\hat{\mathbf{s}}'$ in the form of pitch $\alpha^{(o)\prime}$ and roll $\rho^{(o)\prime}$ for the ease of comparison with the actual simulated receiver orientation in $\alpha^{(o)}$ and $\rho^{(o)}$. The proposed method is able to recover most of the direct and surface-reflected snaps in both cases. As the snaps are farther apart from the receiver, the accuracy of the estimated parameters is slightly degraded.

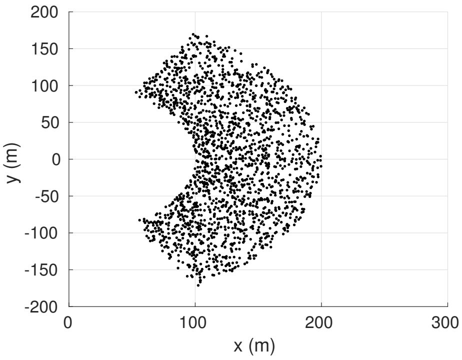

(a) Actual location of snaps at x- and y-axes in simulation 1.

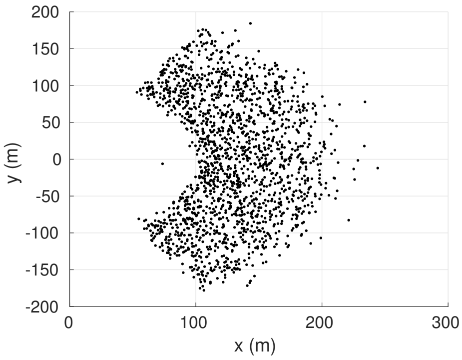

(b) Estimated location of snaps at x- and y-axes in simulation 1. $h' = 15.1689$ m, $\rho^{o\prime} = -4.9510°$, $\alpha^{o\prime} = -6.9403^{o\prime}$ and number of correct pairs is 1795.

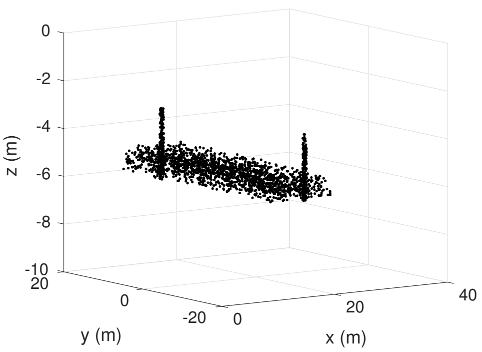

(c) Actual location of snaps in simulation 2.

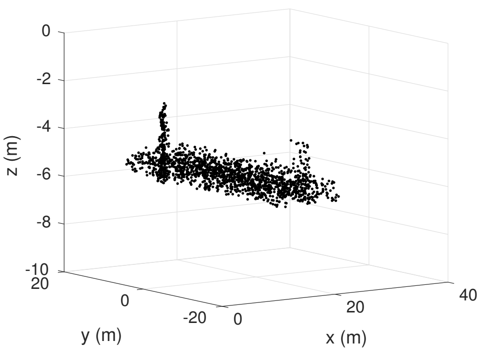

(d) Estimated location of snaps in simulation 2. $h' = 5.1205$ m, $\rho^{o\prime} = -4.9840°$, $\alpha^{o\prime} = 7.0444^{o\prime}$ and number of correct pairs is 1787.

Figure 5.4: Location of the snaps based on alternating association and estimation. The actual location of the snaps is presented for reference.

5.3 Summary

In this section, we presented a two-step optimization method to estimate the nominal water depth and the receiver orientation. We verified the performance of the method in two simulation results. Subsequently, we discussed a more practical problem which includes the association of the direct arrival and surface-reflected snaps along with the parameter estimation. We propose an algorithm to solve this problem suboptimally.

Chapter 6

Experiments

In the previous chapters, we reviewed the limitations of existing methods in detecting DoA-ToA of snaps and suggested reliable DoA-ToA detection methods based on assumption of sparse DoA-ToA. Given the detected DoA-ToA of snaps, we discussed the challenges in estimating the originating locations of the snaps. We have showed through numerical simulations that our proposed methods are capable of solving the snap detection and localization problems. In this chapter, we first provide a suggestion on refining the estimated range of a snap by considering the estimated range of adjacent snaps in experimental results. We describe the details of the experiments, and then present the results based on the experimental data collected in Singapore waters in 2010 and 2014.

6.1 Spatial smoothing of estimated locations of snaps

For convenience, the range estimator is developed based on the assumption of unperturbed water depth, where $\eta_i = 0$ for any i. In reality, perturbation in water depth exists and η_i is non-zero, which contributes to the estimation error. The first order approximation of the range estimation error can be written as

$$D_i - D_i' \approx \frac{\delta_i^2 + \delta_i^2 \hat{\mathbf{d}}_i^\mathsf{T} \hat{\mathbf{r}}_i}{2\left(\delta_i - \frac{h}{\hat{\mathbf{r}}_i^\mathsf{T}\hat{\mathbf{s}}} + \frac{h}{\hat{\mathbf{r}}_i^\mathsf{T}\hat{\mathbf{s}}}\hat{\mathbf{d}}_i^\mathsf{T}\hat{\mathbf{r}}_i\right)^2 \hat{\mathbf{r}}_i^\mathsf{T}\hat{\mathbf{s}}} \eta_i. \tag{6.1}$$

Let $\{\eta_i\}_{i=1}^{P'}$ be IID symmetric unimodel random variables. We can improve the estimated range by calculating the mean of an ensemble of signals from the same snap source. However, it is very difficult to distinguish which are the signals originating from the same snap source. One alternative in obtaining the estimated range is to calculate the mean of estimated ranges of multiple adjacent snap sources having approximately the same DoA. The reasoning behind this method is the fact that we usually observe snapping shrimp living close together in colonies whether on coral reefs or man-made structures. So the direct snap arrivals from the same DoA over time are most likely to have originated from the same shrimp colony, and not from different colonies at different distances away. Note also that these shrimp colonies reside on solid structures which form a barrier for direct arrival propagations from other shrimp sources farther away. Let $\mathcal{B}$ be the discrete set of all possible DoA. Then, we define $\mathcal{B}'_{(\phi_i,\theta_i)} = \{(\phi,\theta) || \phi - \phi_i| \leq \epsilon_\phi, |\theta - \theta_i| \leq \epsilon_\theta, (\phi,\theta) \in \mathcal{B}\}$ where ϵ_ϕ and ϵ_θ are some small angles. We can now refine the estimated range of the snap i as

$$D''_i = \frac{1}{|\mathcal{B}'_{(\phi_i,\theta_i)}|} \sum_{j:(\phi_j,\theta_j)\in\mathcal{B}'_{(\phi_i,\theta_i)}} D'_j. \tag{6.2}$$

6.2 Experiment 2010

Experiment 2010 was conducted within a stretch of sea covering 500 m$\times$500 m at Selat Pauh anchorage in Singapore waters during the months of April-May 2010. ROMANIS was deployed from a barge at the location 1°12.967′**N**, 103°44.382′**E** with average water depth of 15 m. It was stationed on the seabed with a reasonably flat bathymetry where the sea bottom was a mix of sand and mud. The sea state within the deployment area was reported to be calm. The array was positioned to face southward such that two long-term mooring buoys fall in the field of view of the array. Buoy 1 and buoy 2 were at the range of about 144 m and 246 m respectively from ROMANIS. These buoys provide interesting points for study because the anchor lines of the buoys present suitable habitats for the snapping shrimp to form colonies that are structurally different from those lodging on the seabed. Figure 6.1 shows photographs taken during the experiment and Figure 6.2 is a map indicating the location of the experiment. Acoustic pressure data dominated by snapping shrimp noise were recorded. In particular, two 30-second datasets collected on April 11, 2010 at 21:04:55 and 21:05:42 local time respectively were used. We present the experimental results regarding snapping shrimp noise DoA-ToA detection and localization in the following section.

(a) Deploying ROMANIS. (b) Long-term mooring buoy 1.

Figure 6.1: Photographs taken from the barge during Experiment 2010.

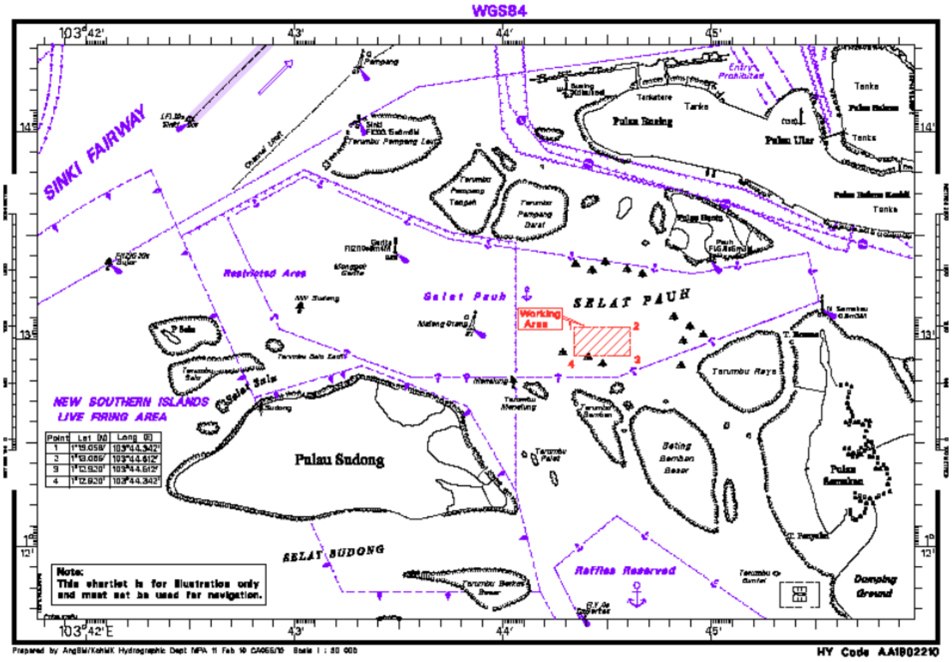

Figure 6.2: Selet Pauh location chart. The red box is the working area of the experiment.

6.2.1 DoA-ToA detection

For DoA-ToA detection, a 10-second data segment collected on April 11, 2010 at 21:05:42 was used. We define the set of azimuth angles $\mathcal{S}_\phi = \{-50°, -49.5°, \cdots, 50°\}$, the set of elevation angles $\mathcal{S}_\theta = \{-30°, -29.5°, \cdots, 40°\}$ and the set of time of arrivals $\mathcal{S}_\Gamma = \{0, 1, \cdots, 3920\}$ for $\mathcal{S}$. We set the threshold u to 1^{st} percentile of the sensor data for arrival detection. The maximum time lag of XCorr is 0.844 ms for the full-sized ROMANIS, and 0.390 ms for the scaled-down ROMANIS with diameter 0.6 m. Array response $\mathbf{A}$ was generated by randomly selecting 512 frequency points while the reduced-size $\mathbf{A}$ was based on 90^{th} percentile of the energy of the DAS beamformed output. The choice of 512 frequency points is based on the practice of downsampling the total Fourier coefficients by a multiple integer factor. We computed $\mathbf{z}^{\mathrm{XCorr}}$, $\mathbf{z}^{\mathrm{Hough}}$, $\mathbf{z}^{\mathrm{DAS}}$, $\mathbf{z}^{\mathrm{BS}}$, and $\mathbf{z}^{\mathrm{rS}}$ accordingly. For DoA-ToA detection, we set the threshold distance $\triangle_{\phi} = 1°$, $\triangle_{\theta} = 1°$, and $\triangle_{\Gamma} = 0.510$ ms while the threshold amplitude $\triangle_{\mathbf{z}}$ is defined by the 0.999^{th} percentile of $\mathbf{z}$. The DoA-ToA detection is repeatedly computed over the 10-second data segment without overlapping.

Let N_a be the number of detected DoA-ToAs and $\triangle N_a$ be normalized value of the change in the number of detected DoA-ToAs with respect to the full-sized ROMANIS. We verify the detection performance by plotting the detected DoA in Figure 6.3 and showing the changes in the number of detected DoA-ToA between full-sized and scaled-down ROMANIS in Table 6.1. The table shows that given the same dataset, the detection performance is verified through ΔN_a with different aperture sizes and different number of sensors in the receiver. This measurement provides an indication on the consistency and robustness of the detection method with respect to changes in array resolution (smaller aperture) and changes in array signal-and-noise ratio (lesser number of sensors). Hough generally has the worst performance in terms of the ability to compute the DoA of snapping shrimp noise as shown in Figure 6.3. This may due to the large number of false positive detection. The DoA plot of XCorr using full-sized ROMANIS differs from the one using scaled-down ROMANIS. Compared with full-sized ROMANIS, DoA-ToA detection of XCorr using scaled-down ROMANIS tends to be inconsistent as shown in Table 6.1 and its DoA plot does not give a clear illustration on the colonies of shrimp. DoA plots of BS and DAS seem to have consistent detection performance regardless of the ROMANIS size according to Figure 6.3. However, we observe that the change in the number of detected DoA-ToAs of the methods is huge from using full-sized to scaled-down ROMANIS. This shows that the methods may be sensitive to aperture size as well as the PSNR of sensor data. Note that BS has the largest number of detected DoA-ToA but with considerably lesser coverage in DoA. One particular DoA might contain multiple detections in the ToA-axis as the BS method only enforces sparsity in DoA space.

The DoA plot using rS mainly consists of three layers: the middle layer, which corresponds to shrimp colonies residing on the seabed, and the top and bottom layers which may be due to surface and bottom reflections of the snapping shrimp noise. There is significant amount of arrivals propagating at 2.4° azimuth angle which probably originated from snapping shrimp colonies on buoy 1. The proposed method tends to discover more arrivals from buoy 2 at roughly 37° azimuth angle. According to the Global Positioning System (GPS) coordinates data, the azimuth angle between the straight line from ROMANIS to buoy 1 and the straight line from ROMANIS to buoy 2 is approximately 36°. This shows that the detected DoA is close to the calculated azimuth angles of the buoys.

TABLE 6.1: Number of detected DoA-ToAs in Experiment 2010.

Method	ROMANIS	N_a	$\triangle N_a$
XCorr	full-sized	2070	31%
	scaled-down	2709	
Hough	full-sized	8590	93%
	scaled-down	16555	
DAS	full-sized	3453	56%
	scaled-down	1514	
BS	full-sized	17352	35%
	scaled-down	11326	
rS	full-sized	3925	7%
	scaled-down	3656	

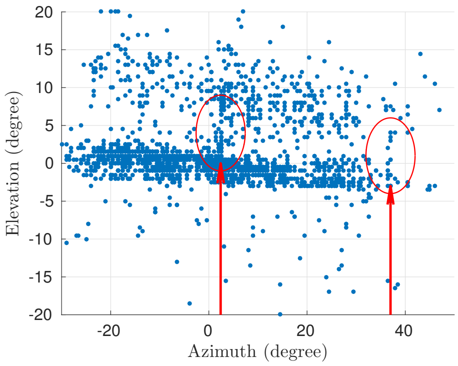

(a) DoA using XCorr (full-sized)

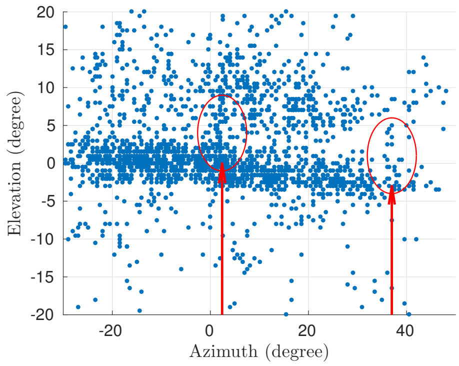

(b) DoA using XCorr (scaled-down)

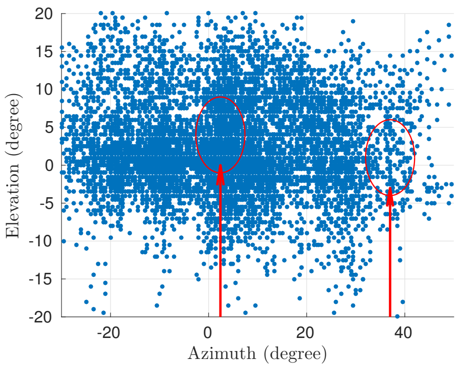

(c) DoA using Hough (full-sized)

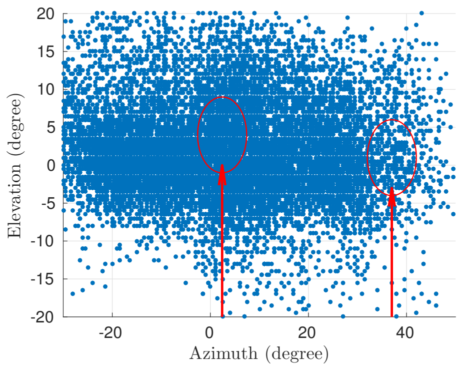

(d) DoA using Hough (scaled-down)

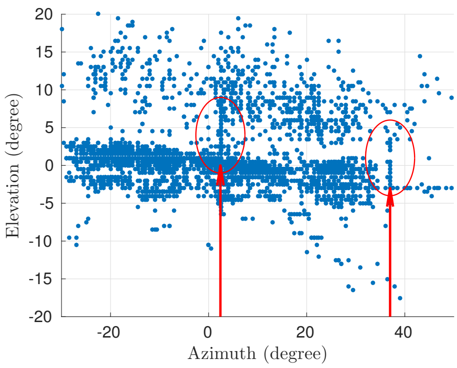

(e) DoA using DAS (full-sized)

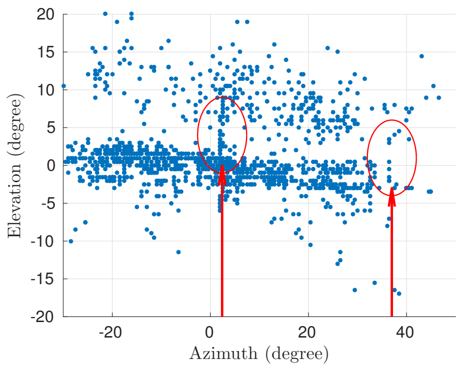

(f) DoA using DAS (scaled-down)

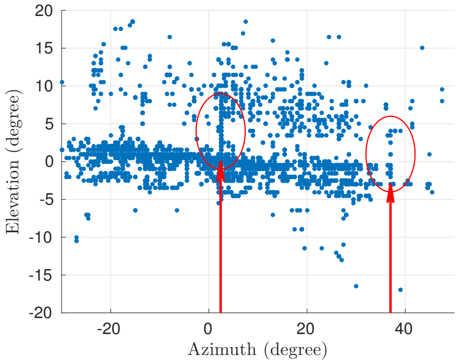

(g) DoA using BS (full-sized)

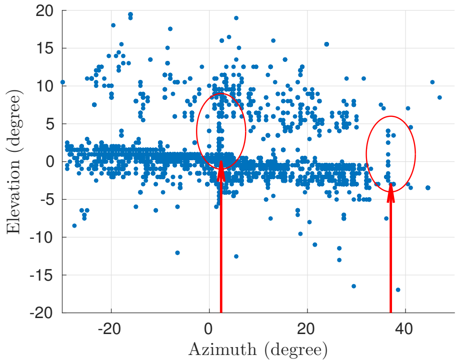

(h) DoA using BS (scaled-down)

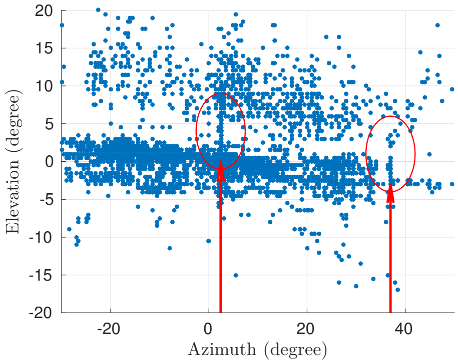

(i) DoA using rS (full-sized)

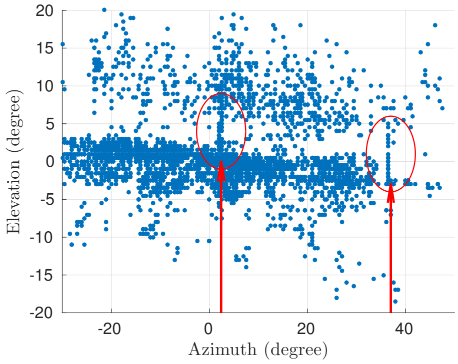

(j) DoA using rS (scaled-down)

Figure 6.3: The blue points in the scatter plots are the detected DoA. Buoy 1 and 2 are marked by the red circles, while the arrows indicate the azimuth angle of the buoys.

6.2.2 Snap localization

Based on the entire dataset collected at 21:05:42 local time using full-sized ROMANIS, DoA-ToA detection using rS were performed and 11482 arrivals were detected. We set $\varepsilon_\phi = 20^\circ$ and $h_u = 20$ m for the coarse pairing and $\lambda = 10000$ for the parameter estimation. All the snaps propagating within $\epsilon_\phi = 1^\circ$ and $\epsilon_\theta = 1^\circ$ were considered to have from the same shrimp colony. Two results, one showing purely the estimated location of snaps and the other showing the spatially smoothed estimated location of snaps, were presented.

Given a location of a snap, spatial smoothing computes a new location of the snap through averaging the location of adjacent snaps with similar DoA. Since this procedure applies to every snaps, the number of estimated locations of snaps remains the same for both plots.

Without spatial smoothing, Figure 6.4(a) shows that the estimated ranges of snaps originating from the buoys suffer from deviations of approximately 10 m possibly caused by vertical wave motion. Figure 6.8(b) shows the spatially smoothed estimated location of snaps such that two clusters of snaps form vertical patterns while the remaining snaps populate an inclined surface. The vertical patterns are located 140.13 m and 251.92 m respectively from ROMANIS. The ranges of these vertical columns match the actual ranges of the buoys. This suggests that the vectical patterns of snaps are probably originated from the snapping shrimp lodged on the long-term mooring buoy. The cluster of snaps over the inclined surface can be mapped to the colonies of shrimp populating the sloping seabed. The spatial distribution of this cluster gives an indication on the local bathymetry of the seafloor between buoys, showing a decreasing depth from buoy 1 at 14 m, to buoy 2 at 11 m. The visual inspection is slightly different from the reported nominal water depths of buoy 1 and buoy 2 which are 11.5 m and 10 m respectively according to 2010 hydrographic chart. The accuracy of the buoy depth is mainly limited by the number of snaps obtained from the area of interest.

For the same dataset, the estimated nominal depth is 16.06 m and the estimated receiver orientation is $\rho' = 1.6°$ and $\alpha' = 2.0°$. To verify the accuracy of the estimation, we performed the DoA-ToA detection based on another

30-second dataset collected at 21:04:55 local time. The spatial distribution of the estimated location of snaps is generally similar to the previous result with a slightly different estimated parameters. From the second dataset, we obtained 15.51 m for the estimated nominal water depth, and $\rho' = 1.7°$ and $\alpha' = 1.8°$ for the estimated receiver orientation. The experimental results provided here are adequate in the feasibility study of using small aperture receiver for localizing snapping shrimp. However, the size and the number of datasets in this experiment might not be sufficient to reveal most of the shrimp colonies. We address these issues and further verify the localization performance by conducting another experiment as discussed in the following section.

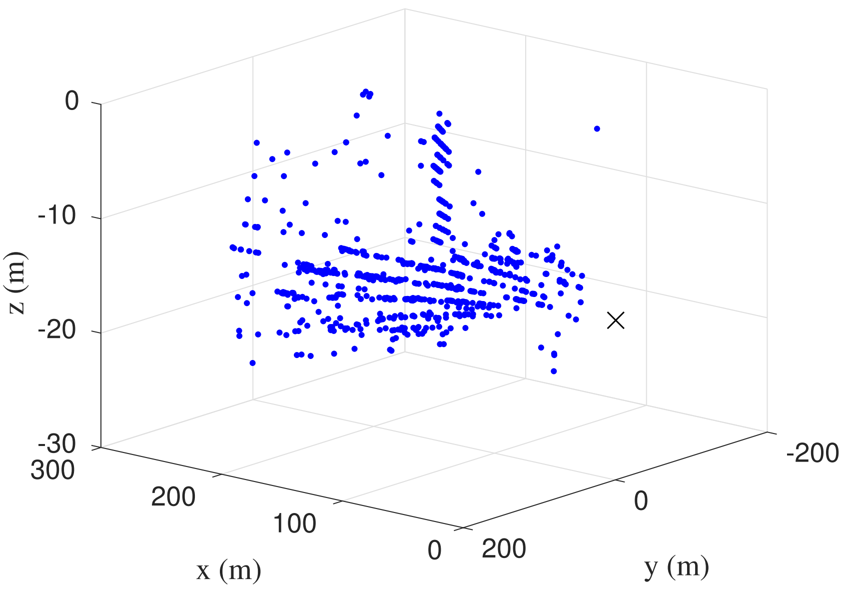

(a) Dots show the estimated locations of snaps without spatial smoothing. The origin of ROMANIS is denoted by the black cross.

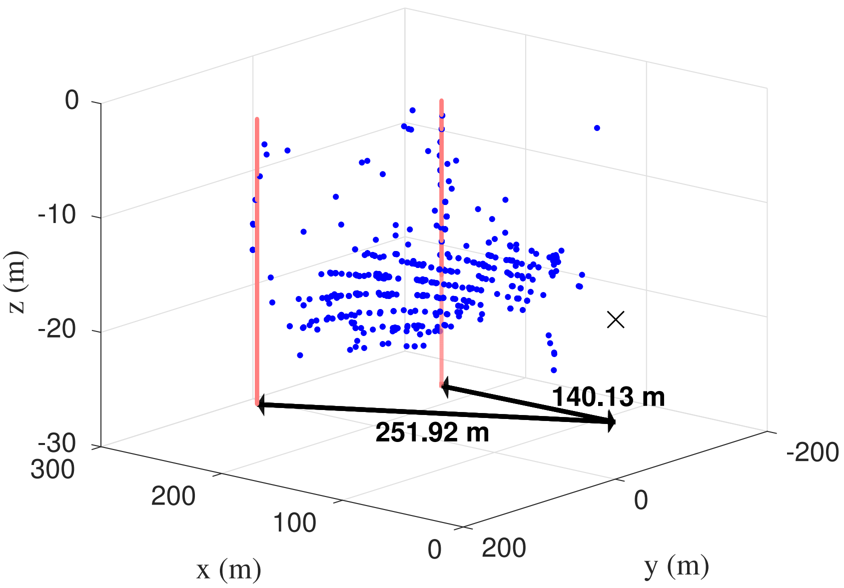

(b) Dots show the estimated locations of snaps with spatial smoothing and red vertical lines illustrate the x-y position of the buoy. The origin of ROMANIS is denoted by the black cross.

Figure 6.4: Estimated location of snaps in Experiment 2010.

6.3 Experiment 2014

Experiment 2014 was conducted at St. John Island, Singapore in August 2014. ROMANIS was deployed at $1°13.027'\mathbf{N}, 103°51.106'\mathbf{E}$ with average water depth of 5 m to collect the acoustic pressure recording of ambient noise which is dominated by snapping shrimp noise. It was surrounded by man-made structures like the jetty, watergate and fishing farm. A large amount of snaps can be observed in these areas as they form a conducive environment for snapping shrimp. ROMANIS was positioned approximately 8 m away facing the jetty where a lot of snaps can be found. Figure 6.5 shows the photographs of the experiment and a labeled Google Map indicating the position of the surrounding man-made structures. Four datasets containing snapping shrimp noise from the jetty were recorded at different time slots. Each of the dataset is a 300-second acoustic pressure recording by ROMANIS. The sea state during the recording was reported to be calm.

6.3.1 DoA-ToA detection

One of the datasets was collected on August 12, 2014 at 15:49:43 local time. A 10-second data segment was used to verify the performance of DoA-ToA detection of snapping shrimp noise. The computations of $\mathbf{z}^{\mathrm{XCorr}}$, $\mathbf{z}^{\mathrm{Hough}}$, $\mathbf{z}^{\mathrm{DAS}}$, $\mathbf{z}^{\mathrm{BS}}$, and $\mathbf{z}^{\mathrm{rS}}$ are generally the same as the previous experiment's. Note that the receiver was placed near the jetty and close to the coast, and hence reflected snaps on underwater structure of the jetty as well as seafloor are significant. An incident of snap might cause a large number diffuse reflections on the rough surface of these obstacles. For better visualization of snapping shrimp position,

(a) Deploying ROMANIS at the jetty.

(b) Jetty

(c) Position of ROMANIS in the labeled Google map.

Figure 6.5: Experiment 2014 at St. John Island, Singapore.

either in the DoA space or the later 3-dimensional Euclidean space, the detected DoA-ToA is post-processed by setting maximum number of detections to 20 for each round of DoA-ToA computation over the dataset to reduce the number of such arrivals.

We examined the detection performance by plotting the detected DoA in Figure 6.6 and showing the changes in the number of detected DoA-ToA between full-sized and scaled-down ROMANIS in Table 6.2. The DoA plots for all the methods using full-sized ROMANIS are essentially the same, except for the BS method's. A visual inspection of the DoA plots show that the estimated location of snaps in DoA space can be classified into two clusters, a bottom layer and a top layer. These two layers merge into one at the receiver's broadside while separate out beyond the receiver's broadside. The bottom layer is probably due to the direct arrivals of the impulsive transient signals originating from snapping shrimp lodging on the pillars of the jetty. The top layer is simply the mirror image of the bottom layer caused by surface-reflected snaps. This is obvious especially in the detected DoA-ToA using DAS and rS. When the size of ROMANIS was reduced, the changes in the number of DoA-ToA detections using XCorr, Hough, DAS, and BS based on the same threshold values are huge. The possible reasons for the difference are the low PSNR and the lack of ability to resolve arrivals close in DoA-ToA space using small aperture receiver. In contrast, the change in the number of detections between full-sized and scaled-down ROMANIS using rS is relatively small. This observation is indeed consistent with the result in Experiment 2010.

Table 6.2: Number of detected DoA-ToAs in Experiment 2014.

Method	ROMANIS	N_a	$\triangle N_a$
XCorr	full-sized	1675	43%
	scaled-down	2401	
Hough	full-sized	2934	51%
	scaled-down	1437	
DAS	full-sized	2408	55%
	scaled-down	1079	
BS	full-sized	676	202%
	scaled-down	2042	
rS	full-sized	2510	15%
	scaled-down	2130	

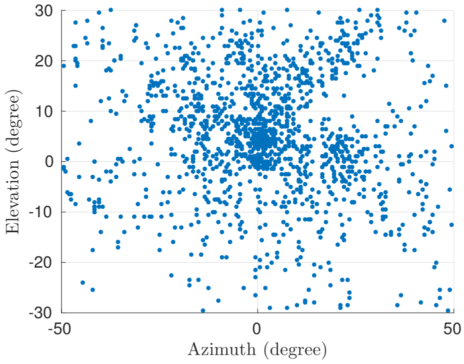

(a) DoA using XCorr (full-sized)

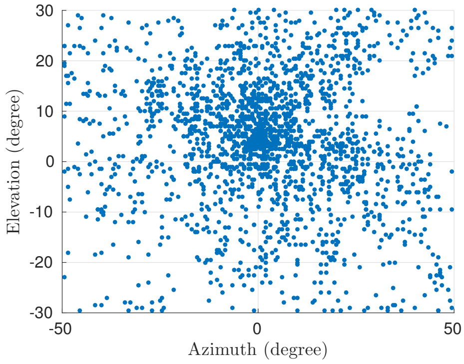

(b) DoA using XCorr (scaled-down)

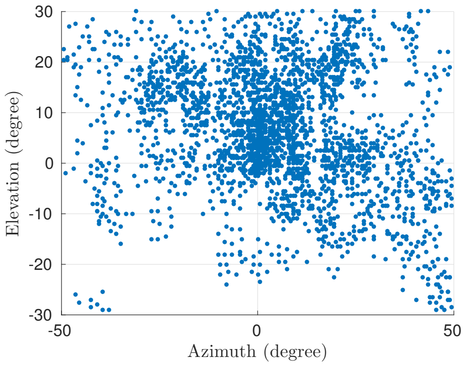

(c) DoA using Hough (full-sized)

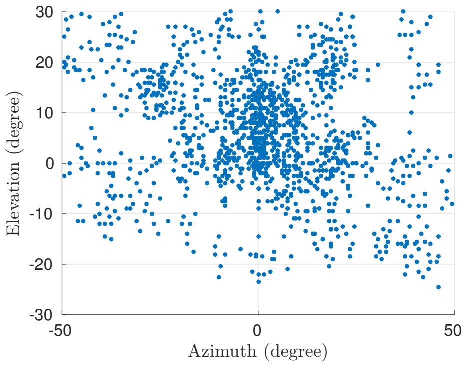

(d) DoA using Hough (scaled-down)

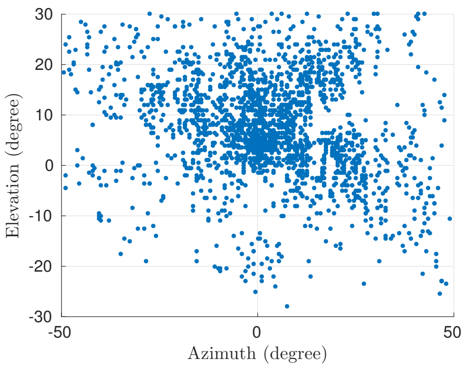

(e) DoA using DAS (full-sized)

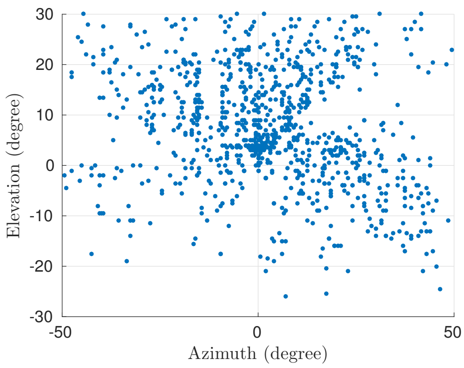

(f) DoA using DAS (scaled-down)

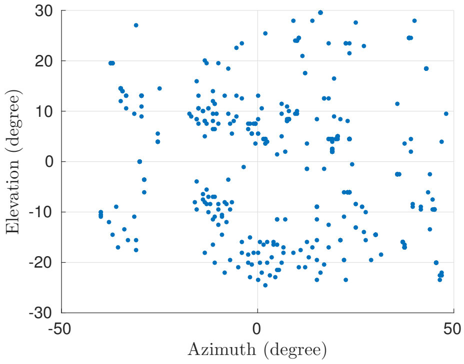

(g) DoA using BS (full-sized)

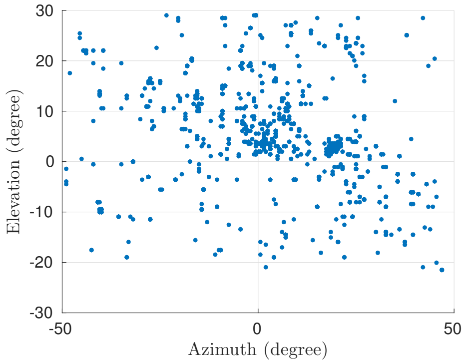

(h) DoA using BS (scaled-down)

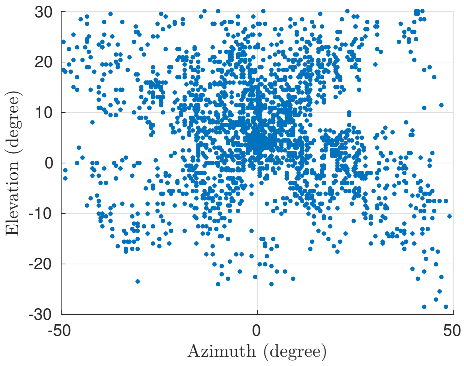

(i) DoA using rS (full-sized)

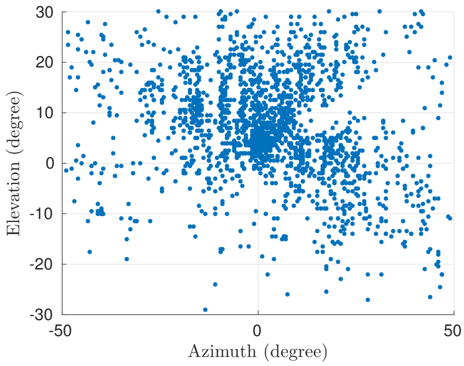

(j) DoA using rS (scaled-down)

Figure 6.6: The blue dots in the scatter plots are the detected DoA.

6.3.2 Snap localization

From the same dataset, 34531 arrivals, which comprise direct arrivals and multipath reflections of snapping shrimp noise, were detected using full-sized ROMANIS, and subsequently the location of these snaps were estimated. We set $\varepsilon_\phi = 20^\circ$ and $h_u = 20$ m for the coarse pairing and $\lambda = 5000$ for the parameter estimation. We presented two results regarding the estimated location of snaps. The first is purely the estimated location of snaps while the second is the spatially smoothed estimated location of snaps.

Figure 6.8 displays the layout of the jetty along with the estimation results of the shrimp locations for comparison. Based on $\epsilon_\phi = 1^\circ$ and $\epsilon_\theta = 1^\circ$, the estimated snap locations with spatial smoothing reveals some of the pillars of the jetty. In Figure 6.8(a), it can be seen that without spatial smoothing, the pillars of the jetty are not so clearly revealed, because there is a bigger spread of estimated range of snaps from the same colony, possibly due to vertical wave motion. Comparing the layout of the jetty in Figure 6.7 and the estimated locations of snaps in Figure 6.8(b), we notice that the vertical patterns formed by the estimated snap locations match the pillars of the jetty. In particular, the actual distance between pillar A and B is $4-8$ m while the observed distance is around 5.87 m. The actual distance between pillar A and C should be at least 4 m since the pillars are not truly vertical but are inclined outwards such that the base of the pillars are more than 4 m apart. The observed distance between the two vertical patterns of the estimated shrimp locations, which corresponds to the pillars A and B, is 6.70 m. The estimated sources of snaps trace out a slope extending from the seabed to the shore, which is a reasonable result, based on the local bathymetry information.

The remaining datasets were collected at 16:06:46, 16:44:16 and 16:51:25 local time respectively. Combining with the aforementioned dataset, the estimated nominal depth and receiver orientation over four datasets collected in different time slots are shown in Figure 6.9. On August 12, 2014, a high tide was reported at 12:45 followed by a low tide at 18:25 with the tidal height dropping gradually in between. According to the Singapore Tide Table 2014, the tidal height on August 12, 2014 at Tanjong Pagar, the closest point to St. John Island, measured 1.5 m at 16:00:00 and 1.1 m at 17:00:00 [64]. The difference between these tidal heights is 0.4 m.. This agrees with our observation regarding the changes in the estimated nominal water depth. The rate of reduction of $\hat{h}$ is the highest between dataset 16:06:46 and 16:44:16 as they have the largest time difference. The rate is lower for datasets which are smaller in time difference. The estimated receiver orientation obtained using snapping shrimp noise is consistent over datasets. The receiver orientation is shown to be slightly tilted with respect to the sea level.

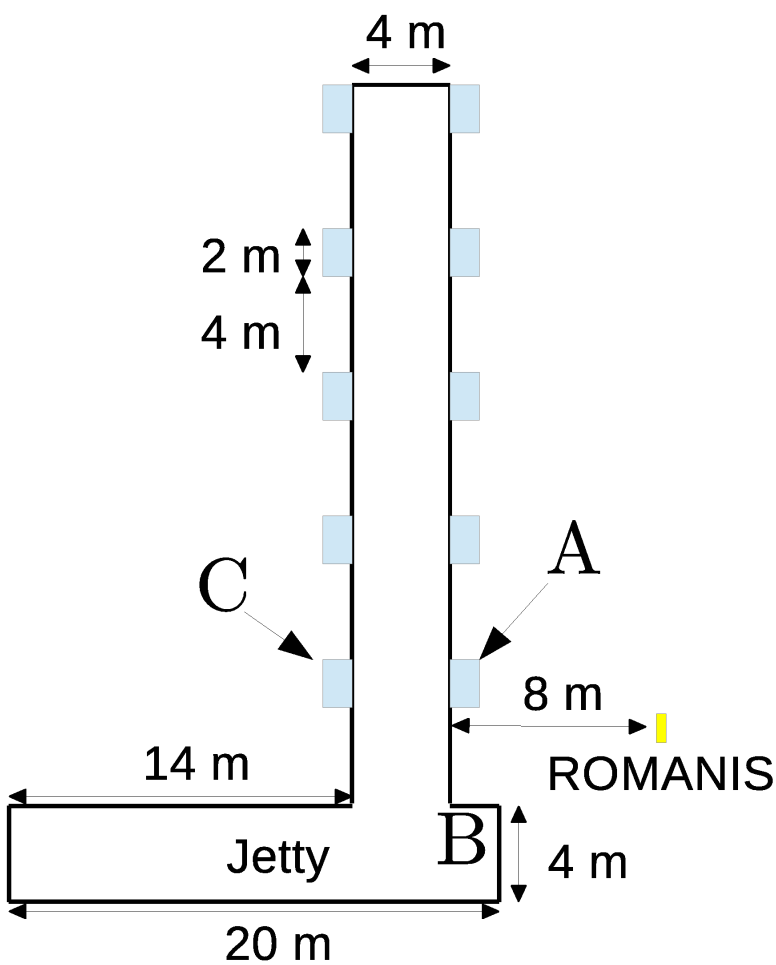

Figure 6.7: Layout of the jetty. A, B, and C indicate the pillars of the jetty.

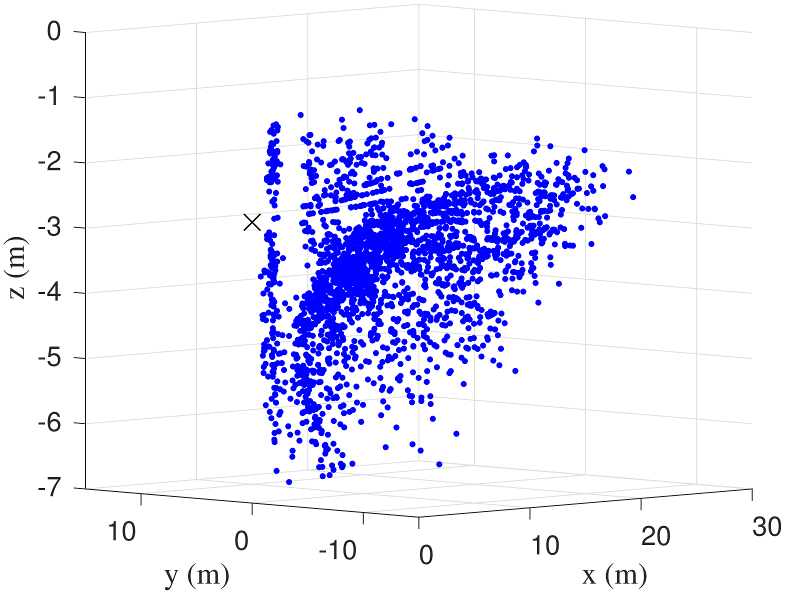

(a) Dots show the estimated locations of snaps without spatial smoothing. The position of ROMANIS is denoted by the black cross.

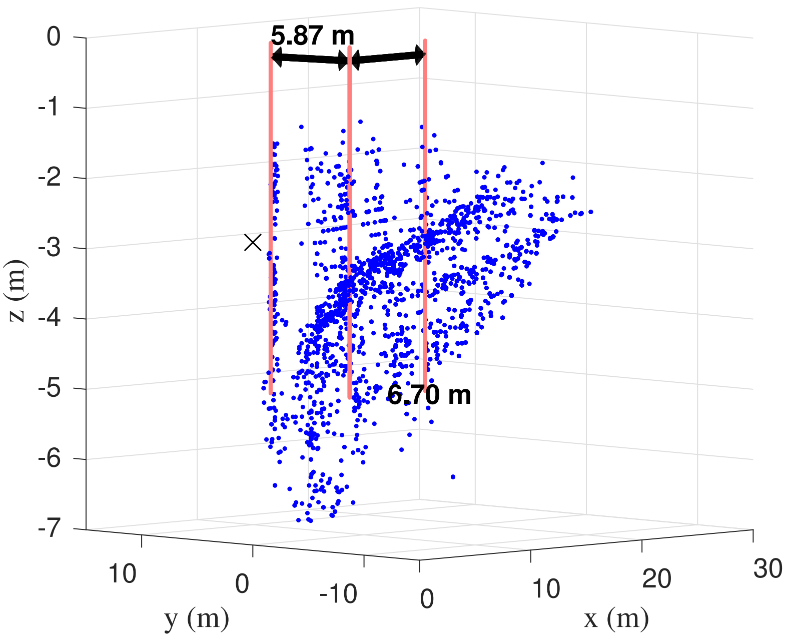

(b) Dots show the estimated locations of snaps with spatial smoothing and red vertical lines illustrate the x-y position of the pillars of the jetty. The position of ROMANIS is denoted by the black cross.

Figure 6.8: Estimated location of snaps originating from the jetty at St. John Island, Singapore.

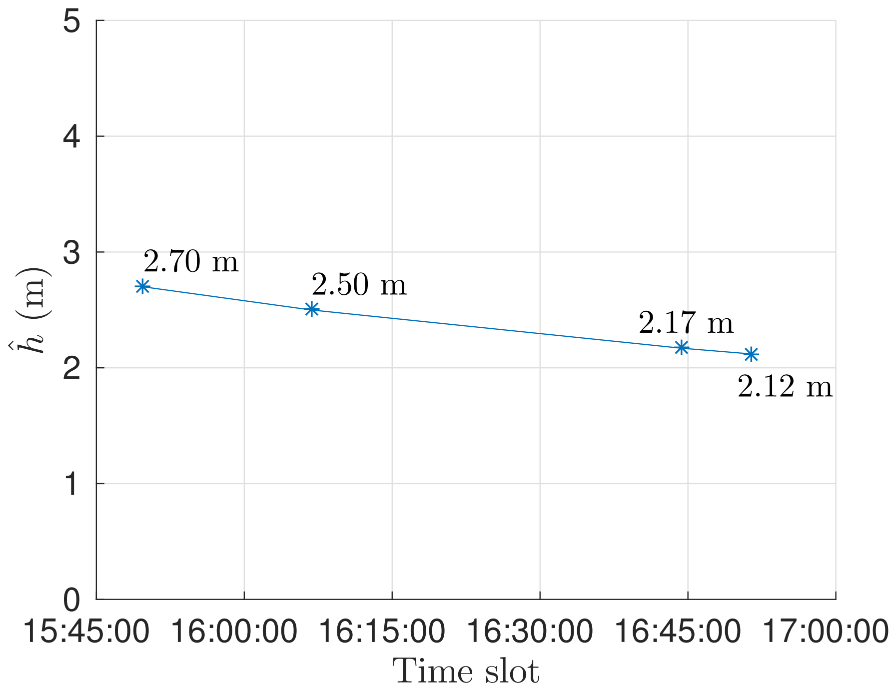

(a) Estimated nominal water depth $\hat{h}$.

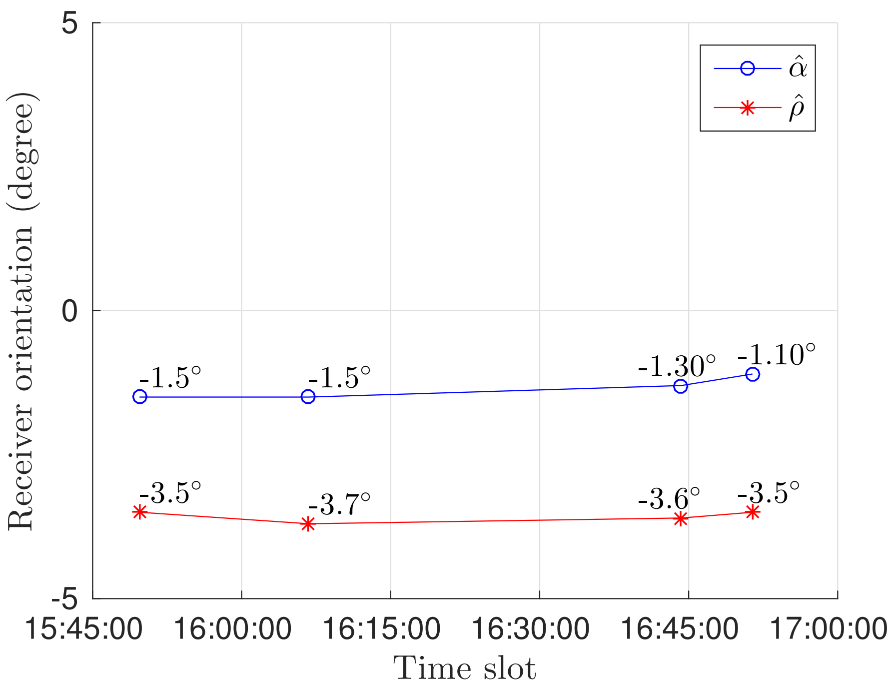

(b) Estimated receiver orientation defined by roll $\hat{\rho}$ and pitch $\hat{\alpha}$.

Figure 6.9: Estimated parameters based on different datasets.

6.4 Summary

In this chapter, we demonstrated that the proposed sparse DoA-ToA detection method is robust regardless of array size and threshold values. The method is able to identify impulsive signals originating from snapping shrimp lodging on the man-made structures in two distinct underwater environments. Subsequently, we showed that by incorporating the direct arrival and surface-reflected snaps, snap localization using small aperture receiver is feasible in practice. Field evidences, such as matching the estimated locations of the snaps with the local bathymetry as well as comparing the estimated parameters with the official hydrographic survey data, have been provided.

Chapter 7

Conclusion

7.1 Summary

The main aim of the thesis was to investigate the feasibility of passive sensing with snapping shrimp noise. Existing DoA-ToA detection methods are unable to resolve arrivals close in DoA-ToA, especially those using small aperture receivers. Our method, based on the assumption of sparse DoA is capable of high resolution DoA detection. We extended the idea by assuming the propagating snap to be sparse in both DoA and ToA, and developed reliable methods in detecting the DoA-ToA of snapping shrimp noise. The sparse DoA-ToA methods outperformed some of the common methods such as cross-correlation-based TDoA and other variants of the beamforming method based on ROC curve. Even with a reduced-size array response matrix, the reduced-sparse DoA-ToA method showed detection performance comparable to that of the sparse DoA-ToA method. Based on the results on the number of detected DoA-ToAs and scatter plots of the DoA estimates, (derived from acoustic recording of snapping shrimp noise in Singapore waters,) we showed that our sparse DoA-ToA methods performed consistently regardless of the aperture size of the receiver. The reduced-sparse DoA-ToA method was able to discover persistent arrivals originating from shrimp colonies populating the known underwater man-made structures like the anchor lines of the long-term mooring buoys, and the pillars of the jetty. In fact, the proposed method could be applied to DoA-ToA detection problems involving any impulsive signals due to its general formulation. Note that all the results regarding our methods were computed by randomly undersampling Fourier coefficients of the sensor array recording. This finding could be useful for the development of efficient sensing mechanism that specializes in detecting the DoA-ToA of impulsive transient signals.

The second part of the study is to estimate the locations of the shrimp given their detected DoA-ToAs. In general, small aperture receiver can only estimate the DoA but not the range of snaps in the far-field. But by assuming that the ocean surface acts like an acoustic mirror, reflecting all the snaps at the surface, we explored the possibility of estimating the range of the snaps by measuring the TDoA between the direct arrival and surface-reflected snaps. To simplify the problem we first assumed that the direct and surface-reflected arrivals are perfectly associated. Then we formulated a geometric model to derive the range estimator, which is parameterized by the nominal water depth and receiver orientation. The 3-dimensional geometric model dispenses the restriction of the 2-dimensional model which requires the water surface to be completely flat. Through the sensitivity analysis, we showed that the range estimation error is linearly proportional to the range of the snap multiplied by the parameter errors. Parameter error of receiver orientation tends to be more significant than parameter error of nominal water depth. The range estimation error increases significantly when contaminated by parameter error in receiver orientation compared to parameter error in nominal water depth, at higher snap ranges.

Understanding the significance of the parameter estimation error, the next step aimed to improve the approximations, making use of an ensemble of associated direct arrival and surface-reflected snaps. A two-step iterative method was introduced to minimize the discrepancy of the model fitting. The iterative method produces local optimal estimate but this estimate depends on the tuning parameter which controls the relative importance of the two cost functions of the method. In numerical simulations, we demonstrated that a large value of the tuning parameter yields accurate estimated range of snaps which are further apart from the receiver. Since the parameter error in receiver orientation becomes less significant at smaller snap range, a smaller value for the tuning parameter is sufficient.

Finally, we solved the problem of estimating the location of snapping shrimp by relaxing the assumption of perfectly known associated direct arrival and surface-reflected snaps. We presented this problem as a joint association and estimation optimization problem. An algorithm was developed to alternatingly associate the arrivals with fixed parameters and estimate the parameters with fixed associated arrivals. Throughout the experiments in Singapore waters, we were able to reveal the forms of underwater structures of the long-term mooring buoys and the jetty in 3-dimensional space using solely noise generated by snapping shrimp inhabiting these structures. The success in detecting and localizing snapping shrimp noise potentially lays the foundation for a wide variety of underwater acoustic applications.

7.2 Future work

The use of underwater ambient sources to do passive sensing is an exciting field which still requires extensive work for improvement. While we have numerically shown that ideal detection performance is possible, and experimentally examined the detection performance using undersampled Fourier coefficients of sensor array recording, it is still unclear as to what the minimum number of Fourier coefficients should be. This is an interesting future research direction for building smaller aperture receivers with lower sampling rate, while preserving the DoA-ToA detection performance of impulsive signals. In fact, this is one of the examples in compressed sensing which is a signal processing approach to acquire the "compressed" signal [65].

In developing the parameter estimator, we proposed a rule of thumb in choosing the tuning parameter of the estimator instead of deriving a rigorous procedure to compute the value of the tuning parameter. In certain circumstances, the tuning parameter can be a predominant factor in determining the characteristic of the estimator, and therefore a more rigorous study on this issue is necessary. For snap localization, we noticed through the numerical and experimental datasets that the alternating association and estimation algorithm will converge after a number of iterations given the prior knowledge of the parameters. Further analysis such as the rate of convergence and the correctness of the algorithm is essential to examine this behaviour.

Our study produces reliable methods for underwater acoustic sensing with snapping shrimp noise. Equipped with these methods, we may further develop other underwater acoustic applications. For instance, the ability to localize snapping shrimp in 3-dimensional space using small aperture receiver facilitates coral reef monitoring. The idea of using snapping shrimp noise for coral reef monitoring using large aperture receiver or merely a one-sensor receiver to record snapping shrimp noise has been investigated [43], [66]. The former is capable of covering a large region of interest but is inefficient for long-term monitoring. The latter is easy to implement but is limited by the area of (monitoring) coverage. A large-area monitoring system using a small aperture sensor array would be a viable approach that fills the gap between the two approaches.

Bibliography

[1] J. L. Sutton, "Underwater acoustic imaging," *Proceedings of the IEEE*, vol. 67, no. 4, pp. 554–566, 1979.

[2] M. Doniec, C. Detweiler, I. Vasilescu, M. Chitre, M. Hoffmann-Kuhnt, and D. Rus, "Aquaoptical: A lightweight device for high-rate long-range underwater point-to-point communication," *Marine Technology Society Journal*, vol. 44, no. 4, pp. 55–65, 2010.

[3] M. Siderius, C. H. Harrison, and M. B. Porter, "A passive fathometer technique for imaging seabed layering using ambient noise," *The Journal of the Acoustical Society of America*, vol. 120, no. 3, pp. 1315–1323, 2006.

[4] M. Siderius, H. Song, P. Gerstoft, W. S. Hodgkiss, P. Hursky, and C. Harrison, "Adaptive passive fathometer processing," *The Journal of the Acoustical Society of America*, vol. 127, no. 4, pp. 2193–2200, 2010.

[5] P. L. Nielsen, M. Siderius, J. Miller, S. Crocker, and J. Giard, "Seabed characterization using ambient noise and compact arrays on an autonomous underwater vehicle." in *Proceedings of Meetings on Acoustics*, vol. 19, no. 1. Acoustical Society of America, 2013, p. 070030.

[6] C. Gervaise, B. G. Kinda, J. Bonnel, Y. Stéphan, and S. Vallez, "Passive geoacoustic inversion with a single hydrophone using broadband ship noise," *The Journal of the Acoustical Society of America*, vol. 131, no. 3, pp. 1999–2010, 2012.

[7] M. Chitre, M. Legg, and T.-B. Koay, "Snapping shrimp dominated natural soundscape in singapore waters," *Contrib Mar Sci*, vol. 2012, pp. 127–134, 2012.

[8] M. W. Legg, *Non-Gaussian and non-homogeneous Poisson models of snapping shrimp noise.* Citeseer, 2009.

[9] M. Chitre, S. Ong, and J. Potter, "Performance of coded ofdm in very shallow water channels and snapping shrimp noise," in *Proceedings of OCEANS 2005 MTS/IEEE.* IEEE, 2005, pp. 996–1001.

[10] A. Mahmood, M. Chitre, and M. A. Armand, "Improving psk performance in snapping shrimp noise with rotated constellations," in *Proceedings of the Seventh ACM International Conference on Underwater Networks and Systems.* ACM, 2012, p. 12.

[11] J. Butler, M. Butler, and H. Gaff, "Acoustic-based model estimation of snapping shrimp populations and the effects of a sponge die-off," *bioRxiv*, p. 056986, 2016.

[12] S. D. Simpson, M. Meekan, J. Montgomery, R. McCauley, and A. Jeffs, "Homeward sound," *Science*, vol. 308, no. 5719, pp. 221–221, 2005.

[13] C. Radford, J. Stanley, C. Tindle, J. Montgomery, and A. Jeffs, "Localised coastal habitats have distinct underwater sound signatures," *Marine Ecology Progress Series*, vol. 401, pp. 21–29, 2010.

[14] Ö. Yilmaz, *Seismic data analysis.* Society of exploration geophysicists Tulsa, 2001, vol. 1.

[15] G. Valenzise, L. Gerosa, M. Tagliasacchi, F. Antonacci, and A. Sarti, "Scream and gunshot detection and localization for audio-surveillance systems," in *Advanced Video and Signal Based Surveillance, 2007. AVSS 2007. IEEE Conference on.* IEEE, 2007, pp. 21–26.

[16] X. Lurton, *An introduction to underwater acoustics: principles and applications.* Springer Science & Business Media, 2002.

[17] D. Inman, "Scripps in the 1940s: the sverdrup era," *OCEANOGRAPHY-WASHINGTON DC-OCEANOGRAPHY SOCIETY-*, vol. 16, no. 3, pp. 20–28, 2003.

[18] S. Flatté and W. Munk, "Submarine detection: Acoustic contrast versus acoustic glow," *MITRE Corporation, McLean, Virginia, JASON JSR-85-108*, 1985.

[19] K. M. Stafford, C. G. Fox, and D. S. Clark, "Long-range acoustic detection and localization of blue whale calls in the northeast pacific ocean," *The Journal of the Acoustical Society of America*, vol. 104, no. 6, pp. 3616–3625, 1998.

[20] S. M. Van Parijs, M. Baumgartner, D. Cholewiak, G. Davis, J. Gedamke, D. Gerlach, S. Haver, J. Hatch, L. Hatch, C. Hotchkin *et al.*, "Nepan: A us northeast passive acoustic sensing network for monitoring, reducing threats and the conservation of marine animals," *Marine Technology Society Journal*, vol. 49, no. 2, pp. 70–86, 2015.

[21] K. F. Woolfe, S. Lani, K. G. Sabra, and W. Kuperman, "Monitoring deep-ocean temperatures using acoustic ambient noise," *Geophysical Research Letters*, vol. 42, no. 8, pp. 2878–2884, 2015.

[22] L. Fillingera, M. Chitreb, and V. Pallayilb, "Passive diver detection in warm waters," in *Proceedings of 1st International Conference on Underwater Acoustics (UAC), 23-28 June 2013, Corfu, Greece, 1459-1464*, 2013.

[23] V. N. Hari, M. Chitre, Y. M. Too, and V. Pallayil, "Robust passive diver detection in shallow ocean," in *OCEANS 2015-Genova.* IEEE, 2015, pp. 1–6.

[24] M. Chitre, K. T. Beng, and J. Potter, "Origins of directionality in snapping shrimp sounds and its potential applications," in *OCEANS 2003. Proceedings*, vol. 2. IEEE, 2003, pp. 889–896.

[25] K. T. Beng, T. E. Teck, M. Chitre, and J. R. Potter, "Estimating the spatial and temporal distribution of snapping shrimp using a portable, broadband 3-dimensional acoustic array," in *OCEANS 2003. Proceedings*, vol. 5. IEEE, 2003, pp. 2706–2713.

[26] M. W. Johnson, F. A. Everest, and R. W. Young, "The role of snapping shrimp (crangon and synalpheus) in the production of underwater noise in the sea," *Biological Bulletin*, pp. 122–138, 1947.

[27] D. H. Cato and M. J. Bell, "Ultrasonic ambient noise in australian shallow waters at frequencies up to 200 khz," DTIC Document, Tech. Rep., 1992.

[28] M. Versluis, B. Schmitz, A. von der Heydt, and D. Lohse, "How snapping shrimp snap: through cavitating bubbles," *Science*, vol. 289, no. 5487, pp. 2114–2117, 2000.

[29] M. W. Legg, A. J. Duncan, A. Zaknich, and M. V. Greening, "Analysis of impulsive biological noise due to snapping shrimp as a point process in time," in *OCEANS 2007-Europe.* IEEE, 2007, pp. 1–6.

[30] W. W. Au and K. Banks, "The acoustics of the snapping shrimp synalpheus parneomeris in kaneohe bay," *The Journal of the Acoustical Society of America*, vol. 103, no. 1, pp. 41–47, 1998.

[31] M. Legg, A. Duncan, A. Zaknich, and M. Greening, "An exploratory analysis of non-poisson temporal behaviour in snapping shrimp noise," in *Annual Conference of the Australian Acoustical Society: Acoustics in a Changing Environment, Acoustics 2005*, 2005. [Online]. Available: http://researchrepository.murdoch.edu.au/14403/

[32] M. Chitre, "Underwater acoustic communications in warm shallow water channels," *P. hD. Thesis, Singapore: National University of Singapore*, 2006.

[33] A. Mahmood and M. Chitre, "Modeling colored impulsive noise by markov chains and alpha-stable processes," in *OCEANS 2015-Genova*. IEEE, 2015, pp. 1–7.

[34] O. A. Godin, N. A. Zabotin, and V. V. Goncharov, "Ocean tomography with acoustic daylight," *Geophysical Research Letters*, vol. 37, no. 13, 2010.

[35] C. Epifanio, J. Potter, G. Deane, M. Readhead, and M. Buckingham, "Imaging in the ocean with ambient noise: the orb experiments," *The Journal of the Acoustical Society of America*, vol. 106, p. 3211, 1999.

[36] J. Potter and M. Chitre, "Ambient noise imaging in warm shallow seas; second-order moment and model-based imaging algorithms," *The Journal of the Acoustical Society of America*, vol. 106, p. 3201, 1999.

[37] S. Kuselan, M. Chitre, and V. Pallayil, "Ambient noise imaging through joint source localization," in *OCEANS 2011*. IEEE, 2011, pp. 1–5.

[38] M. Chitre, S. Kuselan, and V. Pallayil, "Ambient noise imaging in warm shallow waters; robust statistical algorithms and range estimation," *The Journal of the Acoustical Society of America*, vol. 132, no. 2, pp. 838–847, 2012.

[39] J. J. Piercy, E. A. Codling, A. J. Hill, D. J. Smith, and S. D. Simpson, "Habitat quality affects sound production and likely distance of detection on coral reefs," *Marine Ecology Progress Series*, vol. 516, pp. 35–47, 2014.

[40] B. G. Ferguson and J. L. Cleary, "In situ source level and source position estimates of biological transient signals produced by snapping shrimp in an underwater environment," *The Journal of the Acoustical Society of America*, vol. 109, p. 3031, 2001.

[41] M. J. Alam, E. H. Huntington, and M. R. Frater, "Passive auv tracking using sound produced by shrimps," in *2013 OCEANS-San Diego*. IEEE, 2013, pp. 1–5.

[42] J. C. Rosenberger, "Passive localization," in *Underwater Acoustic Data Processing*. Springer, 1989, pp. 511–524.

[43] S. E. Freeman, M. J. Buckingham, L. A. Freeman, M. O. Lammers, and L. Gerald, "Cross-correlation, triangulation, and curved-wavefront focusing of coral reef sound using a bi-linear hydrophone array," *The Journal of the Acoustical Society of America*, vol. 137, no. 1, pp. 30–41, 2015.

[44] R. Aubauer, M. O. Lammers, and W. W. Au, "One-hydrophone method of estimating distance and depth of phonating dolphins in shallow water," *The Journal of the Acoustical Society of America*, vol. 107, no. 5, pp. 2744–2749, 2000.

[45] A. Širović, J. A. Hildebrand, and S. M. Wiggins, "Blue and fin whale call source levels and propagation range in the southern ocean," *The Journal of the Acoustical Society of America*, vol. 122, no. 2, pp. 1208–1215, 2007.

[46] M. P. Olivieri, S. A. Glegg, and R. K. Coulson, "Measurements of snapping shrimp colonies using a wideband mobile passive sonar," *J. Acoust. Soc. Am*, vol. 103, no. 5 Pt 2, 1998.

[47] M. Buckingham, B. Berknout, and S. Glegg, "Imaging the ocean with ambient noise," *Nature*, vol. 356, no. 6367, pp. 327–329, 1992.

[48] K. T. BENG, "Development of a high frequency ambient noise data acquisition system," Ph.D. dissertation, 2004.

[49] P. Venugopalan, M. A. Chitre, E. T. Tan, J. Potter, K. T. Beng, S. B. Ruiz, and S. P. Tan, "Ambient noise imaging-first deployments of romanis and preliminary data analysis," in *OCEANS 2003. Proceedings*, vol. 2. IEEE, 2003, pp. 882–888.

[50] V. Pallayil, M. Chitre, S. Kuselan, A. Raichur, M. Ignatius, and J. R. Potter, "Development of a second-generation underwater acoustic ambient noise imaging camera," *IEEE Journal of Oceanic Engineering*, vol. 41, no. 1, pp. 175–189, 2016.

[51] M. A. Chitre and J. R. Potter, "Optimisation and beamforming of a two dimensional sparse array," in *High Performance Computing*, vol. 98. Citeseer, 1998.

[52] D. Malioutov, M. Çetin, and A. S. Willsky, "A sparse signal reconstruction perspective for source localization with sensor arrays," *Signal Processing, IEEE Transactions on*, vol. 53, no. 8, pp. 3010–3022, 2005.

[53] D. Johnson and D. Dudgeon, *Array signal processing: concepts and techniques.* Simon & Schuster, 1992.

[54] D. Malioutov *et al.*, "A sparse signal reconstruction perspective for source localization with sensor arrays," in *MS thesis, Mass. Inst. Technol*, 2003.

[55] A. Xenaki, P. Gerstoft, and K. Mosegaard, "Compressive beamforming," *The Journal of the Acoustical Society of America*, vol. 136, no. 1, pp. 260–271, 2014.

[56] M. Yuan and Y. Lin, "Model selection and estimation in regression with grouped variables," *Journal of the Royal Statistical Society: Series B (Statistical Methodology)*, vol. 68, no. 1, pp. 49–67, 2006.

[57] Y. C. Eldar, P. Kuppinger, and H. Bolcskei, "Block-sparse signals: Uncertainty relations and efficient recovery," *IEEE Transactions on Signal Processing*, vol. 58, no. 6, pp. 3042–3054, 2010.

[58] E. J. Candès, J. Romberg, and T. Tao, "Robust uncertainty principles: Exact signal reconstruction from highly incomplete frequency information," *Information Theory, IEEE Transactions on*, vol. 52, no. 2, pp. 489–509, 2006.

[59] E. J. Candes and T. Tao, "Near-optimal signal recovery from random projections: Universal encoding strategies?" *IEEE transactions on information theory*, vol. 52, no. 12, pp. 5406–5425, 2006.

[60] E. van den Berg and M. P. Friedlander, "Probing the pareto frontier for basis pursuit solutions," *SIAM Journal on Scientific Computing*, vol. 31, no. 2, pp. 890–912, 2008. [Online]. Available: http://link.aip.org/link/?SCE/31/890

[61] ——, "SPGL1: A solver for large-scale sparse reconstruction," June 2007, http://www.cs.ubc.ca/labs/scl/spgl1.

[62] L. M. Brekhovskikh and Y. Lysanov, *Fundamentals of ocean acoustics (3rd edition)*. Springer Verlag, 2003.

[63] J. M. Steele, *The Cauchy-Schwarz master class: an introduction to the art of mathematical inequalities*. Cambridge University Press, 2004.

[64] *Singapore Tide Table Year 2014*. Hydrographic Department, Maritime and Port Authority of Singapore, 2014.

[65] D. L. Donoho, "Compressed sensing," *IEEE Transactions on information theory*, vol. 52, no. 4, pp. 1289–1306, 2006.

[66] M. O. Lammers, R. E. Brainard, W. W. Au, T. A. Mooney, and K. B. Wong, "An ecological acoustic recorder (ear) for long-term monitoring of biological and anthropogenic sounds on coral reefs and other marine habitats," *The Journal of the Acoustical Society of America*, vol. 123, no. 3, pp. 1720–1728, 2008.

List of Publications

(C1) Y. M. Too and M. Chitre, "Localization of impulsive sources in the oceans using the method of images," in *MTS/IEEE Oceans-St. John's*, pp. 1-6, 2014.

(C2) Y. M. Too, M. Chitre and V. Pallayil, "Detecting the direction of arrival and time of arrival of impulsive transient signals," in *MTS/IEEE Oceans-Monterey's*, pp. 1-8, 2016.

(J1) Y. M. Too, M. Chitre, G. Barbastathis and V. Pallayil, "Localizing snapping shrimp noise using a small aperture array," in *IEEE Journal of Oceanic Engineering.* (submitted)

(P1) Y. M. Too, M. Chitre, V. Pallayil, Anshu and G. Barbastathis, "Coral reef monitoring using ambient noise," in *CENSAM 8th Annual Workshop*, 29 June 2015. (Poster Presentation)